

Estimation of Contact Forces in Reactor Internals using Neutron Noise Data:

A Comparison of Approaches

by

Nicholas Harn

Bachelor of Science in Mechanical Engineering, University of Pittsburgh, 2020

Submitted to the Graduate Faculty of

the Swanson School of Engineering in partial fulfillment

of the requirements for the degree of

Master of Science

University of Pittsburgh

2022

UNIVERSITY OF PITTSBURGH
SWANSON SCHOOL OF ENGINEERING

This thesis was presented

by

Nicholas Harn

It was defended on

July 20th, 2022

and approved by

Dr. William Clark, PhD, Professor, Department of Mechanical Engineering and Materials
Science

Dr. Joseph Yurko, PhD, Director of Undergraduate Data Science Education, School of
Computing and Information

Thesis Advisor: Dr. Daniel Cole, PhD, Associate Professor, Department of Mechanical
Engineering and Materials Science

Copyright © by Nicholas Harn
2022

Estimation of Contact Forces in Reactor Internals using Neutron Noise Data: A Comparison of Approaches

Nicholas Harn, M.S.

University of Pittsburgh, 2022

A pressurized water reactor’s radial keys prevent the reactor core from colliding with its housing. These supports gradually degrade at their points of contact, requiring regular inspections and preventative maintenance during reactor outages. Reactor outages are costly and time-consuming, yet they are necessary for continued safe operations. Outages could be expedited by monitoring the conditions of internal components during reactor operations. This is partially achieved by tracking the contact forces acting on the core barrel, which are altered by radial key degradation.

The contact force at each radial key is modeled as a hyperbolic tangent function of the core barrel’s velocity at the point of contact, capturing the contact force’s transition from viscous damping at low velocities to constant Coulomb friction at high velocities. Two condition-dependent parameters control the contact force model: the maximum contact force, α , and the inverse of the characteristic velocity at which the model transitions between behaviors, β . The contact force dampens the core barrel’s vibrations, which previous research has related to the neutron radiation measured outside the reactor core. The contact force is monitored using these ex-core neutron noise measurements.

This report compares two methods for approximating the contact force parameters. One method applies an unscented Kalman filter to the ex-core measurements. The other applies a grid search algorithm to several ensembles of core barrel simulations, each associated with a combinations of contact parameters. The grid search identifies the combination whose ensemble best approximates the ex-core measurements. These methods are applied to four synthetic datasets with known contact parameters to determine which approach, if any, produces more accurate parameter estimates.

The Kalman filter’s estimates are more accurate than the grid search’s approximations for Datasets 3 and 4. These datasets have α values of 490 N and 660 N, with β values of

70 s/m and 110 s/m respectively. The grid search method performs better than the Kalman filter for Dataset 1 where $\alpha = 100$ N and $\beta = 10$ s/m, while both methods are inaccurate for Dataset 2 where $\alpha = 31.6$ N and $\beta = 316$ s/m. Neither method accurately estimates the contact parameters for an arbitrary synthetic dataset.

Table of Contents

1.0	Introduction	1
1.1	Goals and Outcomes	1
1.2	State of the Art and Limits of Current Practice	1
1.3	Literature Review of Reactor Data	11
1.4	Research Approach	14
1.5	Research Impact	18
2.0	Models of the Core Barrel System	20
2.1	Neutron Noise Model	21
2.2	Vibrational Model	24
2.2.1	Core Barrel Dynamics	25
2.2.1.1	Lagrangian Approach	27
2.2.1.2	Newtonian Approach	32
2.2.1.3	Equations of Motion	34
2.2.2	Continuous-Time State Space Representation	34
2.2.3	Discrete-Time State Space Representation	37
2.3	Turbulence Model	40
2.4	Contact Model	40
2.4.1	Viscous Damping and Coulomb Friction Contact Models	41
2.4.2	Hyperbolic Tangent Contact Model	41
3.0	Synthetic Data Generation	43
3.1	Discrete-Time State Space	44
3.1.1	Structure	45
3.1.2	Reasons to Avoid Using Discrete State Space	46
3.2	Continuous-Time State Space	49
3.2.1	Limitations Regarding White Noise	52
3.2.2	Band-Limited White Noise	53

3.3	Values of Model Variables	54
3.3.1	Model Constants	54
3.3.2	Expected Measurement Noise	55
3.3.3	Contact Parameters	56
3.4	System Response	59
4.0	Machine Learning	64
4.1	Grid Search Method	64
4.2	Ensemble Average	65
4.3	Performance Metrics	67
4.3.1	Minimum Error	67
4.3.2	Maximum Likelihood	69
4.3.3	Maximum Cross-Correlation	70
5.0	Kalman Filter	72
5.1	Unscented Kalman Filters	75
5.2	Disturbed Parameter Estimation	78
5.3	Effects of Changing Model Parameters	80
5.3.1	Changing Initial Conditions	81
5.3.2	Changing True Parameters	82
5.4	State and Output Estimates	86
6.0	Results and Discussion	95
6.1	Overview of Methods	95
6.1.1	Overview of Grid Search	95
6.1.2	Overveiw of Kalman Filtering	97
6.2	Synthetic Dataset 1	98
6.2.1	Grid Search Results	98
6.2.2	Unscented Kalman Filtering Results	103
6.2.3	Comparison of Results	104
6.3	Synthetic Dataset 2	105
6.3.1	Grid Search Results	105
6.3.2	Unscented Kalman Filtering Results	105

6.3.3	Comparison of Results	110
6.4	Synthetic Dataset 3	111
6.4.1	Grid Search Results	111
6.4.2	Unscented Kalman Filtering Results	116
6.4.3	Comparison of Results	116
6.5	Synthetic Dataset 4	117
6.5.1	Grid Search Results	117
6.5.2	Unscented Kalman Filtering Results	117
6.5.3	Comparison of Results	121
6.6	Discussion and Comparison of Methods	122
6.6.1	Comparison of Method Performance	122
6.6.2	Discussion of Unexpected Phenomena	125
6.6.2.1	Deviation of Kalman Filtered Parameter Estimates	125
6.6.2.2	Identification of the Best-Performing Grid Element	128
7.0	Summary and Conclusions	129
7.1	Summary	129
7.2	Conclusions	130
7.3	Contributions	131
7.4	Future Work	133
Appendix A. Approximation of Damping Ratios		135
Appendix B. MATLAB Simulation Code		140
B.1	Synthetic Data Generation	140
B.1.1	Fourth-Order Runge-Kutta Method	149
B.1.2	Continuous-time Equations of Motion	149
B.1.3	Hyperbolic Tangent Contact Force Function	150
B.2	Grid Search Ensemble Generation	150
B.3	Unscented Kalman Filter Approximation	158
B.3.1	Unscented Transformation Function	165
B.3.2	Additional Computations for the Estimates	168
Bibliography		170

List of Tables

1	Table of reactors included in the literature review, as well as the years in which their frequency-domain information was extracted	11
2	Information regarding the vibration modes of a core barrel	12
3	Contact force parameters associated with each of the four synthetic datasets	60
4	Parameter estimates for various initial guesses α_0 and β_0 of the contact parameters. The unscented Kalman filter is applied to a synthetic dataset generated using $\alpha = 100$ N and $\beta = 10$ s/m.	81
5	Parameter estimates created by applying the unscented Kalman filter to various synthetic datasets These datasets are identified by their unique combinations of contact force parameters. The estimates all assume an initial parameter guess of $\alpha_0 = 0$ and $\beta_0 = 0$, with a disturbance of $\sigma_{\epsilon 1} = 10$ for α and $\sigma_{\epsilon 2} = 1$ for β . These simulations are all performed for a random number generation seed of 1, to ensure the variations between datasets are due to their contact parameters and not due to random chance.	85
6	Root-mean-squared error values for each output estimated by the unscented Kalman filter with respect to the training dataset's true outputs. The synthetic training dataset of this Kalman filter is generated using $\alpha = 100$ N and $\beta = 10.0$ s/m.	89
7	Root-mean-squared error of each state estimated by the unscented Kalman filter with respect to the training dataset's true states. This Kalman filter is trained on a synthetic dataset generated using $\alpha = 100$ N and $\beta = 10.0$ s/m.	92

8	($\alpha = 100, \beta = 10.0$) Grid search results for parameter combinations that perform optimally on various metrics with respect to synthetic dataset 1. These metrics seek to minimize the RMSE of the estimate with respect to the data, maximize the average log-likelihood that the synthetic data at a particular point in time came from the estimated ensemble, and maximize the time-averaged cross-correlation between the estimate and the ensemble.	102
9	($\alpha = 100, \beta = 10.0$) Grid search results for parameter combinations that perform above-average on all tested performance metrics for synthetic dataset 1. The geometric mean values of the contact parameters in this dataset are $\alpha \approx 268$ N and $\beta \approx 5.18$ s/m.	102
10	($\alpha = 100, \beta = 10.0$) Grid search method's contact parameter estimates for synthetic dataset 1	103
11	($\alpha = 100, \beta = 10.0$) Unscented Kalman filter's contact parameter estimates for synthetic dataset 1	103
12	($\alpha = 100, \beta = 10.0$) Comparison of contact parameters estimated for synthetic dataset 1, and the ratio of each estimate to its true value . . .	105
13	($\alpha = 31.6, \beta = 316$) Grid search results for parameter combinations that perform optimally on various performance metrics for synthetic dataset 2	108
14	($\alpha = 31.6, \beta = 316$) Grid search results for parameter combinations that perform above-average on all performance metrics of interest, with respect to synthetic dataset 2. These parameters have geometric average values of $\alpha \approx 164$ N and $\beta \approx 10.0$ s/m.	109
15	($\alpha = 31.6, \beta = 316$) Grid search method's contact parameter estimates for synthetic dataset 2	109
16	($\alpha = 31.6, \beta = 316$) Unscented Kalman filter's contact parameter estimates for synthetic dataset 2	110
17	($\alpha = 31.6, \beta = 316$) Comparison of contact parameter estimates for synthetic dataset 2, and the ratio of each estimate to its true value . . .	110

18	$(\alpha = 490, \beta = 70.0)$ Parameter combinations that perform optimally for synthetic dataset 3 according to each performance metric. This grid does not contain the true contact parameter combination, so the true combination's performance on the various metrics cannot be evaluated.	114
19	$(\alpha = 490, \beta = 70.0)$ Contact parameter combinations that performed better than average on all metrics across the grid for synthetic dataset 3. The geometric average parameter values for this subset are $\alpha \approx 100$ N and $\beta \approx 3.83$ s/m.	115
20	$(\alpha = 490, \beta = 70.0)$ Unscented Kalman filter's contact parameter estimates for synthetic dataset 3	116
21	$(\alpha = 490, \beta = 70)$ Comparison of contact parameters estimated for synthetic dataset 3, and the ratio of each estimate to its true value	116
22	$(\alpha = 660, \beta = 110)$ Grid search results for synthetic dataset 4. This parameter combination does not fall on the grid, so the performance metrics associated with the true parameters cannot be computed.	120
23	$(\alpha = 660, \beta = 110)$ Parameter combinations that perform above-average on all performance metrics for synthetic dataset 4. This dataset's geometric average parameters are $\alpha \approx 178$ N and $\beta \approx 3.83$ s/m.	121
24	$(\alpha = 660, \beta = 110)$ Unscented Kalman filter's contact parameter estimates for synthetic dataset 4	121
25	$(\alpha = 660, \beta = 110)$ Comparison of contact parameters estimated for synthetic dataset 4, and the ratio of each estimate to its true value	122
26	Comparison of contact parameters estimated for 4 separate synthetic datasets through the grid search (GS) and Kalman filter (KF) methods. The ratio between each estimate and its associated true value is also computed.	124
27	Resonance peaks and damping ratios for Output 1 of the core barrel system	138
28	Resonance peaks and damping ratios for Output 2 of the core barrel system	138
29	Resonance peaks and damping ratios for Output 3 of the core barrel system	139
30	Resonance peaks and damping ratios for Output 4 of the core barrel system	139

List of Figures

Figure 1: A 3D representation of the core barrel. It is assumed to be a rigid cylindrical body mounted inside of a reactor vessel.	3
Figure 2: 3-D layout of the reactor's eight ex-core neutron flux sensors	4
Figure 3: Layout of the reactor's ex-core neutron flux sensors in the yz plane . . .	5
Figure 4: A comparison of the core barrel's modes of vibration. Top left: Stationary core barrel. Top right: Shell mode. Bottom left: Beam mode. Bottom right: Tilting mode.	8
Figure 5: Model of the contact force acting upon a core barrel as a function of the point-of-contact's velocity. For this simulation, the contact force transitions from a linear function of velocity to a constant force of $\alpha = 100$ N near a velocity of $\frac{1}{\beta} = 0.1$ m/s.	16
Figure 6: Block diagram of the core barrel's vibration model, using state-space notation	21
Figure 7: The free-body diagram of the core barrel, assuming all forces and motions are constrained to the yz plane. The body has a center of mass G, and its supports are attached at points A, B, C, and D.	26
Figure 8: Relationship between the contact force and the velocity at the point of contact for $\alpha = 100$ N and $\beta = 10.0$ s/m. The characteristic velocity $v_c = 0.100$ m/s represents the contact force's transition from a nearly linear relationship to a constant value.	58
Figure 9: Grid of parameter combinations for consideration	60
Figure 10: Response of the ex-core neutron noise sensors to the core barrel's vibrations	63
Figure 11: Contact parameter estimates for $\alpha = 100$ and $\beta = 10$, where the initial conditions for the parameters are a factor of 10 above their true values .	83
Figure 12: Contact parameter estimates for $\alpha = 100$ and $\beta = 10$, where the initial conditions for the parameters are a factor of 10 below their true values .	84

Figure 13: The unscented Kalman filter's estimates for the core barrel system's ex-core neutron noise outputs. The Kalman filter is trained on a synthetic dataset generated using $\alpha = 100$ N and $\beta = 10.0$ s/m.	87
Figure 14: Error of the unscented Kalman filter's output estimates for a synthetic dataset with $\alpha = 100$ N and $\beta = 10.0$ s/m	88
Figure 15: The unscented Kalman filter's estimates for the core barrel system's position states. The Kalman filter is trained on a synthetic dataset generated using $\alpha = 100$ N and $\beta = 10.0$ s/m.	90
Figure 16: Errors in the unscented Kalman filter's estimates for the core barrel system's position states. The Kalman filter is trained on a synthetic dataset generated using $\alpha = 100$ N and $\beta = 10.0$ s/m.	91
Figure 17: The unscented Kalman filter's estimates for the core barrel system's velocity states. This Kalman filter's training dataset uses a contact parameter combination of $\alpha = 100$ N and $\beta = 10.0$ s/m.	93
Figure 18: Errors in the unscented Kalman filter's estimates for the core barrel system's velocity states. This Kalman filter's training dataset uses a contact parameter combination of $\alpha = 100$ N and $\beta = 10.0$ s/m.	94
Figure 19: Root mean squared error of each parameter combination's estimate with respect to synthetic dataset 1. The star represents the dataset's true parameter combination.	99
Figure 20: Time-averaged log-likelihood that synthetic dataset 1 originates from each parameter combination's ensemble of simulations. The star represents the dataset's true parameter combination.	100
Figure 21: Time-averaged cross-correlation between synthetic dataset 1 and the ensemble average of a parameter combination's simulations, evaluated for each parameter combination on the grid. The star represents the dataset's true parameter combination.	101
Figure 22: Root mean squared error of each parameter combination's estimate with respect to synthetic dataset 2. The star represents the dataset's true parameter combination.	106

Figure 23: Time-averaged log-likelihood that synthetic dataset 2 originates from each parameter combination's ensemble of simulations. The star represents the dataset's true parameter combination.	107
Figure 24: Time-averaged cross-correlation between synthetic dataset 2 and the ensemble average of a parameter combination's simulations, evaluated for each parameter combination on the grid. The star represents the dataset's true parameter combination.	108
Figure 25: Root mean squared error of each parameter combination on the grid with respect to synthetic dataset 3. The star indicates the dataset's true contact parameters.	112
Figure 26: Time-averaged log-likelihood that synthetic dataset 3 originates from a parameter combination's ensemble of simulations, evaluated at every parameter combination on the grid. The star indicates the dataset's true contact parameters.	113
Figure 27: Time-averaged cross-correlation between synthetic dataset 3 and the ensemble average of a parameter combination's simulations, evaluated at every parameter combination on the grid. The star indicates the dataset's true contact parameters.	114
Figure 28: Root mean squared error of each parameter combination on the grid with respect to synthetic dataset 4. The star indicates the dataset's true contact parameters.	118
Figure 29: Time-averaged log-likelihood that synthetic dataset 4 originates from a parameter combination's ensemble of simulations, evaluated at every parameter combination on the grid. The star indicates the dataset's true contact parameters.	119
Figure 30: Time-averaged cross-correlation between synthetic dataset 4 and the ensemble average of a parameter combination's simulations, evaluated at every parameter combination on the grid. The star indicates the dataset's true contact parameters.	120

Figure 31: Plot of the contact parameter estimates across all datasets and estimation methods. The shapes of the markers indicate whether a parameter combination is a synthetic dataset's true parameters, a Kalman filter estimate, or a grid search estimate. The markers for the grid search and Kalman filter estimates are color-coded to match their respective synthetic datasets. 123

Figure 32: Power Spectral Density plots of the core barrel system's outputs for simulations with and without the contact force. The simulation that accounts for the contact force has contact parameter values of $\alpha = 100$ N and $\beta = 10$ s/m. Resonance peaks are identified using a minimum prominence threshold of 15 dB, minimum peak width of about 1.5 Hz, and a minimum peak height of -50 dB to exclude the output's noise floor. 136

1.0 Introduction

1.1 Goals and Outcomes

The goal of this project is to develop a technique that approximates the condition of the reactor vessel supporting structures based on the ex-core neutron radiation measurements. A nuclear reactor core's supporting structures prevent the core from colliding with the housing. These structures can gradually degrade, requiring regular inspections and preventative maintenance. The reactor must be shut down to perform an inspection, resulting in lost energy production. If inspections are performed too often, the plant will experience a severe loss of profits due to these outages. However, the core's supports will degrade undetected if inspections aren't performed often enough, causing significant damage to the reactor's internal components. Therefore, there is a critical need to optimize maintenance and inspections for safety and profits. The inspection process could be more efficient if we had methods to monitor the condition of the reactor vessel during operation. At the conclusion of this research, we should be able to do the following:

1. Detect changes in the condition of the reactor vessel internals over long time periods
2. Model the response of the core barrel to an input force applied by the turbulent coolant flow
3. Relate the condition of the reactor internals to the contact force acting on the core barrel
4. Extract the contact force model's parameters from the ex-core radiation measurements
5. Compare the performances of different methods for locating the contact force parameters

1.2 State of the Art and Limits of Current Practice

The reactor core of a pressurized water reactor (PWR) is housed in a core barrel suspended within a pressure vessel filled with water. The water acts as a coolant for the reactor core, and it is pumped at such a high flowrate that the turbulence excites movement in the

core barrel. The core barrel is supported by two hold-down springs and two radial keys. The springs support the majority of the core barrel’s weight within the vessel, while the radial keys bear the rest of the load and prevent the structure from rotating about the vertical axis. Additionally, two sets of horizontal springs and viscous dampers act on the core barrel’s upper edges at the same locations as the hold-down springs. A diagram of the core barrel system’s model is shown in Figure 1.

A typical PWR has eight ex-core neutron noise sensors mounted in the configuration shown in Figure 2. Four sensors lie within the xz plane, while four are found in the yz plane. Assuming the core barrel’s motion is restricted to the yz plane, the positions of the four relevant ex-core sensors are configured as follows:

- Sensor 1: Positive y , positive z
- Sensor 2: Positive y , negative z
- Sensor 3: Negative y , positive z
- Sensor 4: Negative y , negative z

This 2-D configuration is displayed in Figure 3, and it allows the core barrel’s motion to be fully described using an ex-core neutron noise method.

Current operations and maintenance (O&M) practices for a PWR consist of periodic inspections of the reactor internals, including the core barrel’s structural supports. The reactor must be completely shut down for each inspection, leading to downtime for the nuclear plant. If inspections are performed more often than necessary, the required downtime would significantly restrict the plant’s power production capabilities and reduce its profits. However, if the reactor is not inspected often enough, the degradation of its components could lead to a failure, damaging the reactor and potentially endangering nearby personnel. Therefore, a nuclear power plant must optimize inspections to minimize losses while maintaining safe operating conditions.

The reactor’s radial keys are of particular interest to O&M personnel because they constrain the rotation of the reactor core barrel about the vertical axis and aid in damping the rest of the barrel’s motion. The radial keys undergo a nonlinear contact force, and the contact mechanism changes as the contact surfaces of the keys are “hammered-in” by

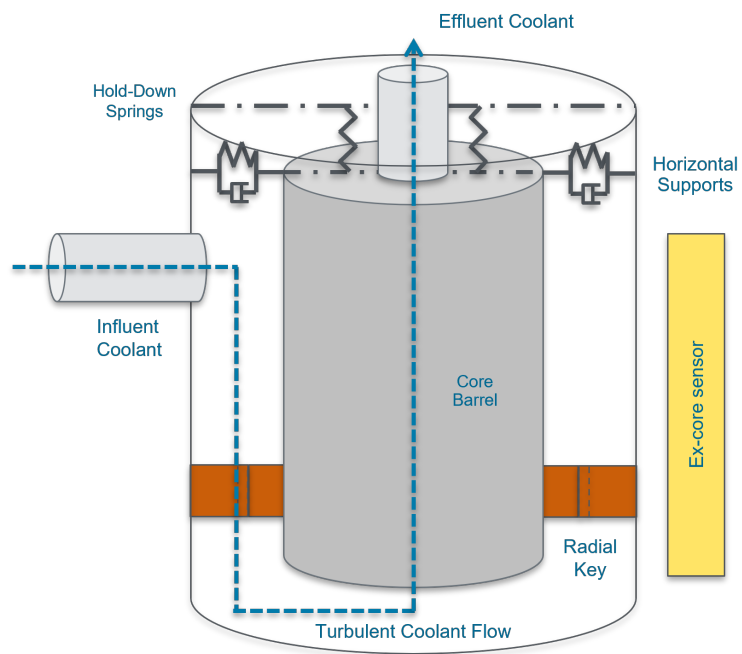


Figure 1: A 3D representation of the core barrel. It is assumed to be a rigid cylindrical body mounted inside of a reactor vessel.

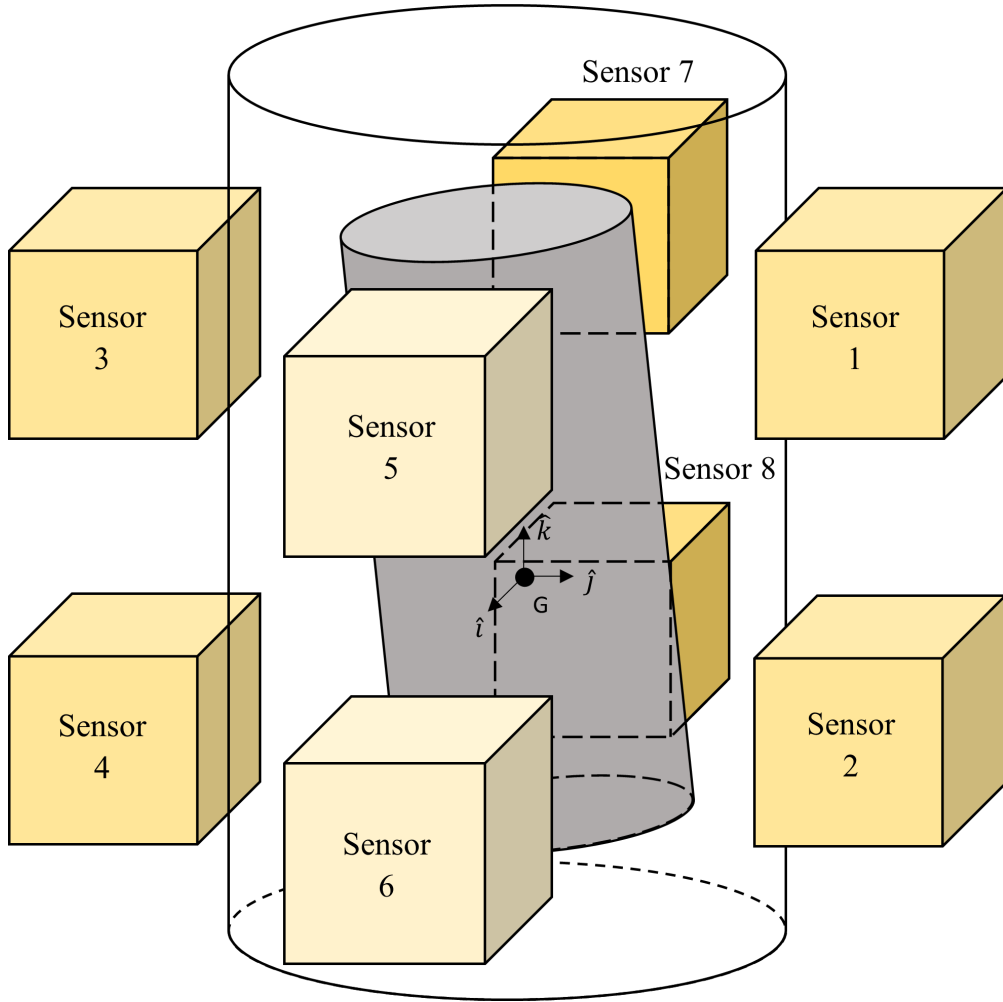


Figure 2: 3-D layout of the reactor's eight ex-core neutron flux sensors

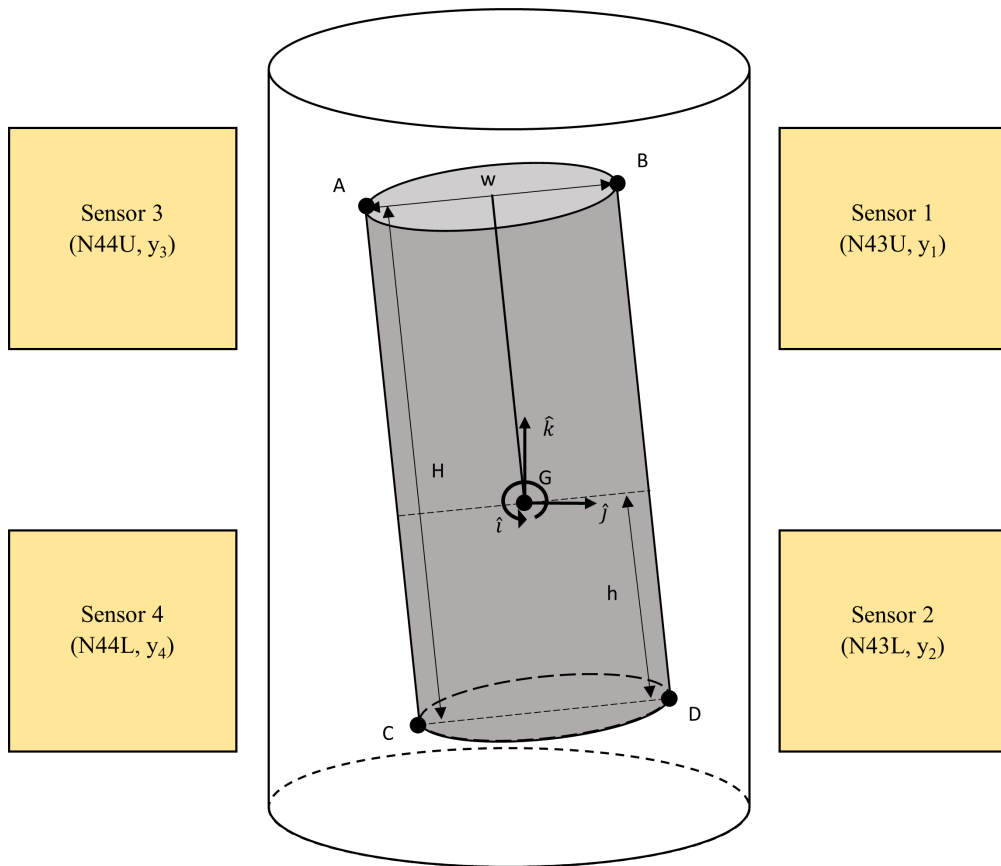


Figure 3: Layout of the reactor's ex-core neutron flux sensors in the yz plane

the excited core barrel. This degradation gradually increases the spacing between the keys and their mounts on the reactor vessel, decreasing the contact frequency and changing the vibration spectra of the core barrel [9].

Although there are no vibration sensors within the core barrel, the structure's vibrations can be approximated from the measurements of the ex-core radiation sensors [8]. The relationship between the radiation measurements and the vibrations of the core barrel follows a simple attenuation mechanism: As the core barrel moves towards a sensor, the effective distance between the radiation source and the sensor decreases, and so the measured neutron radiation will increase. Similarly, the radiation measurement will decrease as the radiation source moves away from the sensor due to an increase in the effective attenuation distance [7].

Certain research has attempted to directly relate the changes in the ex-core neutron radiation measurements to the condition of the reactor supports [9]. These approaches begin by defining the contact force at the radial key as a function of degradation. The contact surface between the radial key and its mount is gradually worn away during operations, decreasing the contact force applied to the core barrel through friction. The contact force is included in the core barrel's equations of motion, which are then substituted into the documented relationship between vibrations and ex-core measurements. The result is an equation relating the degradation of the radial key to the ex-core neutron noise measurements.

The vibrations of the core barrel are but one of many components comprising the ex-core sensor readings of an actual PWR system. Other factors must be taken into account, such as the reactivity of the reactor's fuel, the spectra of the turbulent flow driving the core barrel's motion, and the random uncorrelated measurement noise in the outputs [2]. The approach outlined in previous research assumes that the fluctuations in the ex-core measurements are solely caused by the degradation of the radial key. This neglects fluctuations in the other components of the ex-core sensor readings, potentially misidentifying those sources of neutron noise as changes in the core barrel's vibration profile.

The vibration profile could also be altered by the degradation of components other than the radial keys, such as a decrease in the stiffness of the hold-down springs, or relaxation of the supporting clamps that secure the core barrel [10]. Simply assuming that the change in

the profile is due to wear at the radial keys would lead to confusion between the degradation of the keys and any other changes within the vibration model. However, such issues are beyond the scope of this project. This report focuses on methods for estimating contact forces from ex-core neutron noise data for the purposes of condition monitoring. It assumes that the changes in the core barrel vibrations are mostly caused by the changing behavior of the contact forces due to degradation at the radial keys. Future research seeking to more accurately represent the relationship between measured neutron noise, core barrel vibrations, and radial key condition should account for the degradation of other reactor structures and include other sources of neutron noise .

The core barrel’s vibrations include several modes, each of which describes a characteristic behavior in the structure’s motion. For instance, shell mode vibrations account for changes in the circumference and axial cross-section of the core barrel [8]. These changes include distortion of the core barrel’s cross section from a circle to an ellipse, uniform expansion or contraction of the cylinder’s circumference, and fluctuations in the circumference along the barrel’s axis. Beam mode vibrations isolate the pendulum-like swaying motion of the core barrel’s free end about a fixed axis [5]. These are similar to the tilting mode vibrations, which describe the rotation of the core barrel about an axis intersecting its center of mass [2]. The three modes of vibration are visually compared in Figure 4. The general vibrations of the core barrel are described by some combination of these three modes.

Early condition monitoring efforts for reactor internals relied on mechanical measurements from pressure sensors and accelerometers to extract the eigenfrequencies of the core’s vibrations, which decrease during degradation [5]. Later methods used neutron noise analysis via ex-core ion chambers to extract additional information, such as the direction and amplitude of the vibrations.

The neutron noise method requires taking the auto-power-spectral densities (APSDs) of the ex-core sensor readings and relating the peaks in the spectra to the vibrations at the system’s eigenfrequencies, or relating the peaks to the resonances of the pressure fluctuations that drive the vibrations [5]. Model-based analysis, independent pressure and displacement measurements, and structural mechanics calculations are leveraged to determine the origins of all peaks within the spectra.

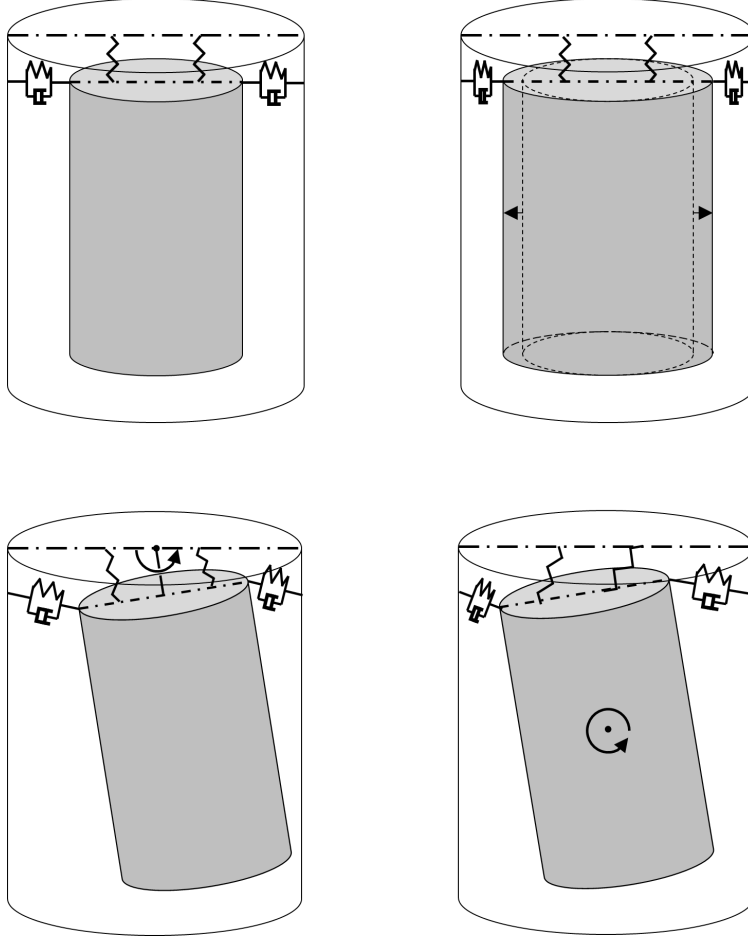


Figure 4: A comparison of the core barrel's modes of vibration. Top left: Stationary core barrel. Top right: Shell mode. Bottom left: Beam mode. Bottom right: Tilting mode.

There are two main approaches for diagnosing the spatial distribution of the vibrations. The first approach is to use a qualitative time-domain method, which assumes random 2-D vibrations that may or may not include some anisotropy and preferred direction. Time-domain methods include visualizing the motion through 2-D amplitude probability distributions, 2-D motion trajectories, and/or equi-probability lines [5]. The visualizations are useful for detecting sudden changes in the ex-core outputs, and for monitoring the reactor in real-time from the control room. However, identifying changes in the patterns of the visualizations is a subjective process, unfit for quantitative analysis of the noise or analyzing its trend over time [5].

The second approach for diagnosing the spatial distribution of the beam mode vibrations is to apply a quantitative frequency-domain method. This assumes various vibration modes and other noise components, such as reactivity and background noise, are present in the ex-core signals. Frequency analysis methods separate these components, after which the spatial properties of the beam mode vibrations are described by determining the weights of the components. The spectral decomposition algorithm is an example of a frequency-domain method for extracting the spatial properties of beam mode vibrations [5]. Spectral decomposition estimates the direction and amplitude of vibrational motion over a range of frequencies. The amplitude of the signal indicates how far the core barrel swings in its pendulum mode, while the direction of the motion indicates the source of unbalance in the reactor. This method separates the vibration modes by assuming the cross-spectra between them are zero [4]. Spectral decomposition has been implemented for analyzing the motions of multiple WWER-type reactors, such as Reactor Unit 2 at the Paks Nuclear Power Plant in Hungary. The method is compatible with other reactor designs as well, making it a versatile tool for frequency-domain analysis [4].

One major drawback of frequency domain methods is that the analysis assumes all modes are equally likely to correspond to a given peak, due to a lack of assumptions on prior information [5]. The spectral decomposition algorithm is expected to select the modes corresponding to each peak, which is inefficient when prior testing has already revealed this information. Also, some vibrational modes cannot be identified from the autospectral densities of the ex-core signals. In 2016, degradation was observed in the reactor alignment pins and lower

radial key of Reactor Unit 4 at the Ringhals Nuclear Power Plant in Sweden. Such wear is inconsistent with the beam mode and shell mode motions of the reactor core barrel, suggesting the presence of other vibration modes in the system [2]. The presence of a “tilting” vibration mode was proposed in response to this observation. This new mode describes a slight tilting motion of the reactor core barrel about a pivot in the xy plane running through the structure’s center of mass [2].

The pendulum-like motion associated with the beam mode and the slight rotational motion of the tilting mode are similar, causing confusion when analyzing them in the autospectral density functions. The main differences between these two modes are instead found in the phase and coherence relationships between ex-core signals, which are extracted from the cross-spectra between the signals. When examining detectors on opposite sides of the core barrel and on different axial levels, such as Sensors 1 and 4 in Figure 3, the tilting mode components are in-phase with the measured signal and the beam mode components are out-of-phase [2]. If the detectors on the same axial level are examined instead, then the tilting mode components are out-of-phase.

The tilting mode cannot be easily identified from these pair-wise coherences and phases. This is because the tilting motion is so slight that the change in the ex-core signals from tilting is almost negligible. The tilting mode must be extracted from the signals and enhanced by considering the symmetries between all eight ex-core detectors. Time-domain methods identify the tilting mode by comparing the detector signals at each instant in time. Frequency-domain methods use cross-spectral-density functions and coherence functions between the output signals to separate their in-phase and out-of-phase components, thereby isolating the tilting mode from the beam mode.

In summary, current reactor models require accounting for the beam mode, shell mode, and tilting mode vibrations of the core barrel. Frequency-domain methods identify these modes using patterns in the APSDs and CPSDs of the neutron radiation measurements at the ex-core sensors. Peaks in the APSDs indicate vibration modes and resonances from the system’s driving force. Most vibration modes are separated in the frequency domain by applying spectral decomposition algorithms such as SPEC-DEC to the APSDs. Certain vibration modes only appear when comparing the phase and coherence of output signals

Table 1: Table of reactors included in the literature review, as well as the years in which their frequency-domain information was extracted

Reactor	Design	Power (MWe)	Year of Measurement
Paks-2	WWER	440	1992
Kalinin-1	WWER	1000	1992
Ringhals-3	Westinghouse	950	2013
Ringhals-4	Westinghouse	950	2015
ORNL	Westinghouse	1148	1981

from different sensors. This is achieved using the CPSDs and coherence functions between the ex-core sensor outputs.

1.3 Literature Review of Reactor Data

The outputs of the core barrel models should reflect the core barrel behavior documented in other resources on this topic. A literature review was conducted to identify general trends in the ex-core measurements and vibration spectra of PWR core barrels. This information will aid in the development of a model that accurately represents the measured response of a core barrel to its operating conditions. The five pressurized water reactors (PWRs) listed in Table 1 are discussed in this literature review. The Paks-2 WWER-440 PWR is a 440 MWe water-water energetic reactor (WWER, or VVER) located at the Paks Nuclear Power Plant in Paks, Hungary. This type of reactor is a predecessor of the WWER-1000, which produces 1000 MWe of electrical energy. The Kalinin-1 PWR of the Kalinin Nuclear Power Station in Kalinin, Russia is an example of a WWER-1000 reactor. Reactor units 3 and 4 at the Ringhals Nuclear Power Plant in Sweden are both 950 MWe Westinghouse PWRs. Another Westinghouse PWR from Oak Ridge National Lab (ORNL) is analyzed as well. This reactor generates 1148 MWe of electrical energy.

Table 2: Information regarding the vibration modes of a core barrel

Reactor	Beam mode	Tilting mode	Pendulum mode	Shell mode
Paks-2	1.27 Hz	N/a	1.1 Hz	N/a
Kalinin-1	2 Hz to 6 Hz	N/a	1.3 Hz to 4.7 Hz	N/a
Ringhals-3	7 Hz to 8 Hz	N/a	N/a	20 Hz
Ringhals-4	7 Hz to 8 Hz	6 Hz	N/a	20 Hz
ORNL	6 Hz to 7 Hz	N/a	N/a	11.5 Hz to 12 Hz

The ex-core measurement spectra contain several resonant frequencies, each associated with a separate mechanism in the reactor. The resonance peaks below 1 Hz are associated with the thermal-fluid feedback effects of the system [10]. Peaks between 1 Hz and 10 Hz generally come from the vibrations of the core barrel structure [10]. These include the beam-mode vibrations of the core barrel as it swings in a pendular motion, the vibrations of the fuel assembly, and the tilting mode of the core barrel [2]. For frequencies between 10 Hz and 20 Hz, the resonant peaks originate from the shell-mode vibrations of the core barrel's rigid body [10]. Frequencies above 20 Hz come from the coolant pumps, which provide the turbulent flow that excites the system [4]. The exact locations of the resonant peaks within these frequency ranges depends on the construction of the reactor. The resonance frequencies of the reactors from the literature review are listed in Table 2.

In an analysis of the Paks-2 reactor in 1998, the ex-core measurements were processed through a low-pass filter with a cutoff frequency in the 4 to 6 Hz range [4]. As a result, vibrations at frequencies above 6 to 9 Hz could only be detected from other sensors, such as the in-core detectors. The ex-core measurements of the Ringhals-3 PWR were recorded every 50 days over a 100 day period in 2013 as part of a research study [3]. These measurements had a sampling frequency of 62.5 Hz, allowing for the analysis of dynamics below 31.25 Hz without introducing aliasing effects.

The beam modes of WWER-type reactors had resonant frequencies ranging from 2 to 6 Hz. These peaks separated over the course of a fuel cycle [4]. The Ringhals reactors had beam-mode peaks in the range of 7 to 8 Hz, while Westinghouse's four-loop reactor had a

beam mode frequency near 6 to 7 Hz [5] [10]. The Ringhals and Westinghouse reactors had multiple fuel assembly vibration modes, also known as reactivity modes. The first reactivity mode for the Westinghouse reactor occurred near 3 to 3.5 Hz, while the second reactivity mode was near 7 to 8 Hz [10]. Over the course of a fuel cycle, the second reactivity mode and the beam mode for the Westinghouse reactor experienced shifts in frequencies, causing the peaks to eventually overlap near 8 Hz. The Ringhals reactors had reactivity modes near 8 Hz as well [5].

The first-order shell modes for the Ringhals reactors were near 20 Hz, and the shell mode for the Westinghouse reactor was in the range of 11.5 to 12 Hz [10]. These peaks remained relatively constant over the fuel cycles of their reactors [3]. The tilting mode of the Ringhals reactor occurred at 6 Hz [2]. This mode appeared as a change in phase and coherence, rather than as a peak in the spectra.

Sometimes, the dynamics of the coolant pumps become part of the ex-core spectra. For the WWER reactors, the feedwater pump had an associated frequency of 25 Hz, which was extracted from an accelerometer mounted to the pump's housing [4]. This matches the needle-peak frequency in the ex-core spectra of the Ringhals reactors, which is also hypothesized to have originated from the pump [3]. However, the WWER reactors had additional dynamics associated with their coolant pumps. The first-order harmonics of the main coolant pumps for those reactors occurred at 33.3 Hz, and the pumps also experienced a rotational frequency of 16.6 Hz [4]. Standing pressure waves formed in the coolant flows of those reactors at 8.6 Hz, and the flow experienced a pressure oscillation of around 9 Hz.

As previously mentioned, the ex-core measurement spectra of the reactors were dominated by thermal-hydraulic feedback effects for frequencies below 1 Hz [4]. Specifically, thermal-hydraulic effects occurred in the WWER reactors in the region of 0.18 to 0.60 Hz, and in the Westinghouse reactor in the 0.001 to 1 Hz region [10]. One of the seven control rods within the Paks-2 WWER-440 reactor oscillated in a pendulum-like motion, creating a peak in the measured spectra near 1.1 Hz [4]. The Ringhals-3 PWR also experienced a peak at 1 Hz, although the source of this peak is unknown [5].

Minor peaks formed in the Westinghouse reactor from unknown causes. These peaks occurred at frequencies of 2 Hz, 4 Hz, and 9 Hz. The 4 Hz peak is potentially believed to be

connected to the vibrations of the fuel assembly, but research into the causes of the other peaks is still ongoing [10]. These peaks were far less distinct than the other resonance peaks in the reactor, and so they are usually ignored during analysis.

The Paks-2 WWER-440 reactor experienced a peak in its ex-core APSD at a frequency of 1.27 Hz [4]. At this peak, the maximum phase between horizontally-placed in-core detectors reached 82 deg. In the Kalinin WWER-1000 reactor, a second resonance peak formed in the 1.3 Hz to 4.7 Hz region [4]. This peak is assumed to originate from the beam-mode vibrations of the core barrel, and it gradually separated into two peaks over the reactor's 90-day installation period.

The literature review's compiled information indicates that the core barrel's vibration estimates from the ex-core sensor readings should have a resonance peak in the range from 1 Hz to 10 Hz. This peak is associated with both the beam mode and the tilting mode of the vibrations. The shell mode does not appear for this simulation because shell mode vibrations require radial deformation of the core barrel. This core barrel simulation assumes the structure is rigid, so deformation effects are ignored. No standing pressure waves, pump rotation frequencies, thermal-hydraulic feedback effects, or fuel reactivity modes are considered within the simulation either. The core barrel simulation assumes the ex-core neutron noise readings are independent of these effects, and that the ex-core measurements only depend upon the vibrations of a rigid core barrel.

1.4 Research Approach

The core barrel is modeled as a spring-mass-damper system undergoing turbulent and contact excitation forces. The contact force, turbulent force, and vibrational behavior of the core barrel are separated into three different models. This allows for the analysis of each model's mechanics and dynamics independent of the others.

Separating the contact model from the vibrations and turbulence models isolates the degradation of the radial keys from all other changes in the overall system over time. Changes in the relationship between the contact point velocities and the contact forces can then be

analyzed without needing to consider the influence of the vibrational structure and the turbulent input on the contact point velocities. If the contact, turbulence, and vibrations models were not separated, any changes in one model could be confused for changes in another. This would complicate the analysis of how any one model evolves over time as the radial keys degrade. Therefore, separating the contact model from the vibrations and turbulence models provides a better measure of the radial key's condition over time.

The turbulent forces acting on the core barrel are assumed to be a scaling of Gaussian white noise with an average value of 0. These forces drive the core barrel's vibrations by randomly exciting the structure. The scaling term applied to the white noise defines the standard deviation of the Gaussian distribution. This term is selected such that the motion of the excited core barrel system is significant enough to cause detectable deviations in the ex-core neutron measurements.

The contact force at each radial key is modeled as a nonlinear function of the core barrel's velocity at the point of contact. At low velocities, the contact force acting on a radial key is linearly proportional to the key's velocity, much like a linearly-viscous friction force. However, the contact force transitions to a near-constant value at higher velocities. An accurate model for the contact forces must account for these nonlinear mechanics while also taking into account the changes in contact due to degradation. This is achieved by introducing two scaling parameters for controlling the contact force model. The first parameter α controls the magnitude of the contact force, and the second parameter β controls the velocity at which the contact mechanics transition from a linearly-viscous force to a constant friction force. The contact forces are approximated using a hyperbolic tangent function of velocity, which transitions from a linearly-viscous force at low velocities to a constant friction force at high velocities. An example of this model is shown in Figure 5 for parameter values of $\alpha = 100$ N and $\beta = 10$ s/m. The β parameter scales terms within the function, while α scales the entire function. One of the main goals of this report is to compare two methods for estimating these contact parameters from the ex-core neutron noise measurements.

As the radial keys degrade over time, the contact spacing increases and the contact frequency decreases, changing the values of the contact model's two unknown parameters. Assuming that the ex-core measurements are taken for a few hours each month, the contact

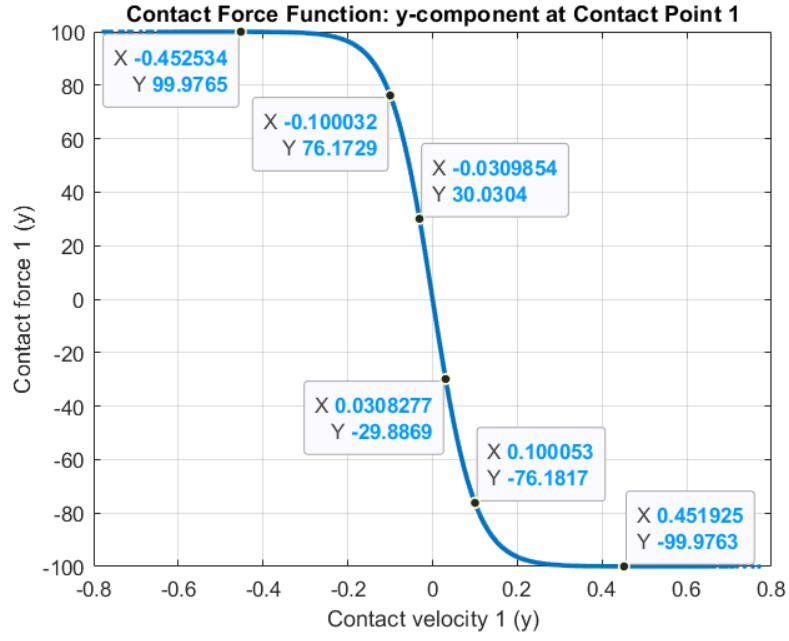


Figure 5: Model of the contact force acting upon a core barrel as a function of the point-of-contact's velocity. For this simulation, the contact force transitions from a linear function of velocity to a constant force of $\alpha = 100$ N near a velocity of $\frac{1}{\beta} = 0.1$ m/s.

force parameters will remain constant during each measurement period. This is because degradation takes place over a time scale much longer than the measurement period. The degradation that occurs between two measurements has an imperceptible impact on the parameter values, but these changes accumulate over the course of several months, eventually producing a noticeable change in the system’s measured response.

The core barrel’s spring-mass-damper model is created using the system’s linearized equations of motion. This model simulates the core barrel’s response to the turbulent excitation force and the nonlinear contact force over a given time interval. The spring-mass-damper model is converted to a state-space representation, maintaining the same information but in a different format. This representation expresses the core barrel system’s response as a function of several states, each of which represents a component of the core barrel’s position and velocity. The state-space representation is useful for examining the dynamics of the core barrel system and simulating its response to a given input.

The vibrational, contact, and turbulence models are combined in a simulation to generate a synthetic dataset for the core barrel system. It is important to note that the models are only combined for the purposes of data generation. Any analysis of the data requires the use of the separated models, so that changes in one model may be analyzed independent of changes in the others. The synthetic dataset is used to train a grid search algorithm and a Kalman filter to extract information regarding the contact model parameters from the ex-core measurements. The results are then compared to investigate the performance of each approach with respect to the synthetic dataset’s known contact parameters.

One method for contact parameter estimation applies a grid search algorithm to ex-core measurements taken over the course of a single day. This approach simulates the ex-core neutron measurements associated with each combination of contact force parameters on a predefined grid. The simulation for a given parameter combination is repeated multiple times, producing an ensemble of potential ex-core measurements for each parameter combination. The reactor’s actual ex-core measurements are then compared to each parameter combination’s ensemble of simulated responses. The grid search algorithm evaluates one or more performance metrics on each parameter combination. These metrics represent the parameter combination’s ability to recreate the measured ex-core data. Potential performance

metrics include the root-mean-squared error of the ensemble average with respect to the measurements, the likelihood that the measured data originated from the ensemble of simulations, and the cross-correlation between the ensemble average and the measured signal. Finally, the grid search method locates the best-performing combination of contact force parameters on the grid. This identified combination is the grid search algorithm’s estimate for the contact force parameters.

Another method estimates the contact force parameters by applying a Kalman filter to the ex-core measurements for that day. The Kalman filter method simulates the core barrel under an assumed set of contact force parameters, which are slightly perturbed at each time step. An additional feedback mechanism is applied to the core barrel system such that the simulated response’s deviation from the true measured data is minimized. This feedback mechanism causes the contact parameter estimates to migrate towards their true values over a period of time. The Kalman filter’s estimated contact force parameters are compared to the grid search method’s results to determine which method is more reliable and accurate. This is possible by applying both methods to a synthetic dataset generated with known contact force parameters.

1.5 Research Impact

Creating a model to approximate the condition of the radial keys will aid operations and maintenance (O&M) teams in scheduling the replacement of these components. Approximating the condition of the reactor’s supports reduces the required frequency of outages for inspections while minimizing the risk of failure, saving money without foregoing safety. In fact, the introduction of a tool for forecasting the condition of the radial key would ensure that the component is replaced before it degrades past a condition threshold, making the operation of the reactor safer. Knowledge regarding the health of the radial keys can be applied to prioritize the maintenance of the most degraded radial keys during scheduled outages. This would reduce the time spent inspecting and maintaining known healthy components, optimizing the use of time during an outage and potentially reducing its overall

length. If successful, the model could be extended to other components in the nuclear plant, reducing wasteful spending on unnecessary replacements and inspections during outages while potentially improving the safety of the plant.

2.0 Models of the Core Barrel System

The core barrel system is described by a combination of four separate models listed below. Each model has its own dynamics, and the models are connected through their inputs and outputs. The simulation describing the core barrel's motion incorporates all four of these models.

- Neutron Noise: The neutron noise model describes the relationship between the core barrel's response and the ex-core neutron noise measurements.
- Vibrations: The vibration model approximates the core barrel's response to some excitation force by assuming that it behaves like a spring-mass damper.
- Contact: The contact model describes the contact force applied to the core barrel at the radial key in response to its motion.
- Turbulence: The turbulence model approximates the excitation force acting on the core barrel.

The block diagram of the core barrel model is shown in Figure 6. The vibration model has two inputs: the turbulent excitation force u_1 , and the contact force u_2 . These inputs are provided by the turbulence and contact models respectively. The turbulence model currently used in the simulation is independent of the other models, while the contact model requires the velocities of the contact points as an input. These velocities y_2 are one of the two outputs produced by the vibration model, the other output being the ex-core neutron noise sensor measurements y_1 from which the motion of the core barrel is extracted.

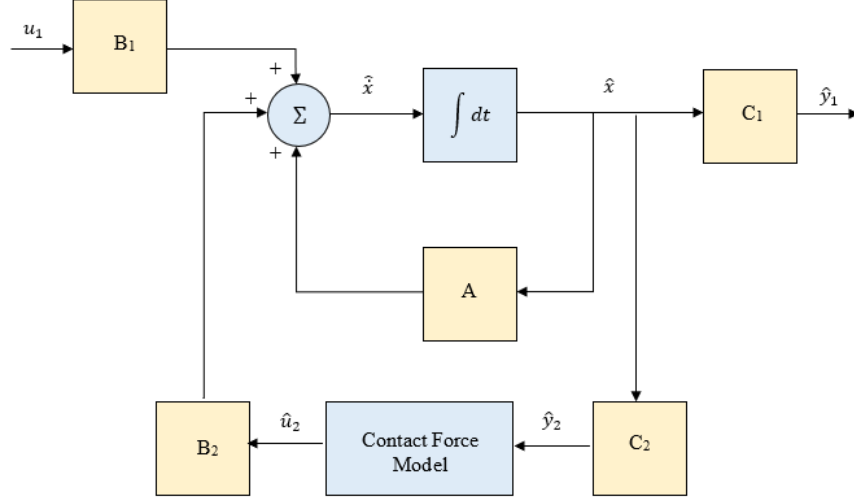


Figure 6: Block diagram of the core barrel's vibration model, using state-space notation

2.1 Neutron Noise Model

It has been documented that a PWR's ex-core neutron radiation sensors are capable of detecting the core barrel's vibrations [6]. The ex-core neutron noise measurements are directly related to the vibrations of the core barrel through the reactor core system's dynamic transfer function.

Neutron noise is classified into one of two types depending on its physical origin: power reactor noise or zero power noise. The neutron noise fluctuations detected by a PWR's ex-core radiation sensors are known as power reactor noise. Power reactor noise describes the dependence of the measured neutron noise upon mechanical and thermal noise sources within the reactor. These noise sources include any processes that introduce fluctuations in the behavior of the neutron transport medium, such as the reactor's coolant flow, the temperature dependence of the medium's material properties, and the vibrations of the core barrel [6].

The fluctuations of the medium introduce space and time fluctuations in all of the system's neutrons simultaneously in a random manner, correlating the parameters of the neu-

trons [6]. Power reactor noise is often monitored to detect malfunctions that alter the behavior of a nuclear reactor's neutron transport medium.

Another type of neutron noise, known as zero power noise, is generated by the fission process within the reactor's core [6]. However, the zero power noise's contribution to the total neutron noise measured at each ex-core sensor is negligible. This is because power reactor noise dominates the neutron noise signal for high-power reactors, such as commercial PWRs. This paper focuses on vibration-induced neutron noise generated in a PWR. Therefore the measured neutron noise is assumed to be power reactor noise, and the zero power noise is assumed to be negligible.

The reactor core is modeled as a neutron radiation source undergoing vibrations. These vibrations alter the flux of neutrons exiting the core barrel, creating fluctuations in the measured neutron radiation flux at each ex-core sensor. As a result, the vibrations are treated as a noise source for the ex-core sensors, and the vibration-induced neutron flux fluctuations $\delta\phi(t)$ are recorded as power reactor noise.

The neutron noise signal $\delta\phi(t)$ at each sensor is described by [2],

$$\delta\phi_1(t) = \delta r_1(t) + \delta P(t) + D(t) - \varphi(r(t)) + \lambda y(t) \quad (2-1)$$

$$\delta\phi_2(t) = \delta r_2(t) + \delta P(t) - D(t) - \varphi(r(t)) - \lambda y(t) \quad (2-2)$$

$$\delta\phi_3(t) = \delta r_3(t) + \delta P(t) + D(t) + \varphi(r(t)) - \lambda y(t) \quad (2-3)$$

$$\delta\phi_4(t) = \delta r_4(t) + \delta P(t) - D(t) + \varphi(r(t)) + \lambda y(t) \quad (2-4)$$

The core barrel's perturbation $r(t)$ is decomposed into its y -axis translation component $y(t)$, z -axis translation component $z(t)$, and x -axis rotation component $\theta(t)$. These perturbations contribute to the neutron noise measurements by altering the attenuation distance between the neutron radiation source and the sensors. As such, a portion of the neutron noise signal denoted by $\varphi(r(t))$ is modeled as a linear combination of the core barrel's perturbation components. Similarly, the core barrel's tilting-mode vibrations contribute to the neutron noise measurements through the approximated term $\lambda y(t)$, and the core's shell-mode vibrations induce another neutron noise component $D(t)$.

Background noise $\delta r(t)$ is present in every sensor reading, with the same broad-band characteristics between all four signals, but these components are assumed to be statistically

independent between detectors. The uncorrelated background noise present in the measurement of the i th sensor is denoted as $\delta r_i(t)$. All four measurement signals also include an identical point reactor neutron noise component $\delta P(t)$.

The neutron radiation emitted from the reactor core is attenuated through the water surrounding the core barrel. As the core vibrates, the path length from the core to the detector changes. These perturbations $r(t)$ create a change in the attenuation distance of the neutron radiation, altering the measured neutron noise. The variation in the reactor's ex-core neutron flux caused by attenuation is assumed to take the following form:

$$\delta\phi_{\text{Attenuate}}(t) \approx A \exp(\Sigma r(t)) \quad (2-5)$$

where the displacement of the core barrel $r(t)$ is multiplied by an arbitrary scaling coefficient A and the core barrel's effective cross-section Σ with respect to the core. The exponential term describing attenuation complicates the decomposition of the ex-core signal into the components expressed in Equations 2-1 to 2-4. Therefore, the variations in the neutron flux are log-normalized to simplify decomposition. This process is achieved using the relationship

$$\begin{aligned} \varphi(t) &= \ln(\delta\phi(t)) \\ &= a\Sigma r(t) \end{aligned} \quad (2-6)$$

where a is some constant scaling coefficient.

The log-normalized neutron flux variations $\varphi(t)$ detected at each sensor are expressed below. The lower sensors detect greater log-normalized flux variations because the lower end of the core barrel tends to move more than the upper end. This is reflected in the factor $(1 + b)$, where b is the decimal expression for the percent difference between the measurements of the lower and upper sensors.

$$\varphi_1(t) = a\Sigma y(t) \quad (2-7)$$

$$\varphi_2(t) = (1 + b) a\Sigma y(t) \quad (2-8)$$

$$\varphi_3(t) = a\Sigma y(t) \quad (2-9)$$

$$\varphi_4(t) = (1 + b) a\Sigma y(t) \quad (2-10)$$

The measurement noise $n(t)$ of the ex-core sensors is assumed to introduce variations about the true measured value according to a Gaussian distribution. This yields a measurement noise term of $n(t) \sim \mathcal{N}(0, \sigma^2)$, where σ is the standard deviation of the distribution. The full expression for the change in the neutron flux measured at an ex-core sensor is given below:

$$\varphi_{\text{sensor}}(t) = a\Sigma r(t) + n(t) \sim \mathcal{N}(a\Sigma r(t), \sigma^2) \quad (2-11)$$

The output of each ex-core sensor is a current I proportional to the measured ex-core neutron flux φ . Therefore, variations in the neutron flux are expressed as changes in the output current. These changes $\Delta I(t)$ are written in terms of $\varphi(t)$, $n(t)$, and $r(t)$:

$$\Delta I(t) = \varphi(t) + n(t) \sim \mathcal{N}(a\Sigma r(t), \sigma^2) \quad (2-12)$$

The core barrel system has a total of 8 ex-core sensors, 4 of which lie within the yz plane. Assuming the system is constrained to 2-D motion in the yz plane, only the 4 ex-core sensors in the plane of motion are required to describe the core barrel's motion.

$$\Delta I_1(t) = a\Sigma y(t) + n(t) \sim \mathcal{N}(a\Sigma y(t), \sigma^2) \quad (2-13)$$

$$\Delta I_2(t) = a(1+b)\Sigma y(t) + n(t) \sim \mathcal{N}(a(1+b)\Sigma y(t), \sigma^2) \quad (2-14)$$

$$\Delta I_3(t) = a\Sigma y(t) + n(t) \sim \mathcal{N}(a\Sigma y(t), \sigma^2) \quad (2-15)$$

$$\Delta I_4(t) = a(1+b)\Sigma y(t) + n(t) \sim \mathcal{N}(a(1+b)\Sigma y(t), \sigma^2) \quad (2-16)$$

2.2 Vibrational Model

The vibrations of the core barrel are found by modeling the structure as a spring-mass-damper (SMD) system with three degrees of freedom. The body is assumed to be a cylindrical mass undergoing slight horizontal, vertical, and rotational displacements within a 2-D plane. This is a simplification of the core barrel's actual motion within a 3-D space.

The 2D motion of the core barrel in the yz plane is fully described using the structure's translation along the y -axis, its translation along the z -axis, and the core barrel's rotation

about the x -axis. These 3 degrees of freedom are described using the variables y , z , and θ , respectively. The origin of the xyz coordinate system used to describe these components is located at the static equilibrium position of the core barrel's center of mass.

Modeling the core barrel's motion in a 3D space requires 2 additional degrees of freedom: the structure's translation along the x -axis, and its rotation about the y -axis. These motions are neglected in the 2D model to simplify the equations of motion. The x -axis translation and y -axis rotation must be re-introduced in a 3D model of the core barrel system to provide a more complete representation of its dynamics.

2.2.1 Core Barrel Dynamics

The core barrel system's dynamics account for the forces applied to the core barrel by the springs and dampers. The forces and moments applied by the turbulent flow of coolant in the reactor, as well as the contact forces at the radial keys, are described by separate models. A free-body diagram of the core barrel in the yz plane is shown in Figure 7.

In this diagram, Δy_A , Δz_A , Δy_B , and Δz_B are the deflections of the core barrel's upper supports along the y - and z -axes. These values are found using the geometry of the core barrel and the slight perturbations of its center of mass. The equations for computing them are

$$\Delta y_A = y + \frac{w}{2} (1 - \cos \theta) - (H - h) \sin \theta \quad (2-17)$$

$$\Delta y_B = y - \frac{w}{2} (1 - \cos \theta) - (H - h) \sin \theta \quad (2-18)$$

$$\Delta z_A = z - \frac{w}{2} \sin \theta - (H - h) (1 - \cos \theta) \quad (2-19)$$

$$\Delta z_B = z + \frac{w}{2} \sin \theta - (H - h) (1 - \cos \theta) \quad (2-20)$$

where w is the diameter of the core barrel, H is the height of the core barrel, and h is the distance from the core barrel's bottom face to its center of mass.

Points A and B represent the locations on the core barrel where the upper supports are attached, including both the hold-down springs and the horizontal supporting structures. Points C and D represent the locations of the radial keys on the surface of the core barrel. k_0 is the spring coefficient of the hold-down springs, k_1 is the spring constant for the horizontal

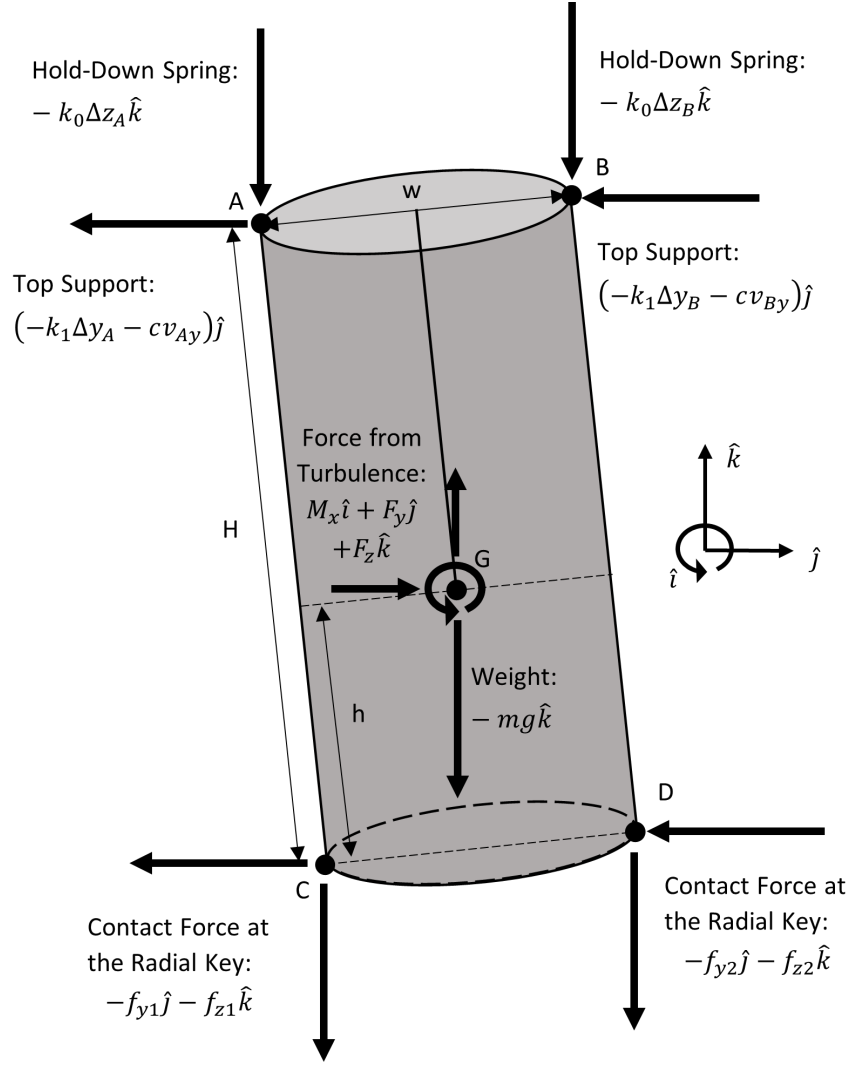


Figure 7: The free-body diagram of the core barrel, assuming all forces and motions are constrained to the yz plane. The body has a center of mass G , and its supports are attached at points A , B , C , and D .

supports, and c is the damping coefficient of the horizontal supports. The load applied by the turbulent flow is decomposed into its equivalent force components and moment at the core barrel's center of gravity. These components are denoted as M_x , F_y , and F_z . Similarly, the contact forces at the radial keys are also decomposed into their y - and z -components. The contact force components at C are labelled f_{y1} and f_{z1} , while the components at D are named f_{y2} and f_{z2} .

The equations of motion describing the core barrel's dynamics are written using either Lagrange's method or Newton's second law. If done properly, both approaches should yield the same results. Therefore, the equations of motion created using Newton's second law can be used to verify the equations found through Lagrange's method, and vice-versa. The equations of motion describing the core barrel's dynamics are then linearized using the small angle assumption. This approximation assumes that the core barrel's angle of rotation is so small that the sine of the angle is approximately equal to the angle itself in radians, and the cosine of the angle is assumed to be equal to 1.

2.2.1.1 Lagrangian Approach

Lagrange's method describes the dynamics of the system using the principle of virtual work and the law of conservation of energy. The total energy within the system is computed by summing the kinetic and potential energies of all bodies. The total value remains constant unless the system is acted upon by external or non-conservative forces, in which case the change in the total energy of the system is equal to the amount of virtual work done by the aforementioned forces. The Lagrangian, L , of the system is defined in Equation 2-23 as the difference between the total kinetic and potential energies of the system, which are represented as T and U respectively.

$$T = \frac{1}{2}mv_G^2 + \frac{1}{2}I_G\omega^2 \quad (2-21)$$

$$U = mgz + \sum \frac{1}{2}k\Delta r^2 \quad (2-22)$$

$$L = T - U \quad (2-23)$$

The total kinetic energy of the system is expressed in terms of the core barrel's mass m , the translational velocity v_G of the core barrel's center of mass, the core barrel's second moment of inertia I_G about its center of mass, and the core barrel's angular velocity ω about its center of mass. This combines both the translational and rotational kinetic energies into a single term. Similarly, the total potential energy is the sum of the core barrel's gravitational potential energy and the total spring potential energy stored in its supports. The vertical displacement of the core barrel from its equilibrium position is written as z , g is the acceleration due to gravity at the Earth's surface, k is the spring coefficient of a given support, and Δr is the distance that a given support has deflected.

The motion of the system can be described using n generalized coordinates, q_1, q_2, \dots, q_n , where n is the number of degrees of freedom within the system. This system has 3 degrees of freedom and the following generalized coordinates: $q_1 = y$, $q_2 = z$, and $q_3 = \theta$. Lagrange's method uses one equation of motion per generalized coordinate, with the k^{th} equation of motion taking the form of Equation 2-24,

$$\frac{\partial}{\partial t} \left(\frac{\partial L}{\partial \dot{q}_k} \right) - \frac{\partial L}{\partial q_k} = Q_k \quad (2-24)$$

where q_k is the k^{th} generalized coordinate and Q_k is the generalized force associated with q_k . Q_k is derived from the principle of virtual work according to Equation 2-25, where F_i is the i^{th} non-conservative or external force acting upon the system and M_j is the j^{th} non-conservative or external moment acting on the system. r_i is the position vector of the i^{th} force's point of application, and N_1 is the total number of such forces performing virtual work upon the system. Similarly, ϕ_j is the angular displacement of the system about the j^{th} moment's point of application, and N_2 is the total number of such moments performing virtual work upon the system.

$$Q_k = \sum_{n=1}^{N_1} F_i \cdot \frac{\partial r_i}{\partial q_k} + \sum_{n=1}^{N_2} M_j \cdot \frac{\partial \phi_j}{\partial q_k} \quad (2-25)$$

The external force applied to the core barrel by the turbulence at point G is expressed as F_G , and the moment applied by the turbulence at G is written as M_G . Similarly, the contact forces applied to the core barrel at points C and D are represented by F_C and F_D . No moments are applied to points C and D, although the contact forces will generate moments

due to their offset from the core barrel's axis of rotation. So, the expressions M_C and M_D for the moments applied to points C and D are equal to zero.

Each external force and moment can be separated into its x -, y -, and z -components. F_y is the y -component of F_G , F_z is the z -component of the turbulent force, and the moment applied by turbulence is given as M_x about the x -axis. Assuming the core barrel moves in the yz plane, the translational motion of the core barrel along the x -axis is restricted, and the core barrel cannot rotate about the y -axis. Additionally, the radial keys constrain the core barrel such that it cannot rotate about the z -axis. As a result, no virtual work can be done by the x -component of F_G , nor can the y or z -components of M_G perform any virtual work on the system. These components are given by F_x , M_y , and M_z , and they still appear in the equations for the forces and moments acting on the core barrel, but they will not appear in any of the generalized force terms because they perform no virtual work.

The contact forces F_C and F_D oppose the motion of the core barrel. Since the core barrel is assumed to remain in the yz plane, it cannot move along the x -axis, and so the x -component of each contact force will be zero. The y - and z -components of F_C are represented by f_{y1} and f_{z1} , while the y - and z -components of F_D are given as f_{y2} and f_{z2} . The contact forces oppose the motion of the core barrel, so the virtual work they perform on the system will be negative. This is reflected in the equations for their y - and z -components, which are expressed as acting in the negative y - and z -directions. The external forces acting on the system and their components are shown in Equations 2-26 to 2-28. Similarly, the external moments applied to the system are expressed in Equations 2-29 and 2-30.

$$F_G = F_x\hat{i} + F_y\hat{j} + F_z\hat{k} \quad (2-26)$$

$$F_C = -f_{y1}\hat{j} - f_{z1}\hat{k} \quad (2-27)$$

$$F_D = -f_{y2}\hat{j} - f_{z2}\hat{k} \quad (2-28)$$

$$M_G = M_x\hat{i} + M_y\hat{j} + M_z\hat{k} \quad (2-29)$$

$$M_C = M_D = 0 \quad (2-30)$$

The turbulent forces are assumed to act on the core barrel's center of gravity G, while the contact forces act on the contact points at the radial keys C and D. The position vectors

associated with these application points are expressed in Equations 2-31 to 2-35

$$r_G = y\hat{j} + z\hat{k} \quad (2-31)$$

$$\phi_G = \theta\hat{i} \quad (2-32)$$

$$r_C = \left(-\frac{w}{2} + y + h\theta\right)\hat{j} + \left(-h + z - \frac{w}{2}\theta\right)\hat{k} \quad (2-33)$$

$$r_D = \left(\frac{w}{2} + y + h\theta\right)\hat{j} + \left(-h + z + \frac{w}{2}\theta\right)\hat{k} \quad (2-34)$$

$$\phi_C = \phi_D = 0 \quad (2-35)$$

where w is the diameter of the core barrel and h is the distance from the core barrel's bottom face to its center of mass. These position vectors represent the location of each point with respect to the core barrel's center of mass at the equilibrium position. r_G gives the current location of the core barrel's center of mass, while r_C and r_D give the locations of the radial key contact points. ϕ_G is the angular displacement of the core barrel about its center of mass. Since the core barrel doesn't rotate about points C or D, the angular displacements ϕ_C and ϕ_D about those points are zero.

By using the center of mass at the equilibrium position as a reference point, the position vectors take the motion of the core barrel into account, becoming functions of the generalized coordinates $q_1 = y$, $q_2 = z$, and $q_3 = \theta$. The vectors are used in Equation 2-25 to find the generalized forces Q_1 , Q_2 , and Q_3 acting on the system. The expanded forms of the generalized forces are shown in Equations 2-36 to 2-38. The values of F_G , F_C , F_D , r_G , r_C , and r_D are substituted into these equations and simplified.

$$Q_1 = F_G \cdot \frac{\partial r_G}{\partial y} + F_C \cdot \frac{\partial r_C}{\partial y} + F_D \cdot \frac{\partial r_D}{\partial y} = F_y - f_{y1} - f_{y2} \quad (2-36)$$

$$Q_2 = F_G \cdot \frac{\partial r_G}{\partial z} + F_C \cdot \frac{\partial r_C}{\partial z} + F_D \cdot \frac{\partial r_D}{\partial z} = F_z - f_{z1} - f_{z2} \quad (2-37)$$

$$\begin{aligned} Q_3 &= F_G \cdot \frac{\partial r_G}{\partial \theta} + F_C \cdot \frac{\partial r_C}{\partial \theta} + F_D \cdot \frac{\partial r_D}{\partial \theta} + M \cdot \frac{\partial \phi_G}{\partial \theta} \\ &= M_x - h(f_{y1} + f_{y2}) + \frac{w}{2}(f_{z1} - f_{z2}) - h\theta(f_{z1} + f_{z2}) - \frac{w}{2}\theta(f_{y1} - f_{y2}) \end{aligned} \quad (2-38)$$

The expression for Q_3 is linearized by assuming that the generalized force terms multiplied by $\theta \ll 1$ are negligible. The linearized generalized force expression for Q_3 is as follows:

$$Q_3 = M_x - h(f_{y1} + f_{y2}) + \frac{w}{2}(f_{z1} - f_{z2}) \quad (2-39)$$

The kinetic energy of the system is computed as a function of both time and the generalized coordinates using Equation 2-40. The potential energy of the system is expressed in a similar manner through Equation 2-41. In these equations, $I_{G_{xx}}$ is the core barrel's second moment of inertia along the x -axis at the center of mass.

$$T = \frac{1}{2}m(\dot{y}^2 + \dot{z}^2) + \frac{1}{2}I_{G_{xx}}\dot{\theta}^2 \quad (2-40)$$

$$U = mgz + \frac{1}{2}k_1(\Delta y_A^2 + \Delta y_B^2) + \frac{1}{2}k_0(\Delta z_A^2 + \Delta z_B^2) \quad (2-41)$$

Δy_A , Δz_A , Δy_B , and Δz_B are the deflections of the core barrel's upper supports along the y - and z -axes. These values are found using the geometry of the core barrel and the slight perturbations of its center of mass, as shown in Equations 2-42 to 2-45.

$$\Delta y_A = y + \frac{w}{2}(1 - \cos \theta) - (H - h)\sin \theta \quad (2-42)$$

$$\Delta y_B = y - \frac{w}{2}(1 - \cos \theta) - (H - h)\sin \theta \quad (2-43)$$

$$\Delta z_A = z - \frac{w}{2}\sin \theta - (H - h)(1 - \cos \theta) \quad (2-44)$$

$$\Delta z_B = z + \frac{w}{2}\sin \theta - (H - h)(1 - \cos \theta) \quad (2-45)$$

For the equations above, w is the diameter of the core barrel, H is the height of the core barrel, and h is the distance from the core barrel's bottom face to its center of mass. Points A and B represent the locations on the core barrel where the upper supports are attached, including both the hold-down springs and the horizontal supporting structures. k_0 is the spring coefficient of the hold-down springs, k_1 is the spring constant for the horizontal supports, and c is the damping coefficient of the horizontal supports.

The resulting values for the system's kinetic and potential energy are used to find the Lagrangian, which is then substituted into Equation 2-24. One equation is found for each generalized coordinate, and the system of equations is linearized using the small angle approximation. The linearized equations of motion describing the core barrel's dynamics using Lagrange's method for y , z , and θ are

$$m\ddot{y} + 2c\dot{y} - 2c(H - h)\dot{\theta} + 2k_1y - 2k_1(H - h)\theta = -f_{y1} - f_{y2} + F_y \quad (2-46)$$

$$m\ddot{z} + 2k_0z = -mg - f_{z1} - f_{z2} + F_z \quad (2-47)$$

$$\begin{aligned}
I_{G_{xx}}\ddot{\theta} - 2c(H-h)\dot{y} + 2c(H-h)^2\dot{\theta} - 2k_1(H-h)y \\
+ 2\left[k_0\left(\frac{w}{2}\right)^2 + k_1(H-h)^2\right]\theta - 2k_0(H-h)z\theta \\
= -h(f_{y1} + f_{y2}) - \frac{w}{2}(-f_{z1} + f_{z2}) \\
- \frac{w}{2}(f_{y1} - f_{y2})\theta - h(f_{z1} + f_{z2})\theta + M_z \quad (2-48)
\end{aligned}$$

2.2.1.2 Newtonian Approach

Newton's second law describes the dynamics of the core barrel using the body's acceleration, inertia, and the net forces and moments acting upon it. Equation 2-49 describes the acceleration of the core barrel \ddot{y} along the y -axis in terms of the net force acting on the core barrel in that direction. Similarly, Equation 2-50 defines the z -axis acceleration \ddot{z} of the core barrel using the net force acting along the z -axis. Equation 2-51 provides the angular acceleration $\ddot{\theta}$ about the x -axis in terms of the net moment about the x -axis. In these equations, v_{Ay} and v_{By} are the translational velocities of the core barrel's upper support points in the y -direction.

$$\sum F_y = -(k_1\Delta y_A + cv_{Ay}) - (k_1\Delta y_B + cv_{By}) - f_{y1} - f_{y2} + F_y = m\ddot{y} \quad (2-49)$$

$$\sum F_z = -k_0\Delta z_A - k_0\Delta z_B - f_{z1} - f_{z2} - mg + F_z = m\ddot{z} \quad (2-50)$$

$$\sum M_x = (r_A \times F_A + r_B \times F_B + r_C \times F_C + r_D \times F_D) \cdot \hat{i} + M_x = I_{G_{xx}}\ddot{\theta} \quad (2-51)$$

The moments are expressed as cross products between the forces acting on the core barrel and the position vectors indicating their locations of applications. F_A and F_B are the forces applied to the core barrel by its upper supports, which are located at r_A and r_B with respect to the center of mass. F_C and F_D are the contact forces applied to the radial keys at r_C and r_D . Equation 2-52 expands the net moment equation by substituting the vectors and evaluating the cross products.

$$\begin{aligned}
\sum M_x = I_{G_{xx}} \ddot{\theta} = M_x &+ \left(-\frac{w}{2} \sin \theta + (H - h) \cos \theta \right) (k_1 \Delta y_A + c v_{Ay}) \\
&+ \left(\frac{w}{2} \cos \theta + (H - h) \sin \theta \right) k_0 \Delta z_A + \left(\frac{w}{2} \sin \theta + (H - h) \cos \theta \right) (k_1 \Delta y_B + c v_{By}) \\
&- \left(\frac{w}{2} \cos \theta - (H - h) \sin \theta \right) k_0 \Delta z_B + \left(\frac{w}{2} \cos \theta - h \sin \theta \right) f_{z1} \\
&- \left(\frac{w}{2} \sin \theta + h \cos \theta \right) f_{y1} - \left(\frac{w}{2} \cos \theta + h \sin \theta \right) f_{z2} - \left(-\frac{w}{2} \sin \theta + h \cos \theta \right) f_{y2} \quad (2-52)
\end{aligned}$$

The horizontal velocities of points A and B can be computed using Equations 2-53 and 2-54. These expressions can be substituted into Equations 2-49 through 2-52 to expand the equations of motion.

$$v_{Ay} = \dot{y} + \frac{w}{2} \dot{\theta} \sin \theta - (H - h) \dot{\theta} \cos \theta \quad (2-53)$$

$$v_{By} = \dot{y} - \frac{w}{2} \dot{\theta} \sin \theta - (H - h) \dot{\theta} \cos \theta \quad (2-54)$$

Once fully expanded, the equations of motion found using Newton's second law are linearized using the small angle approximation to produce the system's final simplified linear system of equations. The linearized equations of motion describing the core barrel's dynamics using Newton's second law for y , z , and θ are expressed below.

$$m \ddot{y} + 2c \dot{y} - 2c(H - h) \dot{\theta} + 2k_1 y - 2k_1(H - h) \theta = -f_{y1} - f_{y2} + F_y \quad (2-55)$$

$$m \ddot{z} + 2k_0 z = -mg - f_{z1} - f_{z2} + F_z \quad (2-56)$$

$$\begin{aligned}
I_{G_{xx}} \ddot{\theta} - 2c(H - h) \dot{y} + 2c(H - h)^2 \dot{\theta} - 2k_1(H - h)y \\
+ 2 \left[k_0 \left(\frac{w}{2} \right)^2 + k_1(H - h)^2 \right] \theta - 2k_0(H - h)z\theta \\
= -h(f_{y1} + f_{y2}) - \frac{w}{2}(-f_{z1} + f_{z2}) \\
- \frac{w}{2}(f_{y1} - f_{y2})\theta - h(f_{z1} + f_{z2})\theta + M_x \quad (2-57)
\end{aligned}$$

2.2.1.3 Equations of Motion

The same equations of motion for the core barrel's dynamics are found using Lagrange's method and Newton's second law. Therefore, both approaches are equally valid for deriving the system of equations that model the motion of the core barrel for the given assumptions. Despite attempts at linearizing the equations of motion via the small angle approximation, nonlinear terms remain within the equation describing the rotational motion of the system. The nonlinear terms are made negligible by assuming that the products of θ with z , f_{y1} , f_{y2} , f_{z1} , and f_{z2} are small. Such an assumption eliminates the $z\theta$, $(f_{y1} - f_{y2})\theta$, and $(f_{z1} + f_{z2})\theta$ terms from the system of equations, fully linearizing the equations of motion. This allows the system's dynamics to be represented using a linear state space representation (SSR). The fully-linearized equations of motion representing the core barrel's spring-mass-damper system are shown below:

$$m\ddot{y} + 2c\dot{y} - 2c(H - h)\dot{\theta} + 2k_1y - 2k_1(H - h)\theta = -f_{y1} - f_{y2} + F_y \quad (2-58)$$

$$m\ddot{z} + 2k_0z = -mg - f_{z1} - f_{z2} + F_z \quad (2-59)$$

$$\begin{aligned} I_{G_{xx}}\ddot{\theta} - 2c(H - h)\dot{y} + 2c(H - h)^2\dot{\theta} - 2k_1(H - h)y \\ + 2\left[k_0\left(\frac{w}{2}\right)^2 + k_1(H - h)^2\right]\theta \\ = -h(f_{y1} + f_{y2}) - \frac{w}{2}(-f_{z1} + f_{z2}) + M_x \end{aligned} \quad (2-60)$$

2.2.2 Continuous-Time State Space Representation

The equations of motion are written in matrix form as

$$M\ddot{r} + \bar{C}\dot{r} + Kr = \bar{B}_1u_1 + \bar{B}_2u_2 \quad (2-61)$$

The position vector r , contact force input vector u_1 , and turbulent force input vector u_2 for the core barrel are

$$r = \begin{bmatrix} y \\ z \\ \theta \end{bmatrix}, \quad u_1 = \begin{bmatrix} F_y \\ F_z \\ M_x \end{bmatrix}, \quad u_2 = \begin{bmatrix} f_{y1} \\ f_{y2} \\ f_{z1} \\ f_{z2} \end{bmatrix} \quad (2-62)$$

The mass matrix M is a collection of mass and inertia terms from the equations of motion, while the stiffness terms are brought into the stiffness matrix K . The input matrix \bar{B}_2 represents each equation's dependence upon the elements of the model's contact force vector u_2 , and \bar{B}_1 represents the dependencies upon the turbulent forcing vector u_1 . The elements of these matrices are as follows:

$$M = \begin{bmatrix} m & 0 & 0 \\ 0 & m & 0 \\ 0 & 0 & I_{G_{xx}} \end{bmatrix}, \quad K = \begin{bmatrix} 2k_1 & 0 & -2k_1(H-h) \\ 0 & 2k_0 & 0 \\ -2k_1(H-h) & 0 & 2k_1(H-h)^2 + 2k_0\left(\frac{w}{2}\right)^2 \end{bmatrix} \quad (2-63)$$

$$\bar{B}_1 = \begin{bmatrix} 1 & 0 & 0 \\ 0 & 1 & 0 \\ 0 & 0 & 1 \end{bmatrix}, \quad \bar{B}_2 = \begin{bmatrix} -1 & -1 & 0 & 0 \\ 0 & 0 & -1 & -1 \\ -h & -h & \frac{w}{2} & -\frac{w}{2} \end{bmatrix} \quad (2-64)$$

The damping matrix \bar{C} is modeled using proportional damping, which assumes the system's matrix of damping coefficients is a sum of scalings of the mass and stiffness matrices.

$$\bar{C} = 3.6M + 0.001K \quad (2-65)$$

The matrices from the equations of motion are used to create a state-space representation. The general form of a linear state-space representation is

$$\dot{x} = Ax + Bu \quad (2-66)$$

$$y = Cx + Du \quad (2-67)$$

The dynamics matrix A indicates the dependencies of each state's derivative upon the other states. The input matrix B is the influence of each input term upon each state. The output

matrix C represents the system's outputs as functions of the states. There is an input-output matrix D , but if the outputs only depend on the states, then D will be populated with zeros.

The state vector x represents the system's states, while the inputs are contained in the input vector u and the outputs in the output vector y . The state vector includes two sub-vectors: x_1 and x_2 . In the case of a spring-mass-damper system, x_1 is the position vector r and x_2 is the velocity vector \dot{r} . The input vector u and output vector y are also each composed of 2 sub-vectors. The input vector's sub-vectors are the force vectors u_1 and u_2 described in Equation 2-62.

The output vector has 2 sub-vectors of responses: y_1 represents the system's response measured by the 4 ex-core neutron sensors, and y_2 contains the y - and z -components of each contact point's velocity. y_2 is included in the output vector because the contact forces applied at the radial keys are dependent on the velocities of the contact points. y_2 is used as an input for the contact model, which then generates the contact force input u_2 for the vibration model. This links the contact model with the vibration model to form a feedback loop. The state, input, and output vectors are listed in terms of their sub-vectors:

$$x = \begin{bmatrix} x_1 \\ x_2 \end{bmatrix} = \begin{bmatrix} r \\ \dot{r} \end{bmatrix}, \quad u = \begin{bmatrix} u_1 \\ u_2 \end{bmatrix}, \quad y = \begin{bmatrix} y_1 \\ y_2 \end{bmatrix} \quad (2-68)$$

Because the input and output vectors each contain two sub-vectors, the input and output matrices are each split into two sub-matrices. The equations are then rewritten as

$$\dot{x} = Ax + B_1u_1 + B_2u_2 \quad (2-69)$$

$$y_1 = C_1x \quad (2-70)$$

$$y_2 = C_2x \quad (2-71)$$

The matrices are

$$\begin{aligned} A &= \begin{bmatrix} 0 & I \\ -M^{-1}K & -M^{-1}\bar{C} \end{bmatrix}, & B &= \begin{bmatrix} B_1 & B_2 \end{bmatrix} \\ C &= \begin{bmatrix} C_1 \\ C_2 \end{bmatrix}, & D &= \begin{bmatrix} 0 \end{bmatrix} \end{aligned} \quad (2-72)$$

and

$$\begin{aligned}
B_1 &= \begin{bmatrix} 0 \\ M^{-1}\bar{B}_1 \end{bmatrix}, & B_2 &= \begin{bmatrix} 0 \\ M^{-1}\bar{B}_2 \end{bmatrix} \\
C_1 &= \begin{bmatrix} \alpha_y & 0 & -\alpha_\theta & 0 & 0 & 0 \\ \alpha_y & 0 & \alpha_\theta & 0 & 0 & 0 \\ -\alpha_y & 0 & \alpha_\theta & 0 & 0 & 0 \\ -\alpha_y & 0 & -\alpha_\theta & 0 & 0 & 0 \end{bmatrix}, & C_2 &= \begin{bmatrix} 0 & 0 & 0 & 1 & 0 & h \\ 0 & 0 & 0 & 1 & 0 & h \\ 0 & 0 & 0 & 0 & 1 & -\frac{w}{2} \\ 0 & 0 & 0 & 0 & 1 & \frac{w}{2} \end{bmatrix}
\end{aligned} \tag{2-73}$$

where α_y and α_θ are calibration coefficients for the ex-core neutron sensors. The system's outputs are normalized by dividing the output matrices by the square root of the system norm. The norm is computed as the trace of CPC' , where the controllability gramian P is found by solving the system's Lyapunov equation in MATLAB. The normalized output matrix C_{norm} is then substituted in place of C in the system's model, resulting in a normalized output vector y_{norm} . The norm-normalized output matrix and normalized output vector are computed using

$$\text{norm} = \text{trace}(CPC') \tag{2-74}$$

$$C_{\text{norm}} = \frac{1}{\sqrt{\text{norm}}}C \tag{2-75}$$

$$y_{\text{norm}} = C_{\text{norm}}x \tag{2-76}$$

2.2.3 Discrete-Time State Space Representation

Discrete-time simulations tend to be less computationally expensive than continuous-time simulations due to the lack of interpolation for model inputs and the use of simpler approximations between time points. Therefore, the system's state-space representation is converted from the continuous-time domain to the discrete-time domain. This is achieved through discretization, where the system's response is evaluated over a series of uniform time steps. Assuming a sampling period of h , a discrete time vector is formed for the simulation, and the value of $x(t)$ is approximated at the $(k+1)^{\text{th}}$ time point using its value at the k^{th} time point. The discretized time vector and state approximation are displayed in Equation 2-77.

$$\begin{aligned}
t &= 0, h, 2h, \dots, hk, h(k+1), \dots \\
x(hk+h) &= x(hk)e^{Ah} + \int_{\tau=hk}^{hk+h} Bu(\tau)e^{A(hk+h-\tau)}d\tau
\end{aligned} \tag{2-77}$$

For a sufficiently small sampling period, the value of an input is assumed to remain constant between time steps. This approximation is known as a zero-order hold, and it is typically valid if the sampling frequency is 10 to 20 times greater than the system's fastest natural frequency. The validity of this assumption can be confirmed by extracting the eigenvalues of the state-space representation's dynamics matrix, which are equal to the natural frequencies of the system, and comparing the maximum eigenvalue to the sampling frequency.

Applying a zero-order hold to the input $u(\tau)$ over the time step h from t_k to t_{k+1} sets its value equal to a constant $u_k = u(hk)$, which exits the integral of Equation 2-77. The value of the state vector at the k^{th} time point is denoted as x_k instead of $x(hk)$ to match this notation. Similarly, the state vector at the $(k+1)^{\text{th}}$ time point is written as x_{k+1} . Also, the integral is simplified by letting $s = \tau - hk$. The rewritten and simplified equations are shown in Equation 2-78.

$$\begin{aligned}
x_{k+1} &= x_k e^{Ah} + Bu_k \int_{\tau=hk}^{hk+h} e^{A(hk+h-\tau)} d\tau \\
&= x_k e^{Ah} + Bu_k \int_{s=0}^h e^{A(h-s)} d\tau \\
&= x_k e^{Ah} + Bu_k e^{Ah} \int_{s=0}^h e^{-As} d\tau
\end{aligned} \tag{2-78}$$

The newly-simplified equation is rewritten in matrix form to create a discrete state-space representation with a discrete dynamics matrix F and a discrete input matrix G through Equation 2-79.

$$\begin{aligned}
F &= e^{Ah} \\
G &= B \int_{s=0}^h e^{A(h-s)} ds \\
&= A^{-1} (e^{Ah} - I) B \\
x_{k+1} &= Fx_k + Gu_k
\end{aligned} \tag{2-79}$$

Alternatively, the system's continuous-time state-space representation can be discretized for a given sample period using MATLAB's `c2d` command. This uses the methods listed above to change the dynamics and input matrices of the SSR from A and B to F and G without manually discretizing the system of equations. Discretization changes the system of differential equations describing \dot{x} into an approximately equivalent system of difference equations describing x_{k+1} .

The continuous-time output vector $y(t)$ is discretized such that $y(hk) = y_k$ to match the notation of x_k and u_k . The output equation then becomes

$$y_k = Cx_k$$

The output matrix is unaltered by the discretization process because both the continuous-time and discrete-time output equations express the values of the output vector at a given point in time as a function of the state vector at that same time.

The input and output matrices of the system's continuous-time state-space representation contain sub-matrices, as expressed in Equations 2-72 and 2-73. The output matrix is unaltered by discretization, so its submatrices remain unchanged. However, the process of discretization changes the continuous-time input matrix B into the discrete input matrix G according to Equation 2-79. Therefore, the discrete input matrix has submatrices G_1 and G_2 following the same structure as B :

$$\begin{aligned} G &= \begin{bmatrix} G_1 & G_2 \end{bmatrix} \\ G_1 &= A^{-1} (e^{Ah} - I) B_1 \\ G_2 &= A^{-1} (e^{Ah} - I) B_2 \end{aligned}$$

The discretized system of equations is written in terms of the separated inputs and outputs:

$$\begin{aligned} x_{k+1} &= Fx_k + G_1u_{1,k} + G_2u_{2,k} \\ y_{1,k} &= C_1x_k \\ y_{2,k} &= C_2x_k \end{aligned} \tag{2-80}$$

2.3 Turbulence Model

The load applied by the coolant's turbulent flow is represented by the components of the equivalent force and moment applied at the core barrel's center of mass. This load is the driving force exciting the core barrel system, and its components are modeled as scalings of averaged Gaussian white noise to reflect the random and chaotic nature of turbulence. The components of the turbulent load approximated through this model are collected within the input force vector u_1 and used as an input to the core barrel system's vibrational model.

$$u_1 \sim \mathcal{N}(0, \sigma) \quad (2-81)$$

2.4 Contact Model

The contact model approximates the forces acting on the core barrel's points of contact. These contact forces depend on the velocities of the contact points y_2 , and they change as the core barrel's radial keys degrade. Therefore, the degradation on the radial keys is approximated by analyzing how the contact forces change over time, which is reflected in the response of the core barrel. The y - and z -components of the contact forces at each radial key are collected in the contact force vector u_2 .

The contact force was initially assumed to be a linearly viscous force, which is a friction force proportional to the contact point's velocity, and each radial key was represented by a spring and a viscous damper in parallel. This model assumed the friction force acting on the radial key was a linearly viscous force proportional to the contact point's velocity and acting in the opposite direction. This commonly occurs when an object moves through a viscous fluid.

The radial keys were assumed to have the same spring rates and damping coefficients as the horizontal supports. However, this linearly-viscous contact force model did not capture the nonlinear contact mechanics inherent to the radial key, such as the constant Coulomb friction that dominates the contact force at higher contact speeds. The contact force is best

described by a function that transitions from linearly-viscous damping to constant Coulomb friction near some characteristic velocity v_c . This is accomplished using a hyperbolic tangent function of the velocities of the contact points. As a result, a hyperbolic tangent contact force model is used in this report instead of the original linearly-viscous model.

2.4.1 Viscous Damping and Coulomb Friction Contact Models

Each radial key was initially modeled as a spring and a viscous damper attached to the point of contact in parallel. Viscous damping was assumed because most non-conservative internal forces within spring-mass-damper systems are approximated as viscous dampers. Additionally, the radial keys are submerged in the reactor's coolant, which could introduce viscous friction at the radial keys when they move through the water. The viscous damping contact force served as an early test for the vibration model to ensure that it was working properly. Its application was simpler than a nonlinear contact model because it was compatible with MATLAB's linear solver tool `lsim`. The `lsim` solver required the vibration model's dynamics and the contact model's mechanics to be combined into a single SSR. This recombination conflated changes in the vibration model with changes in the contact model, re-introducing confusion between their effects on the core barrel's overall behavior.

As the contact point velocity approaches infinity, the observed contact force approaches a constant value. This is consistent with a Coulomb force model, where the friction force opposing the object's motion is independent of velocity. However, the Coulomb force model contradicts the core barrel's aforementioned viscous behavior at low contact point velocities. This discrepancy in behavior indicates that the viscous and Coulomb models could be combined to form a more comprehensive contact model, such as the hyperbolic tangent model.

2.4.2 Hyperbolic Tangent Contact Model

When the contact point's velocity is low, the contact force acts like a viscous damping force. At high velocities, the contact force behaves more like a constant Coulomb friction force. These two different behaviors are combined into a single model by approximating the

contact force as a function of the hyperbolic tangent of the contact point's velocity. As the velocity of the contact point approaches infinity in the positive or negative direction, the contact force resisting the core barrel's motion asymptotically approaches a constant value. This represents Coulomb friction, which is constant with respect to velocity. In contrast, the contact force is almost linearly related to velocity at lower velocities. This represents viscous damping, where the friction force resisting the motion of the contact point is proportional to its velocity. The hyperbolic tangent model transitions between viscous and Coulomb friction near some characteristic velocity v_c .

This contact model includes two unknown parameters, α and β . The parameter α represents a scaling of the Coulomb friction's magnitude, while β defines the characteristic velocity $v_c = 1/\beta$ where the model transitions between friction forces. These two parameters are used to define the equivalent damping coefficient $\gamma = \alpha\beta$ for velocities below v_c . The hyperbolic tangent contact model for the core barrel system is

$$u_2 = \alpha \tanh(\beta y_2) \tag{2-82}$$

3.0 Synthetic Data Generation

Synthetic data is generated for the core barrel model established in Chapter 3. This dataset should approximate the behavior of an actual core barrel, functioning as the “measurement” for each contact parameter estimation method. The best-performing estimation method should generate a response that reliably approximates the behavior of the synthetic dataset’s outputs.

Most synthetic data generation methods rely on integrating the core barrel’s state space equations of motion. MATLAB’s `lsim` simulation command can reliably integrate the state space equations of a linear system in the continuous-time domain, but this solver is incompatible with nonlinear systems. Instead, an iterative discrete-time approach is recommended for nonlinear systems such as the core barrel.

Discrete-time solvers are generally faster than continuous-time solvers because numerical integration in the discrete-time domain is approximated as an iterative sum over finite time steps rather than an integral over a period of time. These methods require discretizing the continuous-time system, transforming it from the continuous-time domain to the discrete-time domain. The discretization process must account for all dynamics in the continuous-time system, including the nonlinear feedback mechanics introduced by the contact force model.

Alternatively, some algorithms integrate a system of equations by locally approximating the continuous-time system as a polynomial and iteratively solving the system at discrete points in time through a Taylor series approximation. These continuous-time solvers are typically slower than their discrete-time counterparts, but they do not require the discretization of the system’s model. This is especially useful in systems with feedback mechanics not included in the state-space representation. Continuous-time solvers include Euler’s method and Runge-Kutta methods. A fourth-order Runge-Kutta method is applied to the core barrel system’s continuous-time model for synthetic data generation.

3.1 Discrete-Time State Space

An iterative solver approach is necessary to accommodate the core barrel model's non-linear contact force. The discrete-time iterative method for solving a system of equations is faster and less computationally-expensive than the continuous-time integration methods.

One discrete-time method involves discretizing the state space matrices through a zero-order hold. This assumption asserts that the system's continuous-time input $u(t)$ remains constant for the duration of each time step. For example, if a system's input u at time $t_k = hk$ is known to be u_k , the value of that input some time period $\tau < h$ after t_k could be approximated using a zero-order hold as follows:

$$u(hk + \tau) \approx u(hk) = u_k \quad (3-1)$$

The zero-order hold assumption simplifies the system's discretization process by setting the input equal to a constant value over the course of each time step, thereby allowing it to be factored out of integrals.

The continuous-time state space model's solution for the state $x(t)$ at time $t = hk + h$ using the state and input from time $t = hk$ is expressed as

$$x(hk + h) = x(hk)e^{Ah} + \int_{\tau=hk}^{hk+h} Bu(\tau)e^{A(hk+h-\tau)}d\tau \quad (3-2)$$

where the values of the state space matrices A and B are constant.

Using the zero-order hold assumption, the input $u(\tau)$ remains constant over the solution's integral from $\tau = hk$ to $\tau = hk + h$. The input is factored out of the integral expression alongside the system's input matrix B .

$$\int_{\tau=hk}^{hk+h} Bu(\tau)e^{A(hk+h-\tau)}d\tau \approx Bu_k \int_{\tau=hk}^{hk+h} e^{A(hk+h-\tau)}d\tau \quad (3-3)$$

The integral is then combined with B to form the discrete-time state space representation's input matrix G :

$$G \approx B \int_{\tau=hk}^{hk+h} e^{A(hk+h-\tau)}d\tau \quad (3-4)$$

The zero-order hold approximation thereby simplifies the system of equations.

The discretization of a continuous-time state space model through a zero-order hold is achieved in MATLAB using the `c2d` function. This function's required inputs are the continuous-time state space representation of the system and the sample period for discretization.

3.1.1 Structure

The response of the discretized state space representation is iteratively computed by solving for the value of the state vector at the next time step using the current time step. The discrete-time state space model takes the form shown below:

$$x_{k+1} = Fx_k + G_1u_{1,k} + G_2u_{2,k} \quad (3-5)$$

$$y_{1,k} = C_1x_k \quad (3-6)$$

$$y_{2,k} = C_2x_k \quad (3-7)$$

The system's input, output, and state vectors at each time point are stored in matrices that compile the vectors for all of the time points. For example, the state vector x evaluated at the N th time point is stored as the $(N - 1)$ th column of the state matrix X . Similarly, the output vector matrices Y_1 and Y_2 contain the output vectors at each time point, and the input vector matrices U_1 and U_2 are populated with the input vectors. These matrices are initialized prior to any iterative solving of the system. These matrices are initially populated with zeros, with the exception of the first state vector of the state matrix, which is the system's initial condition.

Within each iteration of the system, the inputs and outputs are solved for the current time step using the values of the current state vector. The inputs are then used alongside the current state to evaluate the system's state vector at the next time step. This process is iterated over every time step in the system's time span until the matrices are fully populated. The resulting matrices describe the system's inputs, outputs, and states at the discrete time points listed in the time vector. In theory, this discrete-time simulation reflects the response of the core barrel system to a turbulent excitation force while undergoing a nonlinear contact force.

The discrete-time simulation is used to generate synthetic data for the core barrel system. This requires populating the dynamic matrices, providing an initial condition for the state vector x , setting the magnitude of the turbulent load's white noise function u_1 , and specifying the contact force parameters. The simulation creates a set of matrices representing the input, state, and output vectors at every discrete time point. The matrix associated with the measured output vector y_2 is used as the system's synthetic response data.

The MATLAB code for the discrete-time simulation associated with a single replication of a single parameter combination is shown in Appendix B. The variable 'rep_id' identifies the index of the replication, while 'alpha' and 'beta' are the values of α and β for the specified parameter combination. The two functions `turb()` and `contact(Y2)` generate the turbulent and contact forces. They are defined before the for-loop, as are the discretized state space matrices F , G_1 , G_2 , C_1 , and C_2 .

3.1.2 Reasons to Avoid Using Discrete State Space

As previously mentioned, the discrete-time solver method is faster and less computationally expensive than continuous-time methods. However, the discrete-time computation shown above cannot fully replicate the system's continuous-time response due to flaws in the state space discretization process. The feedback mechanism relating the velocity output y_2 and the contact force input u_2 is neglected in the discretization process because the nonlinear contact force is applied outside of the state space model's dynamics matrix. This is shown by examining the impact of discretization on the system if the contact force were a linear-viscous damper. If the contact force is approximated as a linear function $u_2 = \gamma y_2$ where $\gamma \approx \alpha\beta$, the continuous-time state space representation becomes:

$$\begin{aligned}\dot{x} &= Ax + B_1u_1 + B_2u_2 \\ &= Ax + B_1u_1 + B_2\alpha\beta y_2\end{aligned}\tag{3-8}$$

$$y_1 = C_1x\tag{3-9}$$

$$y_2 = C_2x\tag{3-10}$$

Substituting for y_2 , the state space representation is simplified to the following expression:

$$\begin{aligned}\dot{x} &= Ax + B_1u_1 + B_2\alpha\beta C_2x \\ &= (A + B_2\alpha\beta C_2)x + B_1u_1\end{aligned}\tag{3-11}$$

$$y_1 = C_1x\tag{3-12}$$

The term $(A + B_2\alpha\beta C_2)$ is collected into a single equivalent dynamics matrix A_c . This yields a simplified state space representation as follows:

$$\dot{x} = A_c x + B_1 u_1\tag{3-13}$$

$$y_1 = C_1 x\tag{3-14}$$

The input matrix and newly-formed equivalent dynamics matrix are discretized, yielding the discrete-time state space model shown below:

$$x_{k+1} = F_c x_k + G_{c1} u_{1,k}\tag{3-15}$$

$$y_{1,k} = C_1 x_k\tag{3-16}$$

However, if the continuous-time state space representation shown in Equation 3-10 were discretized before substituting $u_2 = \alpha\beta C_2 x$, then the discrete-time state space model would instead be of the form shown in Equation 3-7. The discretization process uses a zero-order hold method, which assumes the inputs u_1 and u_2 have constant values within each time step. However, the contact force's dependence on the system's output may contradict the zero-order hold assumption. If y_2 varies between discrete time points, then u_2 must also vary between the time points. One way to confirm the validity of the assumption is to compare two state space models: one where the contact force function is substituted before discretization, and one where the function is substituted after discretization. If the two expressions are equivalent, then the zero-order hold assumption is valid for the contact force u_2 .

The discrete-time state space representations expressed in Equations 3-16 and 3-7 are only equivalent if the expressions for x_{k+1} are equivalent. The expression from Equation 3-7 is expanded below:

$$\begin{aligned}
x_{k+1} &= Fx_k + G_1u_{1,k} + G_2u_{2,k} \\
&= Fx_k + G_1u_{1,k} + G_2\alpha\beta C_2x_k \\
&= (F + \alpha\beta G_2C_2)x_k + G_1u_{k+1}
\end{aligned} \tag{3-17}$$

Substituting the expressions for A_c , F , and G into the expressions for F_c and G_c in Equation 3-16 yields

$$\begin{aligned}
F_c &= e^{A_ch} = e^{A+\alpha\beta B_2C_2} \\
&= e^A e^{\alpha\beta B_2C_2} = F e^{\alpha\beta B_2C_2}
\end{aligned} \tag{3-18}$$

and

$$\begin{aligned}
G_{c1} &= A_c^{-1} (e^{A_ch} - I) B_1 \\
&= (A + \alpha\beta B_2C_2)^{-1} (e^{Ah} e^{\alpha\beta B_2C_2h} - I) B_1 \\
&= (A + \alpha\beta B_2C_2)^{-1} (F e^{\alpha\beta B_2C_2h} - I) B_1
\end{aligned} \tag{3-19}$$

The zero-order hold approximation cannot reasonably approximate the contact force unless the two following statements are true:

1. $\exp(A + \alpha\beta B_2C_2) = \exp(A) + A^{-1}(\exp(Ah) - I) B_2C_2$
2. $(A + \alpha\beta B_2C_2)^{-1}(\exp(Ah + \alpha\beta B_2C_2h) - I) = A^{-1}(\exp(Ah) - I)$

The requirements are both met under any of the following conditions:

- $\alpha = 0$
- $\beta = 0$
- $B_2 = 0$
- $C_2 = 0$

These conditions can only be true if the contact force u_2 has no impact on the core barrel's motion, or if the contact force is always zero. However, the condition monitoring technique for the core barrel's radial keys requires that the contact force has a measurable impact on the core barrel's response. Therefore, the zero-order hold approximation for the contact force is not valid for condition monitoring applications.

The analysis so far has focused on a contact force approximated as a linear viscous damper. As previously mentioned, the hyperbolic tangent contact force behaves like a viscous damper at low velocities and approaches a constant value as the velocity increases past some characteristic velocity. This nonlinear behavior prevents the substitution of the contact force into the state space representation. The contact force must remain outside of the state space representation as a separate input function. When discretizing the state space representation, a zero-order hold must be applied to this input. However, the viscous behavior of the contact force at low velocities can only be replicated by a zero-order hold approximation if the contact force's impact on the core barrel's motion is negligible. This violates the assumption that the contact mechanics can be extracted from the ex-core sensor readings, undermining the entire purpose of this condition monitoring application. As a result, the discrete-time method cannot accommodate the hyperbolic tangent contact force used in this condition monitoring problem. A continuous-time solver must be used instead.

3.2 Continuous-Time State Space

As shown in the previous chapter, the core barrel system's continuous-time response takes the form:

$$x(t) = x_0 \exp(At) + \int_{\tau=0}^t B_1 u_1(\tau) d\tau + \int_{\tau=0}^t B_2 u_2(\tau) d\tau \quad (3-20)$$

The computation of the true solution to this system requires integrating the inputs over the time domain. Alternatively, the integral's computation can be simplified by applying a Taylor series approximation method to the system's continuous-time state space representation. These approaches locally approximate the system's state as a polynomial function, allowing

for the computation of the solution at some small time step away from the system's initial condition. This process is then repeated for the newly-computed state value, allowing for iterative approximation of the state. The Taylor series approximation is only valid for local approximations, though. Therefore, the error in the approximated state is proportional to the approximation's time step.

The continuous-time solvers based on the Taylor series include the Newton-Euler method and Runge-Kutta methods. As the order of the polynomial used in the approximation method increases, the expected global error of the approximation decreases. For instance, the Newton-Euler method approximates the next state using a linear function, while the second-order Runge-Kutta method uses a quadratic function to approximate the next state.

A standard fourth-order Runge-Kutta approximation (RK-4) of the solution x to a general first-order differential equation $f(t_k, x_k)$ for a constant time-step width h is described as follows:

$$\dot{x}(t) = f(t, x) \quad (3-21)$$

$$x(t_0) = x_0 \quad (3-22)$$

$$t_{k+1} = t_k + h \quad (3-23)$$

$$\begin{aligned} x_{k+1} &= x_k + \frac{1}{6} (K_1 + 2K_2 + 2K_3 + K_4) h \\ &\approx x(t_{k+1}) \end{aligned} \quad (3-24)$$

where \dot{x} is the time derivative of x and x_0 is an initial condition. The values of K_1 , K_2 , K_3 , and K_4 are estimates for \dot{x} evaluated at the beginning, middle, and end of a single time step.

$$K_1 = f(t_k, x_k) \quad (3-25)$$

$$K_2 = f\left(t_k + \frac{h}{2}, x_k + h\frac{K_1}{2}\right) \quad (3-26)$$

$$K_3 = f\left(t_k + \frac{h}{2}, x_k + h\frac{K_2}{2}\right) \quad (3-27)$$

$$K_4 = f(t_k + h, x_k + hK_3) \quad (3-28)$$

The RK-4 method uses the weighted average of these slopes to approximate the system's response at the end of the time step. The error of the RK-4 approximation decreases as the width of the time step approaches zero.

In the case of the core barrel model's continuous-time state space representation, the differential equation for the RK-4 method is $\dot{x} = Ax + B_1u_1 + B_2u_2$. Substituting this equation for $f(t, x)$ in Equation 3-24 yields

$$\dot{x}(t) = Ax(t) + B_1u_1(t) + B_2u_2(t, x) \quad (3-29)$$

$$x_{k+1} \approx x_k + \frac{1}{6}(K_1 + 2K_2 + 2K_3 + K_4)h + B_1u_1(t_k) \quad (3-30)$$

where the K values are

$$K_1 = Ax_k + B_2u_2(t_k, x_k) \quad (3-31)$$

$$K_2 = A\left(x_k + h\frac{K_1}{2}\right) + B_2u_2\left(t_k + \frac{h}{2}, x_k + h\frac{K_1}{2}\right) \quad (3-32)$$

$$K_3 = A\left(x_k + h\frac{K_2}{2}\right) + B_2u_2\left(t_k + \frac{h}{2}, x_k + h\frac{K_2}{2}\right) \quad (3-33)$$

$$K_4 = A(x_k + hK_3) + B_2u_2(t_k + h, x_k + hK_3) \quad (3-34)$$

and the contact force u_2 for a provided time t and state x is given by

$$\begin{aligned} u_2(t, x) &= \alpha \tanh(\beta y_2) \\ &= \alpha \tanh(\beta C_2 x) \end{aligned} \quad (3-35)$$

The MATLAB function `ode45` uses the RK-4 approximation method to solve a system of differential equations over a specified time interval for a given initial condition.

3.2.1 Limitations Regarding White Noise

The RK-4 approximation method operates by computing the weighted average of the response's slope over a small time step. Complications may arise if the slope varies wildly over the time step, such as if the system is excited by a signal with a frequency higher than the step's associated frequency. Theoretical white noise inputs are particularly troublesome because the input randomly changes at every instant. The uppermost frequency of a theoretical white noise signal always exceeds the solver's time step frequency due to the signal's infinite frequency content. Therefore the turbulent white noise input u_1 to the continuous-time state space model varies randomly within the RK-4 solver's time step. The RK-4 approximation must account for this variation halfway through the time step, potentially leading to significant variation amongst K_1 , K_2 , K_3 , and K_4 . This variation introduces uncertainty to the weighted average slope over the time step, decreasing the accuracy of the RK-4 approximation.

In the MATLAB simulation, the turbulent input force vector must be defined over the response's time interval prior to applying the continuous-time solver. Otherwise the solver will attempt to generate a random white noise input at the beginning, middle, and end of each time step. Repeatedly calling the random number generator in this manner drastically increases the solver's computation time. Pre-defining the turbulent input force vector over the time interval is more computationally efficient.

The values of the system's turbulent input vector $u_1(t)$ are only known for the time points in its definition. The value of the input between these time steps must be approximated through methods such as interpolation. Solving the continuous-time equation would also require integrating the interpolated values over a time interval, as shown through the term $\int_{\tau=0}^t Bu(\tau)d\tau$ in Equation 3-20. Interpolating an input between its known values and integrating the result over a time interval is computationally expensive, especially if the calculation must be repeated over numerous time points.

The interpolation and integration issues are circumvented by assuming a zero-order hold approximation between data points. This assumption sets the input to a constant value between sampled data, removing the need for interpolation and allowing the integral to be

expressed as a sum of time steps scaled by the input. The integral is then expressed as

$$\int_{\tau=0}^t u_1(\tau) d\tau \approx \sum_{i=0}^n h u_1(t_i) \quad (3-36)$$

for $t = hn$.

3.2.2 Band-Limited White Noise

Truly random white noise has a uniform energy distribution over an infinite bandwidth. This results in a signal with infinite energy, which is purely theoretical. For more realistic approximations, the bandwidth of white noise is limited to the given application's frequency range of interest. The maximum frequency of the bandwidth effectively acts as a sampling frequency, defining a sample period over which the random signal is assumed to remain constant. As a result, the band-limited white noise has random values at every time point in a discrete time vector defined by the bandwidth's upper frequency limit. A zero-order hold approximation is applied between the time points, thereby maintaining the input force's status as a continuous-time signal.

The core barrel's response to turbulence is simulated using a continuous-time method with a band-limited white noise input for turbulence. The value of the input for each time interval in the band-limited signal is randomly selected from a Gaussian distribution with a specified mean and standard deviation. Normally, a continuous-time solver cannot accommodate a random input because the value changes with every time step. However, by setting the input to have a constant value within discrete time steps, the random input no longer experiences sudden changes between time points in the continuous-time domain. As a result, the input is compatible with solvers that use the continuous-time state space model, such as the Fourth-Order Runge-Kutta Approximation.

The code for the discrete-time simulation is rewritten to consider the input, output, and state vectors of the state space representation as functions. These functions are defined prior to the for-loop in the code, except for the functions describing the turbulent input force and the core barrel's equations of motion.

The turbulent force input function is defined within the simulation’s replication for-loop so that every replication of a simulation is unique. The function for the equations of motion is introduced within the for-loops that iterate over the values of α and β . This passes each value of α and β into the equation of motion for every parameter combination.

3.3 Values of Model Variables

The values of the simulation’s variables are chosen to reflect existing PWRs. These variables depend on the PWR design in question, leading to significant variations between reactors. However, the model in the simulation represents a generalized PWR, and it is not intended to reflect the response of a specific reactor.

3.3.1 Model Constants

Different PWR designs have different dimensions, so no single value for the height, width, and diameter is representative of every PWR. However, the simulation’s core barrel model should still reflect realistic values. Few nuclear plants publish information on the geometric dimensions of their PWRs, complicating the generalization of the reactor model. Thankfully, the WWER-440 and WWER-1000 PWR designs are available to the general public. The dimensions of a WWER-1000 reactor are substituted into the simulation model to ensure that the core barrel model is representative of a realistic reactor. The computations used in the simulation assume the core barrel is a 10.51 m tall cylindrical shell with an inner diameter of 3.67 m and a thickness of 65 mm. Other values may be substituted into the model to reflect different PWR designs.

Information regarding the material composition of reactor components is far more readily available than information regarding geometric dimensions. Most American PWRs use core barrels and radial keys are constructed from AISI Type-304 stainless steel [1]. This alloy has a density of approximately 8000 kg/m^3 . Assuming the core barrel model is a uniform stainless steel cylindrical shell with the dimensions defined above, the mass of the core barrel is approximately 61 metric tons.

3.3.2 Expected Measurement Noise

The ex-core neutron measurements include some noise due to imperfections in the sensors, the inherent randomness of radiation, and the turbulent coolant flow's random excitation of the core barrel. The excitation from turbulence is classified as process noise, an inherently random input to the system. The noise from the sensors and the radiation are considered measurement noise because they only offset the measured response from the system's true response. Unless an output feedback mechanism is present, measurement noise does not influence the system's states.

Due to the presence of measurement noise, only the theoretical values for the ex-core sensor measurements are proportional to the displacement of the core barrel. The measurement noise introduced by the radiation causes the measured currents to deviate from their theoretical values, obscuring the displacement of the core barrel. One way to accommodate for this noise is to create an ensemble of current measurements over multiple trials. Because the measurement noise takes the form of a Gaussian probability distribution centered on the system's theoretical output, the average value of the measurements approaches the theoretical value as the sample size increases.

However, this ensemble average does not account for the randomness introduced by the system's process noise. The randomness in the system's inputs prevents the ensemble-averaged response from converging to a single theoretical function that only depends on time.

Another method for analyzing the measured results is to partially remove the measurement noise from the simulation using a Kalman filter. Kalman filters compare the measured

output to the system model’s expected output at each discrete time step. The filter’s Kalman gain multiplies the difference between these two outputs, and the result is used to correct the model’s state estimate at the current time step through an additional feedback mechanism. The corrected state estimate is then used to approximate the state at the next time point, and the process repeats.

The value of the Kalman gain reflects the user’s trust in the measurements with respect to their trust in the model. A low Kalman gain largely ignores the model’s predictions in favor of the measurements when correcting the state estimate. This is beneficial when the model’s representation of the actual system is questionable. In contrast, a high Kalman gain weighs the model’s predicted outputs more heavily than the measurements, indicating a greater trust in the system’s model when updating the estimates. The additional weight helps combat the measurement noise’s impact on the state estimate. The Kalman filter approach is discussed in detail in a later chapter.

3.3.3 Contact Parameters

The potential values of the contact force parameters α and β are restricted to ranges defined by the physical constraints of the core barrel model. As previously mentioned, the parameter α is the maximum magnitude of the contact force, and β is the inverse of the characteristic velocity v_c at which the contact force model transitions from linearly-viscous behavior to a constant force. The contact force model is shown in Figure 8.

The value of the characteristic velocity should realistically lie somewhere in the region between zero and the reactor’s maximum contact point velocity. If the characteristic velocity were above the maximum contact point velocity, the contact force would never reach its maximum value, and the contact force model could be approximated using a linear-viscous contact model with a damping coefficient of $\gamma = \alpha\beta$. The maximum velocity at the contact point is found by simulating the core barrel’s response while setting the contact force to zero. For the core barrel system described in previous chapters, the maximum velocity at the contact point is approximately 0.86 m/s. Therefore, the hyperbolic tangent contact model only applies when the characteristic velocity is below 0.86 m/s. A characteristic

velocity of 10 m/s is included within the grid of tested values for the simulation, to illustrate the effects of a viscous contact force model on the simulation versus the hyperbolic tangent contact force model.

The lower bounds for the characteristic velocity determines not only the velocity at which the contact force settles, but also how quickly the contact force can switch from negative to positive. The contact force could theoretically change from a value of $-\alpha$ to α over a velocity change as small as $2v_c$, or vice-versa. This term $2v_c$ defines the velocity resolution at which the contact force potentially changes sign. If the contact point velocity can't be accurately determined within this interval, the contact force may suddenly change by 2α . For the core barrel, the minimum characteristic velocity is assumed to be 0.00100 m/s. These bounds of 0.001 00 m/s to 10.0 m/s for the characteristic velocity v_c are then converted into bounds of 0.100 s/m to 1000 s/m for the contact force parameter $\beta = \frac{1}{v_c}$.

The effective viscous damping coefficient γ provides a decent approximation for the contact force model's damping at lower velocities. If the characteristic velocity were above 0.86 m/s, the viscous contact force could be combined with the core barrel system's viscous damping matrix, thereby including the contact force within the state-space model's dynamics. For a value of γ below 50 N s/m, the contact force's contribution to the system's overall damping is negligible. If the contact force has a negligible impact on the core barrel system's response, the contact force parameters cannot be extracted from the ex-core measurements. If the value of γ is above 50000 N s/m, though, two of the core barrel system's modes become critically-damped. This is undesirable because a critically-damped mode causes one of the system's natural frequencies to increase far above the sensor's possible sampling frequencies, leading to aliasing issues. Therefore the value of γ should be kept between 50 and 50000 N s/m, or within a more conservative range of 100 N s/m to 10 000 N s/m. In reality, the hyperbolic tangent contact force model prevents the contact force associated with the viscous contact model from increasing above α . This decreases the actual contact force's impact on the core barrel system's dynamics. However, the bounds of 100 N s/m to 10 000 N s/m for $\gamma = \alpha\beta$ should provide an effective range for extracting the contact force parameters from the core barrel's response.

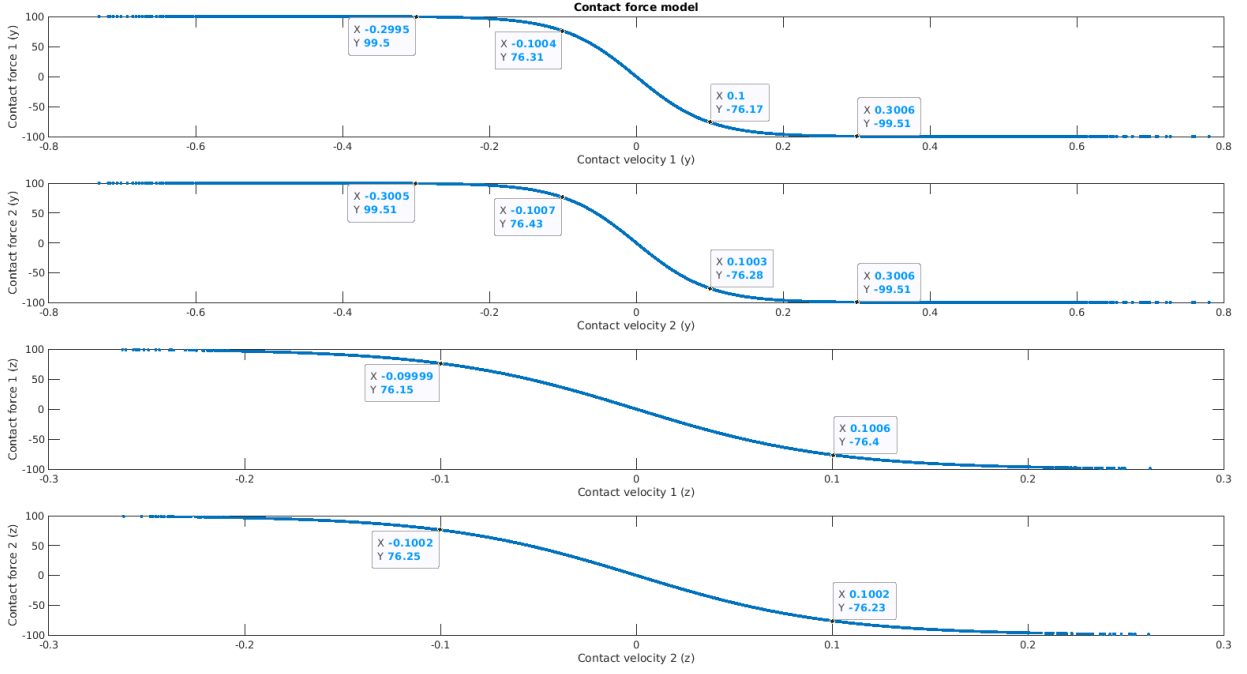


Figure 8: Relationship between the contact force and the velocity at the point of contact for $\alpha = 100$ N and $\beta = 10.0$ s/m. The characteristic velocity $v_c = 0.100$ m/s represents the contact force's transition from a nearly linear relationship to a constant value.

The range of values for the maximum contact force α are approximated by combining the limits imposed upon β and γ . This is achieved using the relationship

$$\alpha = \frac{\gamma}{\beta} = \gamma v_c \quad (3-37)$$

where v_c is the characteristic velocity. Potential values for α are found from 10 N to 100 000 N.

The parameter combinations are isolated to a logarithmically-scaled 9-by-9 grid ranging from 10 N to 100 000 N on α and from 0.100 s/m to 1000 s/m on β . The combinations with effective viscous damping coefficients outside the bounds of 100 N s/m to 10 000 N s/m are excluded from the grid. This removes 47 parameter combinations from consideration, reducing the grid from a set of 81 parameter combinations to the set of 34 shown in Figure 9.

Four synthetic datasets are generated using unique combinations of contact force parameters. The contact parameters for each dataset are estimated using both the grid search method and the Kalman filter approach. These estimates are then compared to determine which method, if any, provides a better approximation of the synthetic dataset's contact force parameters. The true parameter combinations associated with each of the synthetic datasets are listed in Table 3.

3.4 System Response

Synthetic data is generated by applying the fourth-order Runge-Kutta solver to the system's continuous-time state space model for a single combination of α and β . The dataset is structured such that it is compatible with both the Kalman filter and grid search methods for identifying the system's contact parameters. This is achieved by saving the state and output vector values for the dataset over the simulation's time interval, the state space matrices and their dimensions, the Runge-Kutta solver's discrete time step length, and the variance matrices associated with the noise sources.

The time-domain response of the system is found by running the simulation described above over the interval specified by the time vector. The system has four outputs in the output vector y_1 , each corresponding to the measurement of an ex-core radiation sensor:

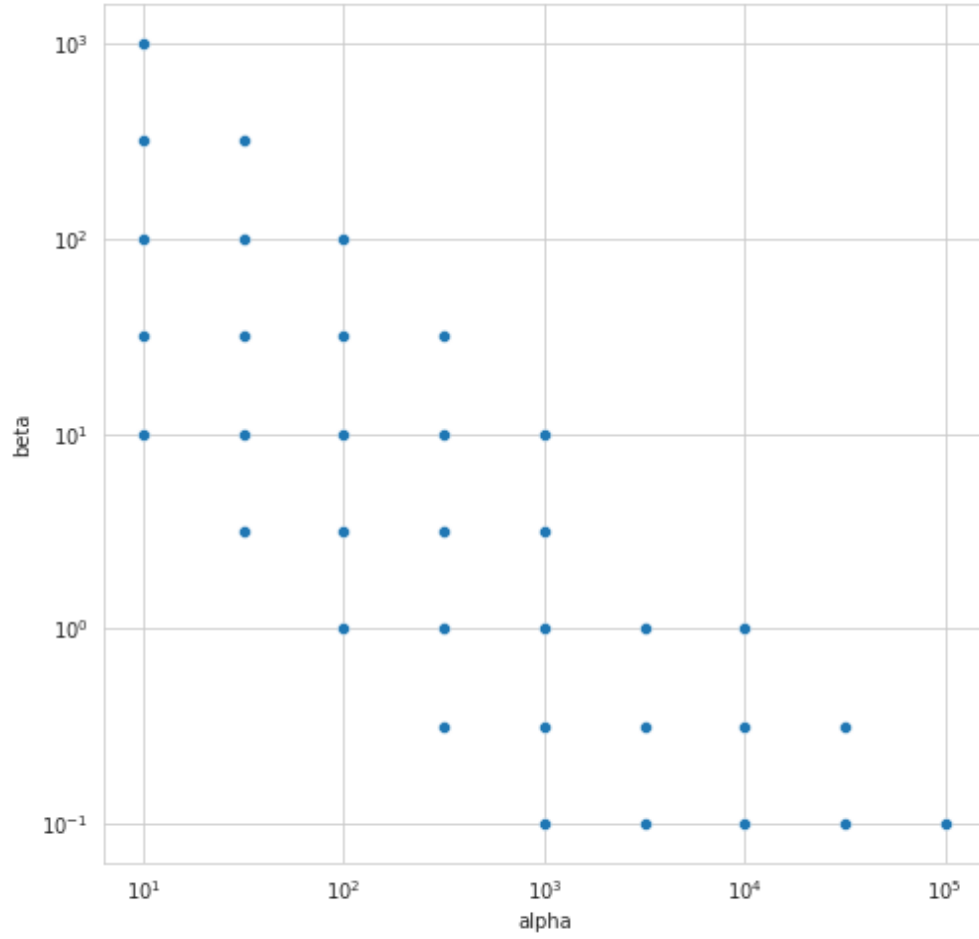


Figure 9: Grid of parameter combinations for consideration

Table 3: Contact force parameters associated with each of the four synthetic datasets

Dataset	True α (N)	True β (s/m)
Case 1	100	10.0
Case 2	31.6	316
Case 3	490	70.0
Case 4	660	110

- The first element of y_1 is I_1 , the current measured at Sensor 1.
- The second element of y_1 is I_2 , the current measured at Sensor 2.
- The third element of y_1 is I_3 , the current measured at Sensor 3.
- The fourth element of y_1 is I_4 , the current measured at Sensor 4.

The measurements at the ex-core sensors will include noise due to the inherent randomness of the neutron radiation. This noise $v(t)$ is modeled by adding Gaussian noise to the simulated currents.

$$v(t) \sim \mathcal{N}(0, \sigma^2) \quad (3-38)$$

The system's outputs are the difference between each ex-core sensor's output current at a given time and the steady-state current constantly emitted from the sensor, I_0 ; that is, we subtract the mean response of the sensors. The system's sensor outputs are linear combinations of the linear displacement y and angular displacement θ ,

$$y_1 = \begin{bmatrix} I_1 - I_0 \\ I_2 - I_0 \\ I_3 - I_0 \\ I_4 - I_0 \end{bmatrix} = \begin{bmatrix} \alpha_y y - \alpha_\theta \theta + v(t) \\ \alpha_y y + \alpha_\theta \theta + v(t) \\ -\alpha_y y + \alpha_\theta \theta + v(t) \\ -\alpha_y y - \alpha_\theta \theta + v(t) \end{bmatrix} \quad (3-39)$$

where α_y and α_θ are scaling coefficients.

If the measurement noise is negligible, the output associated with Sensor 1 will be the exact opposite of the output associated with Sensor 3. The same relationship is observed between the outputs associated with Sensors 2 and 4.

$$y_1 = \alpha_y y - \alpha_\theta \theta = -y_3 \quad (3-40)$$

$$y_2 = \alpha_y y + \alpha_\theta \theta = -y_4 \quad (3-41)$$

Therefore, the current change in one sensor is the exact opposite of the current change in the other sensor on the same vertical level, assuming measurement noise is negligible.

$$I_1 - I_0 = -(I_3 - I_0) \quad (3-42)$$

$$I_2 - I_0 = -(I_4 - I_0) \quad (3-43)$$

By re-arranging these relationships, the steady-state current is computed by averaging the sensor current readings of the upper sensors, or by averaging the current outputs from the lower sensors.

$$I_0 = \frac{1}{2} \langle I_1 + I_3 \rangle = \frac{1}{2} \langle I_2 + I_4 \rangle \quad (3-44)$$

The simulation shown in Figure 10 assumes contact force parameter values of $\alpha = 100$ and $\beta = 10$, as well as a zero initial condition of x_0 .

$$x_0 = \begin{bmatrix} 0 \\ 0 \\ 0 \\ 0 \\ 0 \\ 0 \end{bmatrix} \quad (3-45)$$

The plots show that the currents at Sensors 1 and 2 are nearly identical for the provided conditions. Therefore, only the response of Sensor 1 will be visualized for the remainder of the report, as the responses at the other sensors will exhibit similar behaviors.

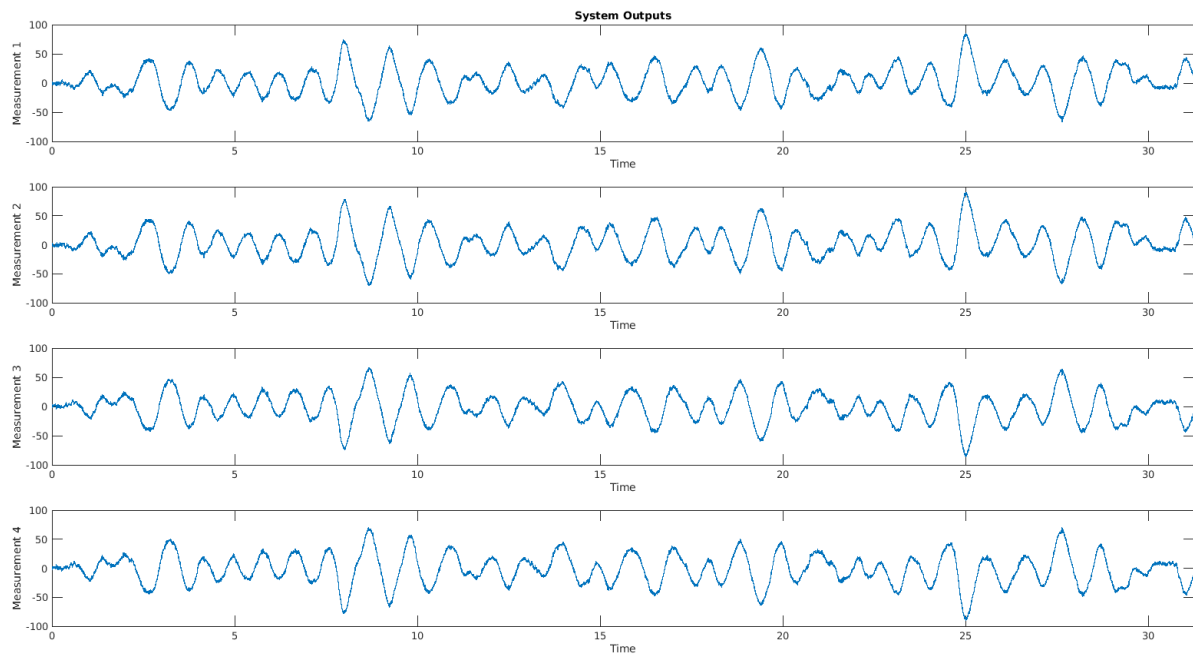


Figure 10: Response of the ex-core neutron noise sensors to the core barrel's vibrations

4.0 Machine Learning

The usefulness of the simulation is checked by attempting to extract the values of the contact force parameters from the synthetic data. The contact parameters are assumed to be the only parameters that change over the course of the system’s degradation. Therefore, if the parameters cannot be extracted from the simulation’s outputs, the simulation won’t be useful for estimating the degradation of the system.

The condition of the core barrel system is assumed to remain constant for the duration of each simulation because degradation occurs on a much longer timescale than the simulation. For example, assume a new reactor with a life cycle of 50 years is installed at a nuclear power plant and ex-core measurements are recorded once a month. If properly installed and maintained, the internals shouldn’t significantly degrade until the reactor draws near the end of its estimated life cycle. Therefore, the dynamics of the reactor shouldn’t significantly change over the course of a single month, barring some sudden change in operating conditions. However, the condition of the reactor might change over the course of several months, and it will definitely change by the end of its life cycle.

4.1 Grid Search Method

The characteristics of the non-linear contact force are an indication of radial-key health. The contact parameters are assumed to be the only variables that change over the course of the system’s degradation. Degradation occurs over a long time-scale, on the order of many months or years. Data is collected over far shorter time-scales, such as hours or minutes, during which the contact force parameters are considered constant. Each contact parameter is assumed to have a vector of discrete values over some range. The two vectors form a grid containing every possible combination of contact parameters. The system’s response is simulated over a predetermined time interval for every contact parameter combination in this grid, and the responses are collected into a synthetic dataset.

An additional response is generated by the continuous-time simulation for a known combination of machine learning parameters and a random seed for random number generation. This represents the true measured response of the system. However, the machine learning parameter values for the measured output of the actual system will be unknown. In such a case, the parameters must be approximated from the measured time-domain response of the system. This can be achieved through a grid search method, where the simulated responses from the synthetic dataset are compared to the measured values. Ideally, the grid search method should locate the combination of contact parameters whose average response best approximates the behavior of the measured data.

A 9-by-9 grid of parameter combinations is considered for testing the grid search algorithm. This grid includes 9 values uniformly-spaced on a base-10 logarithmic scale for each parameter. The resulting grid of 81 unique parameter combinations is then reduced according to the constraints imposed by the core barrel system. As previously mentioned in the “Data Generation” chapter, the grid’s parameter values are selected such that α is within the range of 10 N to 100 000 N, β falls in the range of 0.1 s/m to 1000 s/m, and $\gamma = \alpha\beta$ is within a range of 100 N s/m to 10 000 N s/m. The grid of 81 logarithmically-scaled parameter combinations is reduced to a grid of 34 parameter combinations by limiting the combinations according to these ranges.

4.2 Ensemble Average

The turbulent force input introduces randomness to every simulation of the system. Even if a measured signal has the same contact parameters as one of the simulations in the grid, the randomness of the input force will cause the signal to deviate from the simulation. Therefore, the measurement signal’s contact parameters cannot be found using a single grid of simulations. Instead, the signal is compared to an ensemble of simulations for each contact parameter combination in the grid.

Each ensemble is composed of multiple replications of a simulation for a given set of contact parameters. Each replication within the ensemble has a different seed for random

number generation, producing a different random input force and a different response. The average response of the ensemble's replications represents the average response of the simulation to the random input. All simulation replications for every parameter combination are stored in a single synthetic dataset. The ensemble average and standard deviation are computed for each parameter combination. The reactor's actual ex-core measurements are compared to these ensemble averages to determine the parameter combination that best describes the reactor's operating conditions.

The simulations of the core barrel assume its motion begins at some state defined by the initial condition. This assumption sets the initial variance amongst replications to zero, and the randomness introduced by the turbulent force causes the variation to increase. As a result, the initial response of the core barrel is highly transient, and the average time-domain response varies significantly over time. The transient response of the core barrel is non-stationary, complicating the analysis process.

Once the system's transient response decays, the average response among replications remains nearly constant. This indicates that the core barrel system's non-transient response to turbulence is a stationary random process, and that the ensemble average is equivalent to the time-averaged mean of the response.

The turbulent force exciting the core barrel is assumed to be a band-limited white noise signal, which is stationary. Realistically, the turbulent force can only be stationary if the operating conditions of the reactor and the coolant system remain near-constant during the measurement period. Under such an assumption, the ex-core sensor measurement taken during the associated time period should be a stationary record. These conditions are generally true under the reactor's normal operating conditions.

The reactor's ex-core radiation flux measurements are recorded once a month over the course of an 18 month operation cycle. Until the outage at the end of the cycle, the reactor continuously operates at full power, with only slight random variations in the operating conditions. Assuming the transients of the reactor structure settle within a month, each ex-core measurement should reflect the reactor's steady-state response. Therefore, the transient response of each core barrel simulation is ignored, and only the steady-state responses are stored within the synthetic dataset.

4.3 Performance Metrics

In this paper, the grid search method’s performance is defined as its ability to correctly identify the contact parameters associated with a synthetic dataset. This dataset is generated by simulating the model’s output for a specific combination of contact parameters. The grid search method is said to perform well if it selects a set of contact parameters that generate behavior similar to the true contact parameters.

The performance of an individual ensemble is evaluated by examining how closely it matches the measured behavior. There are numerous ways to compare the ensemble and the measured signal. This report uses three different performance metrics for comparing how well each ensemble matches the measured data. Each performance metric compares the signals through a different method. As such, the best-performing ensemble according to one metric may not perform well according to another metric. However, the ensemble that best matches the measured signal should perform relatively well on each metric.

4.3.1 Minimum Error

The first attempted approach locates the combination of contact parameters that produced the minimum root mean squared error compared to the true measurement. The overall error of a simulation is represented by the root mean squared error,

$$\text{RMSE} = \sqrt{\frac{1}{N} \sum_{i=1}^N (\bar{x}_{\text{sim},i} - x_{\text{true},i})^2} \quad (4-1)$$

where N is the number of time-series measurements for the simulation, $\bar{x}_{\text{sim},i}$ is the average simulated response at the i th time point, and $x_{\text{true},i}$ is the measured response at the i th time point.

The grid search method finds the measurement signal’s associated parameter combination by comparing the measurement signal to the ensemble-averaged synthetic data for every combination of contact parameters. It computes the RMSE between the measurement and each ensemble average, compares the RMSE values found for each parameter combination,

and returns the parameter combination with the lowest RMSE. This parameter combination should theoretically describe the contact mechanics of the measured reactor.

However, the RMSE calculation does not account for variations within the ensemble. If the standard deviation of the replications at a time point is high, any single replication at that time is likely to deviate from the average. A response that falls within two standard deviations of the average is said to be within the distribution's 95% confidence interval. If the measured response is within a parameter combination's confidence interval at all points in time, the behavior of the true signal matches the general behavior associated with that combination of contact parameters. A parameter combination may have a high RMSE value even if the measured signal falls within the confidence interval at all points in time, provided the standard deviation amongst replications is high.

One method to compensate for the variance involves normalizing the error at each time point by the standard deviation amongst the replications. This penalizes parameter combinations with low variance more heavily than combinations with high variance. The penalization is necessary because the grid search method is meant to locate the parameter combination where the true measurement signal falls within the confidence interval of the average response. If the true signal does not fall within the confidence interval at a specific time point, the normalized error should increase substantially. The normalized error is expressed as

$$\text{Error}_{\text{norm}} = \left| \frac{x - \mu}{\sigma} \right| \quad (4-2)$$

where μ is the average value of the distribution and σ is the standard deviation. Substituting the normalized error into the equation for the root mean squared error yields

$$\text{RMSE}_{\text{norm}} = \sqrt{\frac{1}{N} \sum_{i=1}^N \left(\frac{\bar{x}_{\text{sim},i} - x_{\text{true},i}}{\sigma_{\text{sim},i}} \right)^2} \quad (4-3)$$

where $\sigma_{\text{sim},i}$ is the standard deviation of the replications at the i th point in time.

The normalized error applies a greater penalty to a parameter combination when the true signal falls outside of the response's confidence interval at a given time point. If the replications all exhibit similar responses at a given time point, the confidence interval will be small at this time. If there are large variations between the replications at another time

point, the confidence interval will be large at that time. Consider a true signal that deviates from the average response at both of these time points by the same amount. The error at each time point is the same, penalizing the parameter combination by the same amount at both time points. However, the deviation from the average response may fall within the wider confidence interval and outside of the more narrow confidence interval. In this case, the behavior of the true signal matches the behavior of the replications within the wide confidence interval, and the true signal's behavior massively deviates from the replications at the more narrow confidence interval. Therefore, the deviation should be more heavily penalized at the narrow confidence interval than at the wide confidence interval. Normalizing the error by the standard deviation accounts for such differences in the confidence interval, making the normalized error a better measure for the true signal's deviation from the average response amongst replications.

This newly-introduced bias towards parameter combinations with larger standard deviations may over-correct the grid search. The algorithm may begin to identify parameter combinations associated with larger standard deviations as better approximations of the measured data than combinations whose average values closely match the true measurements. In a worst-case scenario, the grid search might always select the parameter combination with the largest standard deviation as the true parameter value regardless of the measured signal's behavior. The RMSE must be weighted such that both the ensemble average and the standard deviation amongst replications are considered when performing the grid search.

4.3.2 Maximum Likelihood

Likelihood functions are another way to select the ensemble average associated with a measured signal. Likelihood expresses the probability that a sample originates from a given probability distribution function. In this case, the distribution under analysis is the ensemble of simulations, and the sample in question is the ex-core measurement. A high likelihood indicates a strong possibility that the measured signal originated from the ensemble. Therefore, the likelihood should be maximized for the ensemble associated with the measured signal's unknown contact parameters. To account for time-dependent variations

in the ensemble and the response, the likelihood is computed at every point in time for the simulation.

The likelihood that the true response is generated from the ensemble of replications is computed at each time point for a given parameter combination. This is achieved by approximating the ensemble’s probability distribution at the provided time point as a Gaussian distribution with the ensemble’s average and standard deviation at that time. A logarithm is then applied to the likelihood, and the resulting log-normalized likelihoods at every time point are averaged together over the entire steady-state time span of the response. The logarithms are applied to avoid floating point errors. The process is repeated for every combination of contact parameters in the grid of simulations. The parameter combination with the maximum time-averaged log-normalized likelihood should theoretically be the set of contact parameters most likely to match the true response’s behavior.

4.3.3 Maximum Cross-Correlation

Theoretically, the cross-correlation between the true measurement and the ensemble average associated with a parameter combination should be maximized for the true combination of contact parameters. The cross-correlation time-shifts one signal with respect to the other, maintaining the time order of each signal’s points. This accounts for the time dependence of both the true measurement and the ensemble average, which is otherwise ignored by the maximum likelihood method.

One cross-correlation method requires convolving each of the ensemble’s replications with the measured signal for a single parameter combination. The convolution is averaged over the measurement’s time period, creating a performance metric representing the time-averaged cross-correlation between the replication and the measurement. This process is repeated for every replication in the ensemble associated with the previously specified parameter combination. The cross-correlation is averaged over the entire ensemble of replications, creating a single performance metric representing the agreement between the parameter combination’s ensemble of replications and the measured signal. This is repeated for every parameter combination in the grid before comparing the performance metrics. The measured signal’s

cross-correlation with the ensemble average should be relatively high for the parameter combination used during data generation.

Another cross-correlation method requires computing the ensemble average of the replications for a single parameter combination first, then convolving the ensemble average with the true signal. The convolution is then averaged over time to produce the average cross-correlation associated with that parameter combination. This process is repeated for every parameter combination, and the one with the highest average cross-correlation is identified as the parameter combination that best approximates the measured signal.

Both methods produced identical performance metric values when tested on a given parameter combination, so neither cross-correlation method is more or less accurate than the other. The second cross-correlation method is far faster and consumes less system memory than the first. Therefore, the second cross-correlation method is recommended for locating the contact parameters.

5.0 Kalman Filter

Kalman filters excel at estimating the state of a system from its noisy measurements. A Kalman filter is a type of optimal state estimator that compares a measured output to a model's prediction at a given point in time. The difference between the system's predicted output and the observation is used to update the system's state estimate, improving the accuracy of the estimation process. The difference between the measured output and the model's prediction is known as the 'residual' or 'measurement innovation' of the Kalman filter, and this feedback term is weighted by the optimal Kalman gain K .

An a priori state estimate \hat{x}^- considers evidence from all time points prior to the one being evaluated. This estimate is used to predict the output \hat{y}^- at the current time point. The predictor equation expresses the a priori state estimate and the predicted output at time t_k as follows:

$$\hat{x}_k^- = F\hat{x}_{k-1}^+ \quad (5-1)$$

$$\hat{y}_k^- = C\hat{x}_k^- \quad (5-2)$$

where \hat{x}_{k-1}^+ is the a posteriori state estimate at the previous time point t_{k-1} . The a posteriori state estimate \hat{x}^+ modifies the a priori estimate using an observation y made during the associated time step. This computation is expressed in the corrector equation:

$$\hat{x}_k^+ = \hat{x}_k^- + K(y_k - \hat{y}_k^-) = \hat{x}_k^- + K(y_k - C\hat{x}_k^-) \quad (5-3)$$

The predictor and corrector equations are combined to form the following expressions:

$$\hat{x}_k^+ = \hat{x}_k^- + K(y_k - C\hat{x}_k^-) \quad (5-4)$$

$$\hat{x}_{k+1}^- = F\hat{x}_k^+ = F\hat{x}_k^- + FK(y_k - C\hat{x}_k^-) \quad (5-5)$$

The Leuenberger observer gain $L = FK$ is substituted into the above expression to yield the discrete-time state-space model for a Kalman-filtered system.

$$\begin{aligned} \hat{x}_{k+1}^- &= F\hat{x}_k^- + L(y_k - C\hat{x}_k^-) \\ \hat{y}_k^- &= C\hat{x}_k^- \end{aligned} \quad (5-6)$$

By grouping together the \hat{x}_k^- terms on the right-hand side of the above equation, the effective dynamics matrix of the Kalman-filtered system is revealed to be $F - LC$.

$$\hat{x}_{k+1}^- = (F - LC) \hat{x}_k^- + Ly_k \quad (5-7)$$

There are also prediction and correction equations for the variances of the state estimates. The variance of the predicted state \hat{x}_k^- is expressed as Σ_{xx}^- or Σ_k^- , while the variance of the predicted output \hat{y}_k^- is written as Σ_{yy}^- . Similarly, the covariance of \hat{x}_k^- with respect to \hat{y}_k^- is Σ_{xy}^- , and the covariance of \hat{y}_k^- with respect to \hat{x}_k^- is Σ_{yx}^- . Despite the lack of a subscript k , the variance and covariance matrices of the state and output vectors are all dependent on the time step t_k .

The covariance matrix of some vector of random variables x_1 with respect to another vector of random variables x_2 is expressed as the expected value of the first signal's deviation from its mean multiplied by the transpose of the second signal's deviation from its mean. The variance and covariance matrices for the Kalman filter's input and output vectors are expressed as expected values

$$\Sigma_{xx}^- = \mathbb{E} \{ (x - m_x) (x - m_x)' \} \quad (5-8)$$

$$\Sigma_{xy}^- = \mathbb{E} \{ (x - m_x) (y - m_y)' \} \quad (5-9)$$

$$\Sigma_{yx}^- = \mathbb{E} \{ (y - m_y) (x - m_x)' \} \quad (5-10)$$

$$\Sigma_{yy}^- = \mathbb{E} \{ (y - m_y) (y - m_y)' \} \quad (5-11)$$

where m_x is the mean of the input vector x and m_y is the mean of the output vector y . The expected values are simplified, yielding the following expressions:

$$\Sigma_{xx}^- = \Sigma_k^- \quad (5-12)$$

$$\Sigma_{xy}^- = \Sigma_k^- C' \quad (5-13)$$

$$\Sigma_{yx}^- = (\Sigma_{xy}^-)' = C \Sigma_k^- \quad (5-14)$$

$$\Sigma_{yy}^- = C \Sigma_k^- C' + R \quad (5-15)$$

The covariance of \hat{y}_k^- with respect to \hat{x}_k^- is the transpose of the covariance of \hat{x}_k^- with respect to \hat{y}_k^- . In this computation, the predicted state's variance matrix $\Sigma_{xx}^- = \Sigma_k^-$ is assumed to

be symmetric such that $\Sigma_k^{-'} = \Sigma_k^-$. The predictor and corrector equations associated with the state estimate error covariance matrix Σ_k are as follows:

$$\Sigma_k^- = A\Sigma_{k-1}^+ A' + BQB' \quad (5-16)$$

$$\Sigma_k^+ = \Sigma_k^- - \Sigma_{xy}^- (\Sigma_{yy}^-)^{-1} \Sigma_{yx}^- \quad (5-17)$$

The Kalman gain K_k can be expressed in terms of the variance matrices instead of state-space matrices. This collects some of the factors in the equation for Σ_k^+ , simplifying its expression.

$$K_k = \Sigma_{xy}^- (\Sigma_{yy}^-)^{-1} = \Sigma_k^- C' (C\Sigma_k^- C' + R)^{-1} \quad (5-18)$$

$$\Sigma_k^+ = (I - K_k C) \Sigma_k^- \quad (5-19)$$

The core barrel system has both a process noise signal w acting as a source of excitation and a measurement noise signal v obscuring the observed output. These are both assumed to be independent white noise signals. The process noise is assumed to have a normal probability distribution described by the process noise covariance matrix Q , while the measurement noise is assumed to follow a normal probability distribution associated with some measurement noise covariance matrix R . Under these assumptions, both covariance matrices are diagonal and populated with the variances of their associated signals. The size of the process noise covariance matrix is equal to the number of process noise inputs acting on the system. For the case of a system with three process noise components, the process noise variance matrix takes the form shown below,

$$Q = \begin{bmatrix} \sigma_{w1}^2 & 0 & 0 \\ 0 & \sigma_{w2}^2 & 0 \\ 0 & 0 & \sigma_{w3}^2 \end{bmatrix}$$

where σ_{w1}^2 , σ_{w2}^2 , and σ_{w3}^2 are the variances of the three process noise components. Likewise, the measurement noise covariance matrix's dimensions are determined by the number of

measured outputs. For a system with four measured outputs, the measurement noise variance matrix is

$$R = \begin{bmatrix} \sigma_{v1}^2 & 0 & 0 & 0 \\ 0 & \sigma_{v2}^2 & 0 & 0 \\ 0 & 0 & \sigma_{v3}^2 & 0 \\ 0 & 0 & 0 & \sigma_{v4}^2 \end{bmatrix}$$

where σ_{v1}^2 , σ_{v2}^2 , σ_{v3}^2 , and σ_{v4}^2 are the variances of the measurement noise components associated with the first, second, third, and fourth measured outputs.

The a posteriori state estimate is optimized by selecting the Kalman gain matrix K according to the following expression:

$$K = \Sigma^- C' (C \Sigma^- C' + R)^{-1} \quad (5-20)$$

Where Σ^- is the a priori state error variance matrix. If K satisfies the above expression, the a posteriori state estimate error variance Σ^+ is minimized. The a priori state error variance matrix is computed through the discrete algebraic Ricatti equation (DARE), which stabilizes the feedback gain matrix $F - LC$.

$$\Sigma^- = F \Sigma^- F' - F \Sigma^- C' (C \Sigma^- C' + R)^{-1} C \Sigma^- F' + G Q G' \quad (5-21)$$

5.1 Unscented Kalman Filters

The above formulation of a Kalman filter assumes the system in question is linear. For a more generalized expression, the system's discrete-time state space equations are rewritten as

$$\hat{x}_k^- = a(\hat{x}_{k-1}^+) + b(\hat{x}_{k-1}^+) w_{k-1} \quad (5-22)$$

$$\hat{y}_k^- = c(\hat{x}_k^-) + v_k \quad (5-23)$$

where a , b , and c are functions relating the states, process noise inputs, and outputs at various time points. The dynamics function a and input function b in Equation 5-22 relate

the previous state and previous process noise input to the current state. The measurement function c in Equation 5-23 defines the relationship between the state and the measured output at a given time point.

The formulation of the discrete algebraic Ricatti equation expressed in Equation 5-21 is only valid for a linear system. If the system is nonlinear, it can only be solved using a nonlinear method. The state space equations for a nonlinear system follow the generalized format shown in Equations 5-22 and 5-23.

An unscented Kalman filter (UKF) estimates the distribution of the output y_a by propagating the distribution of the input x_a through the nonlinear function f .

$$x_a = \begin{bmatrix} \hat{x}_{k-1}^+ \\ w_{k-1} \\ v_k \end{bmatrix}, \quad y_a = \begin{bmatrix} \hat{x}_k^- \\ \hat{y}_k^- \end{bmatrix} \quad (5-24)$$

$$y_a = f(x_a) = \begin{bmatrix} a(\hat{x}_{k-1}^+) + b(\hat{x}_{k-1}^+) w_{k-1} \\ c(a(\hat{x}_{k-1}^+) + b(\hat{x}_{k-1}^+) w_{k-1}) + v_k \end{bmatrix} \quad (5-25)$$

In the case of the core barrel simulation, the nonlinear function is approximated by applying a fourth-order Runge-Kutta solver to the system's continuous-time state-space model.

A minimal set of sample points are selected from the input's distribution such that their sample mean \bar{x}_a and sample variance P_{xx} match the distribution. The points are symmetrically distributed about the set's mean value, often including a single point located at the mean. This set is known as the distribution's sigma points x_Σ , and they fully recreate the statistics of the Gaussian input.

$$x_a \sim \mathcal{N}(\bar{x}_a, P_{xx}) \quad (5-26)$$

$$x_\Sigma \sim \mathcal{N}(\bar{x}_a, P_{xx}) \quad (5-27)$$

$$\bar{x}_a = \begin{bmatrix} \hat{x}_{k-1}^+ \\ 0 \\ 0 \end{bmatrix} \quad (5-28)$$

$$P_{xx} = \begin{bmatrix} \Sigma_{k-1}^+ & 0 & 0 \\ 0 & Q & 0 \\ 0 & 0 & R \end{bmatrix} \quad (5-29)$$

The sigma points are transformed through the nonlinear function, creating a new distribution of points y_Σ . The mean and variance of the transformed sigma points are then used to create a new Gaussian probability distribution for the outputs. The actual outputs y_a may not strictly follow a Gaussian distribution, but if the transformed sigma points are assumed to follow a Gaussian distribution, then the statistics of the transformed sigma points should approximate the mean \bar{y}_a and variance P_{yy} of the nonlinear function's distribution of outputs for the provided inputs.

$$y_\Sigma = f(x_\Sigma) \quad (5-30)$$

$$y_\Sigma \sim \mathcal{N}(\bar{y}_a, P_{yy}) \quad (5-31)$$

$$y_a \sim \mathcal{N}(\bar{y}_a, P_{yy}) \quad (5-32)$$

$$\bar{y}_a = \begin{bmatrix} \hat{x}_k^- \\ \hat{y}_k^- \end{bmatrix} \quad (5-33)$$

$$P_{yy} = \begin{bmatrix} \Sigma_k^- & \Sigma_{xy}^- \\ \Sigma_{yx}^- & \Sigma_{yy}^- \end{bmatrix} \quad (5-34)$$

The predicted state \hat{x}_k^- and output \hat{y}_k^- at the next time step are extracted from the average values of the transformed sigma points. Similarly, the variances and covariances of the predicted state and output are located within the transformed distribution's variance matrix P_{yy} .

As previously established, Σ_k^- is the variance of the predicted state estimate \hat{x}_k^- at the next time step. Similarly, Σ_{yy}^- is the variance of the next time step's predicted output \hat{y}_k^- . Σ_{xy}^- is the covariance of \hat{x}_k^- with respect to \hat{y}_k^- , and Σ_{yx}^- is the covariance of \hat{y}_k^- with respect to \hat{x}_k^- . As a result, Σ_{yx}^- is the transpose of Σ_{xy}^- . The corrector equation updates the predictions found in \bar{y}_a using the variance matrices extracted from P_{yy} .

$$K_k = \Sigma_{xy}^- (\Sigma_{yy}^-)^{-1} \quad (5-35)$$

$$\hat{x}_k^+ = \hat{x}_k^- + K_k (y_k - \hat{y}_k^-) \quad (5-36)$$

$$\Sigma_k^+ = \Sigma_k^- - \Sigma_{xy}^- (\Sigma_{yy}^-)^{-1} \Sigma_{yx}^- = \Sigma_k^- - K_k \Sigma_{yx}^- \quad (5-37)$$

5.2 Disturbed Parameter Estimation

A Kalman filter can estimate the value of a model parameter if that parameter is assumed to slightly fluctuate about its true value. If a model parameter α fluctuates over time due to a noise term ϵ with a variance of Q_ϵ , the parameter's value at the next time point α_k is approximated by Equation 5-38, while the process noise term is defined in Equation 5-39.

$$\alpha_k = \alpha_{k-1} + \epsilon_{1,k-1} \geq 0 \quad (5-38)$$

$$\epsilon_1 \sim \mathcal{N}(0, Q_{\epsilon,1}) \quad (5-39)$$

The true value of α is assumed to either be positive or zero. Therefore, Equation 5-38 takes the absolute value of α_k to prevent the estimate of α from decreasing below zero.

The true value of a fluctuating parameter in a Kalman filter is estimated by treating the parameter as an additional state and the fluctuation as a process noise input.

$$\mathbf{x} = \begin{bmatrix} x \\ \dot{x} \\ \alpha \end{bmatrix}, \quad w = \begin{bmatrix} u_1 \\ \epsilon \end{bmatrix} \quad (5-40)$$

The terms x and u_1 in the above equations are the core barrel position and turbulent force vectors before introducing the disturbance ϵ_1 to the model parameter α . In the case of the core barrel model, these vectors have the following components:

$$x = \begin{bmatrix} y \\ z \\ \theta \end{bmatrix}, \quad u_1 = \begin{bmatrix} F_y \\ F_z \\ M_x \end{bmatrix} \quad (5-41)$$

A second contact force parameter β in the core barrel model is also disturbed by a noise signal ϵ_2 with a variance of $Q_{\epsilon,2}$. The equation shown below for the next value of β is similar to the equation for the next value of α .

$$\beta_k = \beta_{k-1} + \epsilon_{2,k-1} \geq 0 \quad (5-42)$$

$$\epsilon_2 \sim \mathcal{N}(0, Q_{\epsilon,2}) \quad (5-43)$$

The state and process noise vectors for the core barrel system's Kalman filter are expressed as follows:

$$\mathbf{x} = \begin{bmatrix} x \\ \dot{x} \\ \alpha \\ \beta \end{bmatrix}, \quad w = \begin{bmatrix} u_1 \\ \epsilon_1 \\ \epsilon_2 \end{bmatrix} \quad (5-44)$$

Assuming the disturbance terms ϵ_1 and ϵ_2 are both white noise signals, the variance Q of the new process noise vector is written as

$$Q = \begin{bmatrix} Q_f & 0 & 0 \\ 0 & Q_{\epsilon,1} & 0 \\ 0 & 0 & Q_{\epsilon,2} \end{bmatrix} \quad (5-45)$$

where Q_f is the variance of the original process noise vector u_1 . The process noise vector is represented as the distribution

$$w \sim \mathcal{N}(0, Q) \quad (5-46)$$

For the core barrel disturbance problem's state vector, the augmented input and output vectors are rewritten according to Equations 5-47 and 5-48.

$$x_{a,k} = \begin{bmatrix} \hat{\mathbf{x}}_{k-1}^+ \\ w_{k-1} \\ v_k \end{bmatrix} = \begin{bmatrix} \hat{x}_{k-1}^+ \\ \alpha_{k-1}^+ \\ \beta_{k-1}^+ \\ u_{1,k-1} \\ \epsilon_{1,k-1} \\ \epsilon_{2,k-1} \\ v_k \end{bmatrix} \quad (5-47)$$

$$y_{a,k} = \begin{bmatrix} \hat{x}_k^- \\ \alpha_k^- \\ \beta_k^- \\ \hat{y}_k^- \end{bmatrix} = f(x_{a,k}) = \begin{bmatrix} a(\hat{x}_{k-1}^+) + b(\hat{x}_{k-1}^+)u_{1,k-1} \\ \alpha_{k-1}^+ + \epsilon_{1,k-1} \\ \beta_{k-1}^+ + \epsilon_{2,k-1} \\ c(\hat{x}_k^-) + v_k \end{bmatrix} \quad (5-48)$$

The solutions to these systems of equations are approximated using a fourth-order Runge-Kutta integration method.

A synthetic dataset describing the core barrel's motion is generated for a known combination of true contact parameters. This data is used as the Kalman filter's measurement dataset. Within the Kalman filter, the states associated with the contact parameters are assumed to undergo their associated disturbances. In theory, the Kalman filter should gradually adjust the values of these states over time until they match the contact parameters of the measurement dataset. But in practice, the Kalman filter could adjust the values of the contact parameter states until they produce an output roughly equivalent to that of the measured dataset. If multiple combinations of contact parameters produce similar results, the Kalman filter may trend towards whichever parameter combination is closest to the provided initial condition.

5.3 Effects of Changing Model Parameters

The Kalman filter applied in the parameter disturbance problem should approximate the contact parameters associated with the measured data. Therefore, applying the Kalman filter to a synthetic dataset generated using a different combination of contact parameters should result in different contact parameter estimates. The parameter estimates begin at an assumed initial condition before approaching the values associated with the measured data. The proximity of the initial conditions relative to the dataset's true contact parameters determines how quickly the estimates converge upon their final values. The estimates for an initial guess of α and β near the true parameters should reach a solution more quickly than estimates for an initial condition much further from the true values.

Several simulations are conducted to test these hypotheses. In one set of simulations, the initial conditions are altered for a given synthetic dataset with contact parameters of $\alpha = 1$ and $\beta = 1$. In another group of simulations, synthetic data is generated for various combinations of contact parameters. The contact parameters of each dataset are estimated for an initial guess of $\alpha = 0$ and $\beta = 0$.

Table 4: Parameter estimates for various initial guesses α_0 and β_0 of the contact parameters. The unscented Kalman filter is applied to a synthetic dataset generated using $\alpha = 100$ N and $\beta = 10$ s/m.

α_0	β_0	$\hat{\alpha}$	$\hat{\beta}$
0	0	510	74
10	1	510	74
10	10	490	71
10	100	490	71
100	1	490	71
100	10	490	71
100	100	490	71
1000	1	490	71
1000	10	490	71
1000	100	490	71

5.3.1 Changing Initial Conditions

The Kalman filter requires some initial guess for the system’s states prior to state estimation. The value of this initial condition determines the speed at which the parameter estimates approach their steady-state values. If the initial condition significantly deviates from the synthetic dataset’s parameters, though, the Kalman filter may not replicate the dataset’s contact parameters.

To test this hypothesis, a synthetic dataset describing the 2D motion of an arbitrary spring-mass-damper system was generated for an assumed combination of true parameters. The same spring-mass-damper model was used to create an unscented Kalman filter where the contact parameters undergo some disturbance. This model was tested for various initial conditions to determine their impact upon the simulation’s state estimates. The following initial conditions for α and β were tested for a true parameter combination of $\alpha = 100$ and $\beta = 10$:

For every tested combination of parameters, the contact parameter estimates approach and then fluctuate about $\alpha \approx 490$ N and $\beta \approx 71$ s/m. Therefore the contact parameter estimates appear to be independent of the initial conditions, provided that the initial guesses for the contact parameters are reasonably close to the true values. The contact parameter estimates for an overestimated set of initial parameters are shown in Figure 11, while Figure 12 displays the estimates for an underestimated set of initial parameter values.

5.3.2 Changing True Parameters

Synthetic datasets were generated for multiple combinations of contact parameters in an attempt to analyze how the Kalman filter state estimates change with respect to the true parameter values. The tested parameter combinations are listed below:

The steady-state parameter estimates appear to be more dependent upon α than on β . For synthetic datasets generated using lower values of α , such as $\alpha = 0$ and $\alpha = 10$, the steady-state parameter estimates fluctuate around $\hat{\alpha} \approx 490$ and $\hat{\beta} \approx 71$.

Datasets created with $\alpha = 100$ generate parameter estimates that fluctuate about $\hat{\alpha} \approx 520$ and $\hat{\beta} \approx 76$

If α reaches a value of 1000, the estimated contact parameters vary about $\hat{\alpha} \approx 1000$ and $\hat{\beta} \approx 210$. The value of β does not appear to approach a constant value within the simulation's 30s time span, indicating that its transients have not fully decayed..

The steady-state parameter estimates associated with a true parameter value of $\alpha = 0.1$ all tend to fluctuate about $\alpha \approx 1.0$ Newtons and $\beta \approx 1.2$ seconds per meter, despite having different true values for β . The estimate associated with the parameter combination of $\alpha = 0$ and $\beta = 0$ also exhibits this behavior, as well as the estimates for the parameter combination of $\alpha = 1$ and $\beta = 0.1$.

Some tested parameter combinations, including all combinations with a true value of $\alpha = 10$, deviate from this behavior. The estimates for $\alpha = 10$ and $\beta = 1$ oscillate about $\alpha \approx 3.9$ and $\beta \approx 3.6$. The parameter combination of $\alpha = 10$ and $\beta = 10$ yields estimates oscillating about $\alpha \approx 5.3$ and $\beta \approx 4.5$ instead. The estimates for the following parameter combinations fluctuate about steady-state values of $\alpha \approx 1.4$ and $\beta \approx 1.7$:

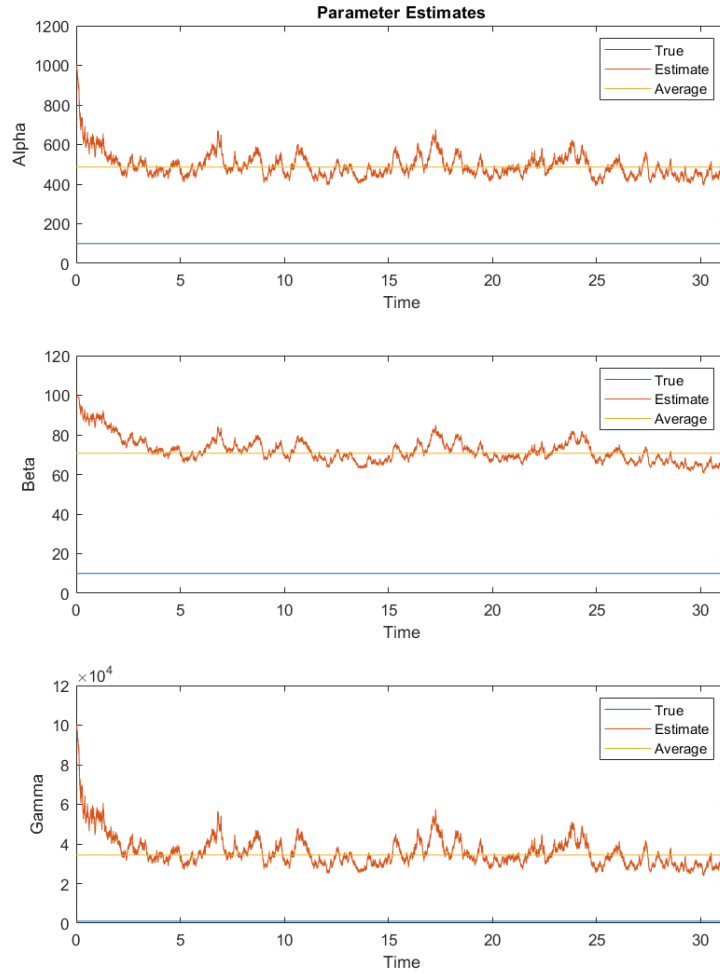


Figure 11: Contact parameter estimates for $\alpha = 100$ and $\beta = 10$, where the initial conditions for the parameters are a factor of 10 above their true values

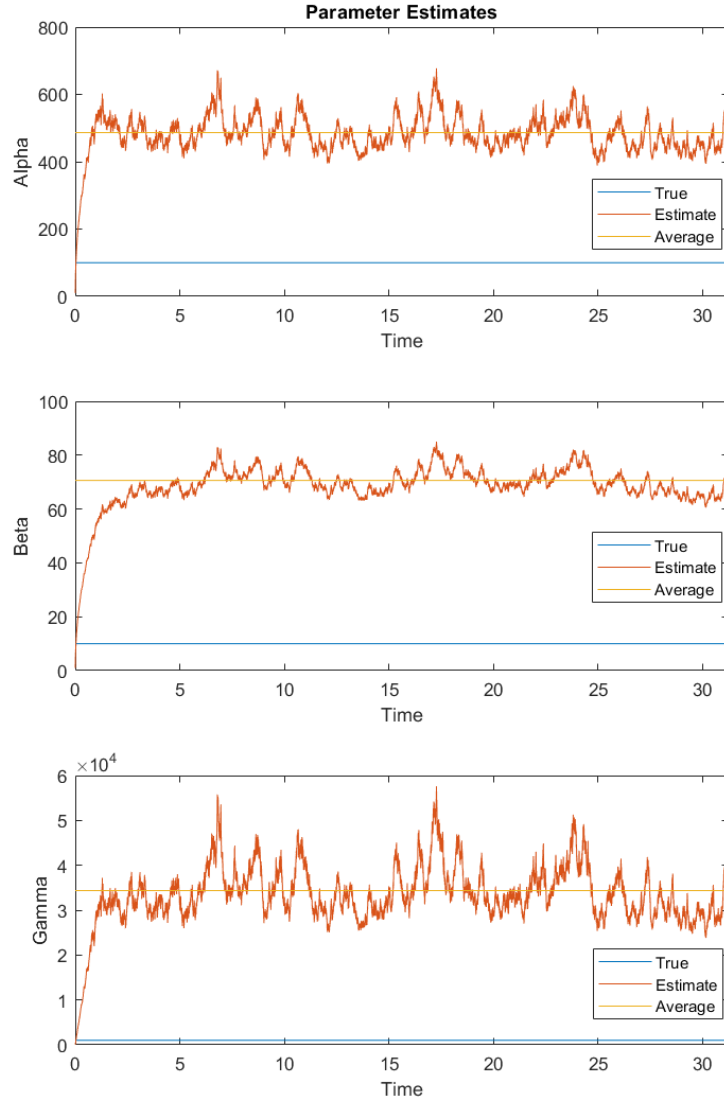


Figure 12: Contact parameter estimates for $\alpha = 100$ and $\beta = 10$, where the initial conditions for the parameters are a factor of 10 below their true values

Table 5: Parameter estimates created by applying the unscented Kalman filter to various synthetic datasets. These datasets are identified by their unique combinations of contact force parameters. The estimates all assume an initial parameter guess of $\alpha_0 = 0$ and $\beta_0 = 0$, with a disturbance of $\sigma_{\epsilon 1} = 10$ for α and $\sigma_{\epsilon 2} = 1$ for β . These simulations are all performed for a random number generation seed of 1, to ensure the variations between datasets are due to their contact parameters and not due to random chance.

α	β	$\hat{\alpha}$	$\hat{\beta}$	σ_{α}	σ_{β}
0	0	490	71	47	4.8
10	10	490	71	47	4.8
10	100	490	71	47	4.8
10	1000	490	71	47	4.8
100	10	510	75	50	5.1
100	100	520	76	52	5.3
100	1000	520	76	53	5.4
1000	10	780	140	99	8.5
1000	100	1000	210	150	35
1000	1000	1000	210	150	37

- $\alpha = 1$ and $\beta = 1$
- $\alpha = 1$ and $\beta = 10$
- $\alpha = 10$ and $\beta = 0.1$

For every tested combination of parameter values, the Kalman filter’s estimates could not replicate both contact force parameters. The estimates associated with the combinations of $\alpha = 1$, $\beta = 0.1$ and $\alpha = 0.1$, $\beta = 1$ each managed to closely approximate one parameter: α for the former, and β for the latter.

5.4 State and Output Estimates

The unscented Kalman filter provides estimates for the core barrel system’s states, outputs, and contact parameters. The outputs are compared to the measurements of the reactor’s ex-core neutron radiation sensors. Unfortunately the internal states and contact parameters for an actual core barrel system cannot be measured, preventing analysis of the Kalman filter’s state and parameter estimates. This issue is remedied through the use of a synthetic dataset for which the state and true parameter values are known. By training the Kalman filter on such a dataset, the filter’s capabilities for approximating the contact force model may be analyzed. For this specific example, a synthetic dataset is generated with true contact force parameters of $\alpha = 100$ N and $\beta = 10.0$ s/m.

The error for the Kalman filter method is quantified as the difference between the synthetic dataset’s response and the Kalman filter’s corrected output. This error is used to compute the root-mean-squared error of the Kalman filter’s approximated response. The output vector \hat{y}_1 is approximated by applying an unscented Kalman filter to the synthetic dataset. The output estimates are plotted in Figure 13, and the errors of these estimates are shown in Figure 14. Each estimated output in the vector \hat{y}_1 has a root-mean-squared error of 0.084 when compared to the synthetic dataset’s recorded true response y_1 , as shown in Table 6.

The estimates of the core barrel system’s position states enjoy similar accuracy, as shown by the position state estimates displayed in Figure 15 alongside the true position states. The

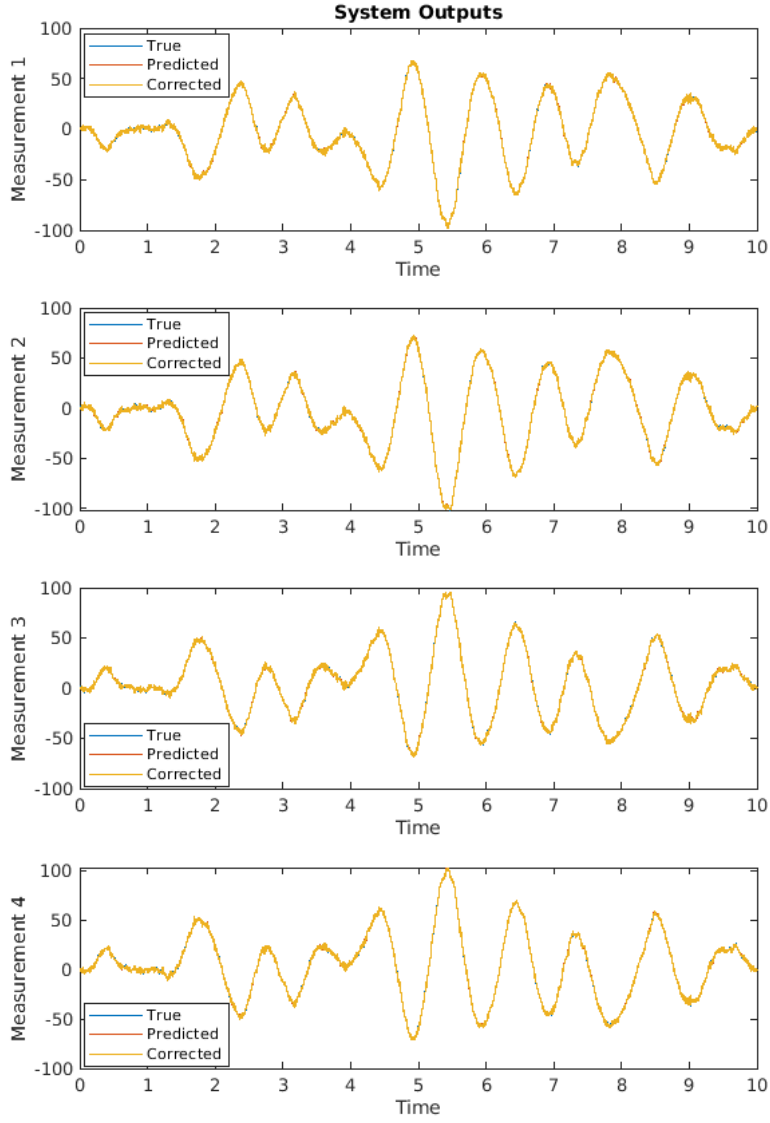


Figure 13: The unscented Kalman filter's estimates for the core barrel system's ex-core neutron noise outputs. The Kalman filter is trained on a synthetic dataset generated using $\alpha = 100$ N and $\beta = 10.0$ s/m.

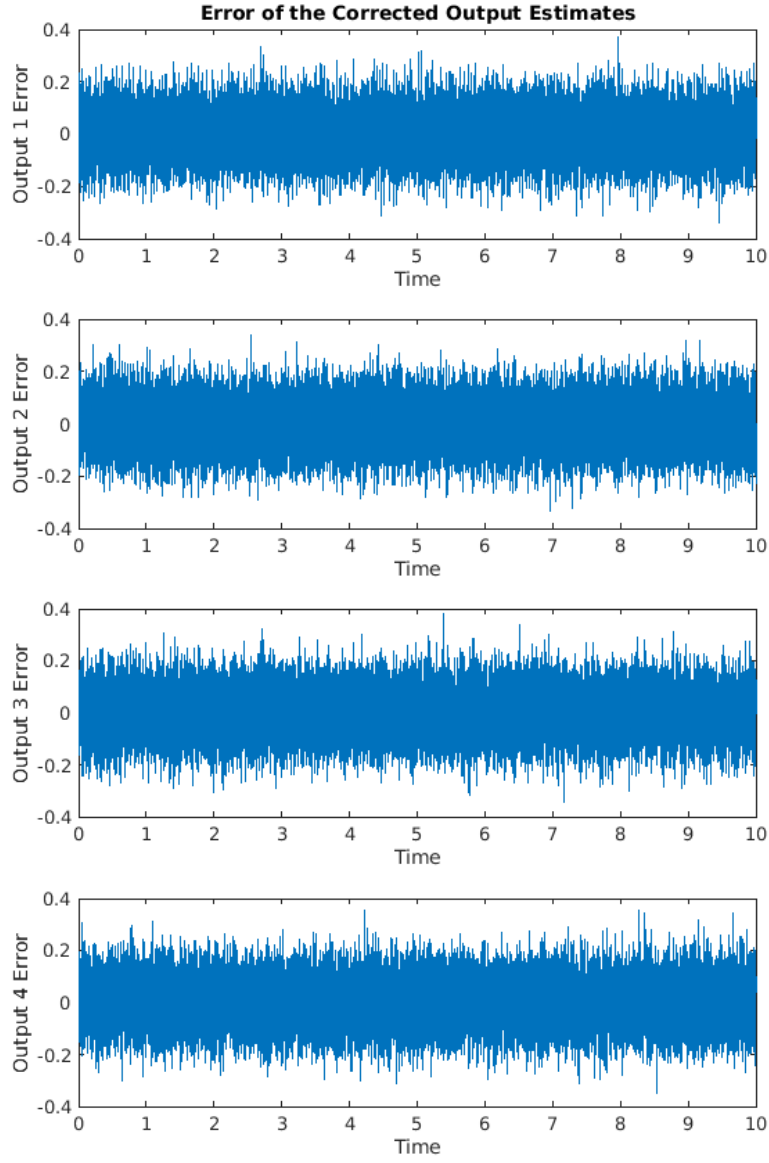


Figure 14: Error of the unscented Kalman filter's output estimates for a synthetic dataset with $\alpha = 100$ N and $\beta = 10.0$ s/m

Table 6: Root-mean-squared error values for each output estimated by the unscented Kalman filter with respect to the training dataset’s true outputs. The synthetic training dataset of this Kalman filter is generated using $\alpha = 100$ N and $\beta = 10.0$ s/m.

Output	RMSE
Output 1	0.084
Output 2	0.084
Output 3	0.084
Output 4	0.084

errors for these estimates are shown in Figure 16. The root-mean-squared errors of the state estimates \hat{y} , \hat{z} , and $\hat{\theta}$ with respect to their true values from the synthetic dataset are approximately $2.50e - 6$, $2.44e - 6$, and $1.34e - 4$ respectively. The error in the estimate for the rotational displacement θ is significantly higher than the estimates for the horizontal displacement y and vertical displacement z . This is likely because the rotational displacement depends on both the horizontal and the vertical components of the contact force estimates. The horizontal displacement y is directly related to the horizontal components of the contact forces, but the vertical components of the forces only contribute to this displacement through its dependencies on the other displacement terms. Similarly, the vertical displacement depends on the vertical contact forces, but its dependence on the horizontal components is limited to the term’s dependence on y and θ . In contrast, the rotational displacement is directly related to the moments applied by all four contact force components. Therefore, any error in the contact force estimates is magnified in the rotational displacement estimate to a greater degree than in the other displacement estimates.

The system’s velocity state estimates and true velocity states are shown in Figure 17, while the errors in the velocity state estimates are located in Figure 18. These state estimates have root-mean-squared error values of 2.94×10^{-6} for \hat{y} , 2.86×10^{-6} for \hat{z} , and 1.24×10^{-3} for $\hat{\theta}$. The velocity states have higher error values than the position state estimates because numerical derivatives are inherently inaccurate. The core barrel system’s approximations for the velocity states depend on numerical derivation through a Taylor series approxima-

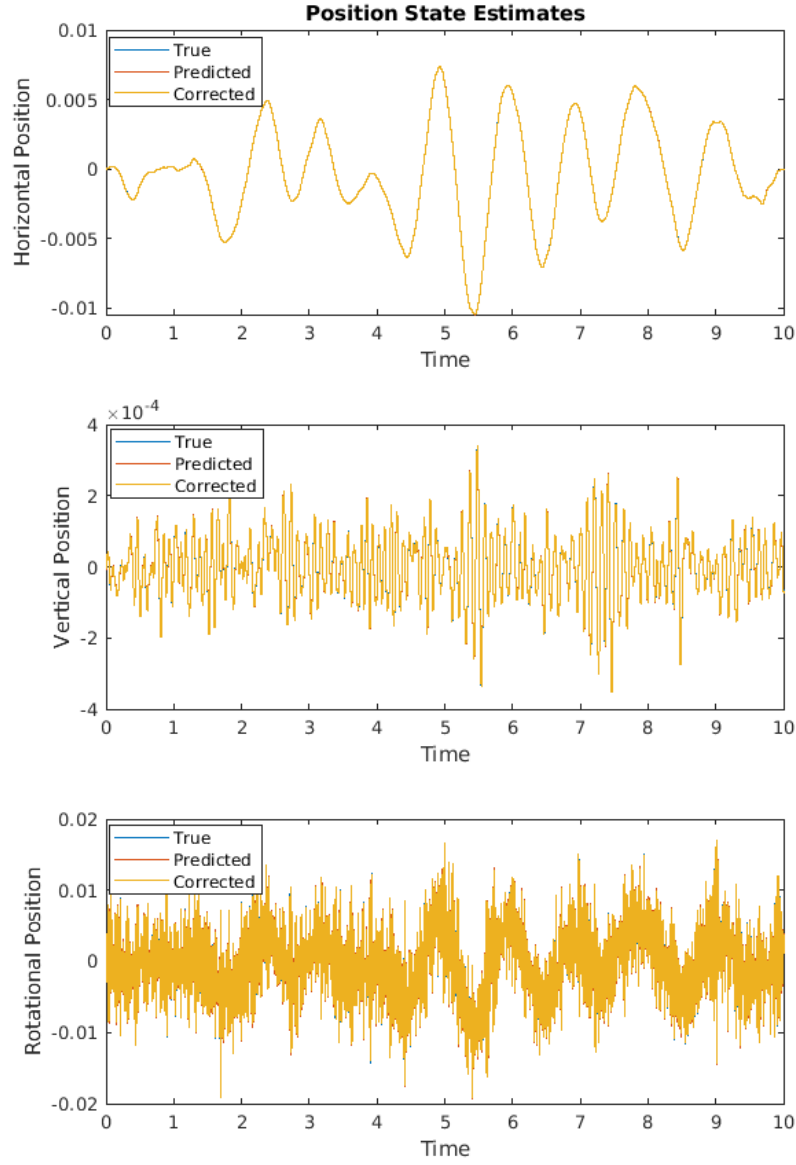


Figure 15: The unscented Kalman filter's estimates for the core barrel system's position states. The Kalman filter is trained on a synthetic dataset generated using $\alpha = 100$ N and $\beta = 10.0$ s/m.

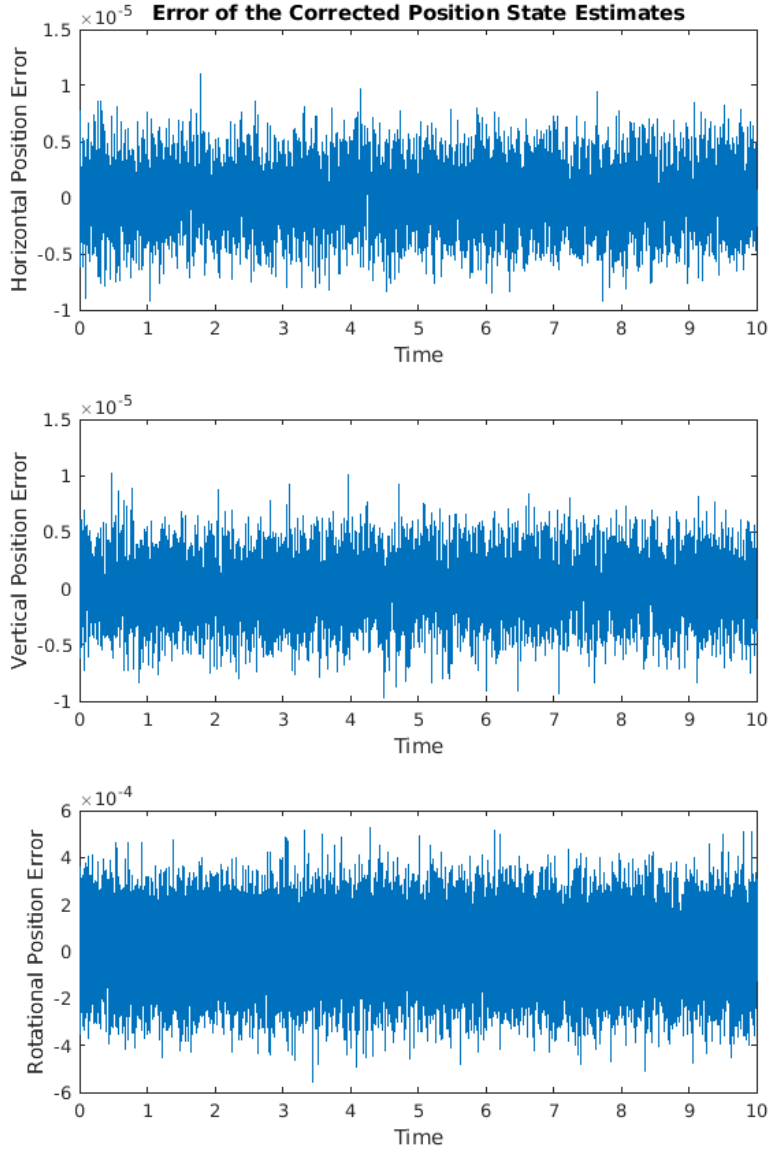


Figure 16: Errors in the unscented Kalman filter's estimates for the core barrel system's position states. The Kalman filter is trained on a synthetic dataset generated using $\alpha = 100$ N and $\beta = 10.0$ s/m.

Table 7: Root-mean-squared error of each state estimated by the unscented Kalman filter with respect to the training dataset’s true states. This Kalman filter is trained on a synthetic dataset generated using $\alpha = 100$ N and $\beta = 10.0$ s/m.

State	RMSE
\hat{y}	2.50×10^{-6}
\hat{z}	2.44×10^{-6}
$\hat{\theta}$	1.34×10^{-4}
$\dot{\hat{y}}$	2.94×10^{-6}
$\dot{\hat{z}}$	2.86×10^{-6}
$\dot{\hat{\theta}}$	1.24×10^{-3}

tion. The Runge-Kutta algorithm assumes a fourth-order approximation of the Taylor series, which neglects Taylor series terms higher than the fourth order. This is a fairly accurate approximation for a numerical derivative, but the missing terms still introduce some error into the process. This global error is proportional to h^4 , where h is the length of the numerical solver’s time step. Provided that h is far below the system’s associated time constant, the error should be relatively small, but it will still accumulate through numerical evaluation of the system’s states at successive time points. Additionally, errors in the position state estimates propagate through these numerical derivatives, generating increased error in the velocity state estimates. This is especially true for the core barrel system’s angular velocity estimate, since the rotational displacement estimate has greater error than the other displacement estimates.

The root-mean-squared errors of the state estimates for this synthetic dataset are summarized in Table 7.

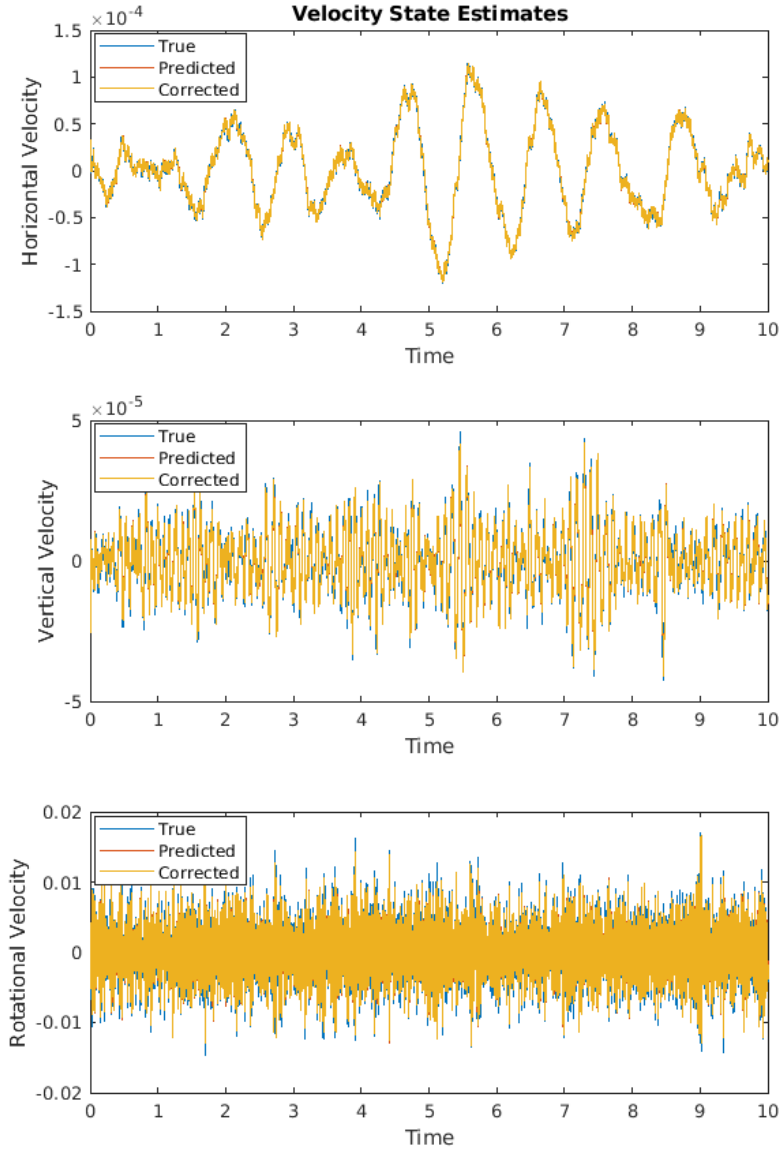


Figure 17: The unscented Kalman filter's estimates for the core barrel system's velocity states. This Kalman filter's training dataset uses a contact parameter combination of $\alpha = 100$ N and $\beta = 10.0$ s/m.

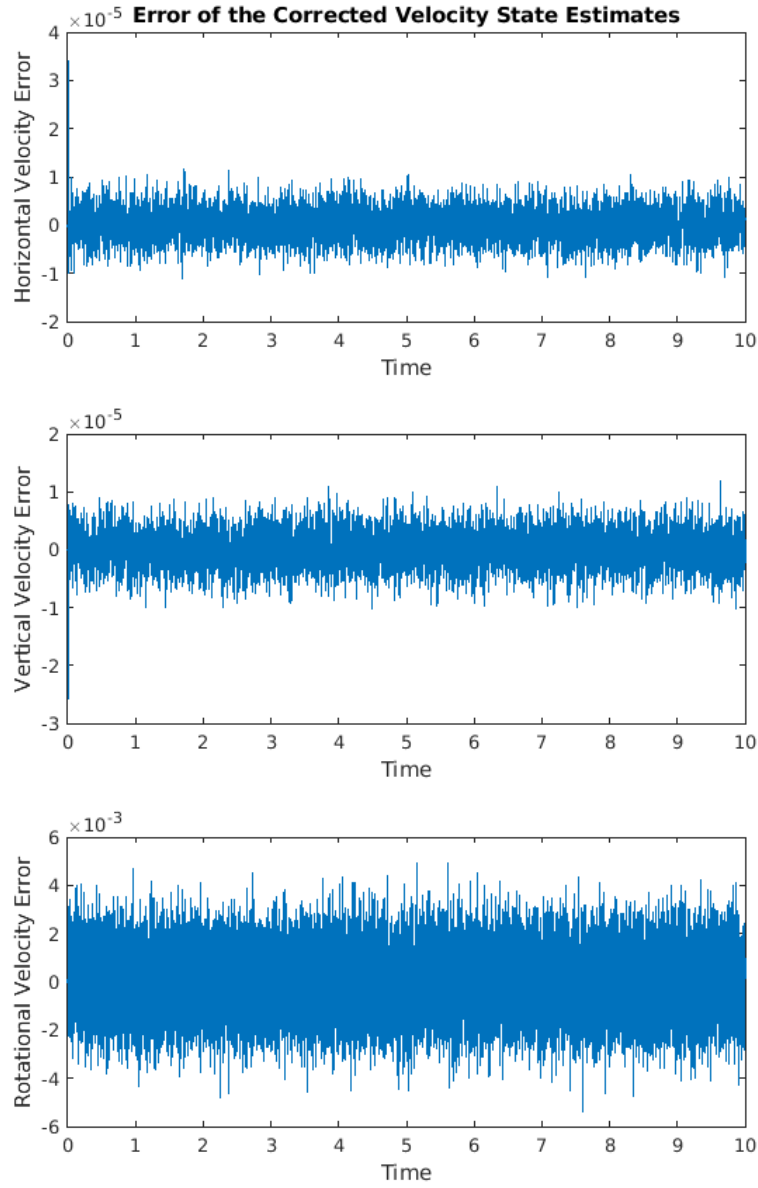


Figure 18: Errors in the unscented Kalman filter’s estimates for the core barrel system’s velocity states. This Kalman filter’s training dataset uses a contact parameter combination of $\alpha = 100$ N and $\beta = 10.0$ s/m.

6.0 Results and Discussion

The two methods for estimating the core barrel system’s contact force parameters are tested on four synthetic datasets, each generated with its own combination of true contact parameters. The performances of these estimation methods are then evaluated based upon the contact parameter estimates for these datasets.

6.1 Overview of Methods

The grid search method and unscented Kalman filter method for contact parameter estimation are outlined below.

6.1.1 Overview of Grid Search

The grid search method attempts to locate a combination of contact parameters on a grid that best approximates the system’s response. This is achieved by generating multiple simulations of the system for every parameter combination on the grid, taking the ensemble average of those simulations, and evaluating the ensemble’s performance with respect to the measured output.

A 9-by-9 grid of parameter combinations is considered for testing the grid search algorithm. This grid includes 9 values uniformly-spaced on a base-10 logarithmic scale for each parameter. The resulting grid of 81 unique parameter combinations is then reduced according to the constraints imposed by the core barrel system. As previously mentioned in the “Data Generation” chapter, the grid’s parameter values are selected such that α is within the range of 10 N to 100 000 N, β falls in the range of 0.1 s/m to 1000 s/m, and $\gamma = \alpha\beta$ is within a range of 100 N s/m to 10 000 N s/m. The grid of 81 logarithmically-scaled parameter combinations is reduced to a grid of 34 parameter combinations by limiting the combinations according to these ranges.

The performance of the grid search algorithm is found by computing all three performance metrics discussed in Chapter 4 for each parameter combination in the grid, evaluated over the entire ensemble of replications. These performance metrics are the root-mean-squared error of the ensemble average with respect to the measured output, the likelihood that the measured output came from the ensemble, and the cross-correlation between the ensemble average and the output. The likelihood and cross-correlation should be maximized for a parameter combination whose ensemble matches the measured output's behavior, while the root-mean-squared error should be minimized. Each simulation of the system's response for a given combination of contact force parameters is performed 20 times with randomized inputs sampled from the same distribution. These simulations form the ensemble of replications for that parameter combination, summarized by a mean and a variance.

The ensemble average for each parameter combination is compared to the measured output of the system by computing the performance metrics. These metrics are then compiled into a dataset representing the performance of every parameter combination on the grid. The average value and standard deviation of each performance metric is computed over the entire grid of combinations. Each performance metric p is then standardized by its mean \bar{p} and normalized by its standard deviation σ_p .

$$p_{\text{normal}} = \frac{p - \bar{p}}{\sigma_p} \quad (6-1)$$

The true combination of contact parameters associated with the measured data is expected to perform well on all three performance metrics. A simulation generated with the true parameters should have a relatively low error with respect to the measured signal. The cross-correlation between the simulation and the measurement should also be relatively high in comparison to other simulations, and the likelihood that the synthetic data originated from the ensemble associated with the true parameter combination should be greater than the likelihoods associated with other parameter combinations. Therefore, all three performance metrics should be considered together when evaluating the overall performance of a parameter combination.

The parameter combinations whose ensembles perform better-than-average on all performance metrics are extracted from the grid. A geometric mean is applied to the parameter

estimates of this subset to approximate the synthetic dataset’s true parameter combination. A geometric average is applied instead of an arithmetic mean because the contact force parameters are spaced on a logarithmic scale.

6.1.2 Overview of Kalman Filtering

The unscented Kalman filter provides estimates for the core barrel system’s states, outputs, and contact parameters. The outputs are compared to the measurements of the reactor’s ex-core neutron radiation sensors. Unfortunately the internal states and contact parameters for an actual core barrel system cannot be measured, preventing analysis of the Kalman filter’s state and parameter estimates. This issue is remedied through the use of a synthetic dataset for which the state and true parameter values are known. By training the Kalman filter on such as dataset, the filter’s capabilities for approximating the contact force model may be analyzed.

Our goal in implementing the unscented Kalman filter is to estimate the contact force model’s parameters. Traditional performance metrics based upon the error between the estimated response and the synthetic data’s response won’t indicate the Kalman filter’s capability in estimating the contact parameters. Instead, the performance metric of interest must account for the difference between the method’s approximations for the contact force parameters and the true parameter values used when generating the synthetic data.

If the Kalman filter method approximates the contact force model, the estimates for α and β should settle such that their time-averaged values are nearly constant. The disturbance terms ϵ_1 and ϵ_2 prevent the approximations of α and β from reaching truly constant values. Once the core barrel system’s transient response decays and the Kalman filter’s parameter estimates leave their initial conditions, each parameter estimate should form a Gaussian distribution about some time-averaged value. The standard deviation of this distribution is determined by the magnitude of the disturbance. Ideally, the average contact parameter estimates should be relatively close to the true values from the synthetic dataset.

The contact parameter estimates must adjust from their assumed initial conditions to the unscented Kalman filter’s estimated values. As a result, the parameter estimates during the system’s transient period are far from the final estimated values.

6.2 Synthetic Dataset 1

A synthetic dataset is generated for a maximum contact force of $\alpha = 100$ N and a β value of 10.0 s/m, which is associated with a characteristic velocity of $v_c = 0.100$ m/s and an effective viscous damping coefficient of $\gamma = 1000$ N s/m for the contact force. The contact force model described by these parameters increases the damping ratio of the core barrel system’s most damped mode from $\zeta = 0.10$ to $\zeta = 0.12$. This 20% increase in the core barrel’s highest-damped mode should generate a detectable change in the system’s outputs. The synthetic dataset’s contact force parameters are approximated using the grid search and Kalman filter methods. The results are analyzed and compared below.

6.2.1 Grid Search Results

Across the grid of parameter combinations, the performance of each combination is evaluated according to each metric with respect to synthetic dataset 1. The performances are displayed in Figures 19 to 21.

The performances of each metric’s optimal parameter combinations, as well as the performance of the dataset’s true combination of parameter values, are shown in Table 8. Only 7 of the grid’s 34 parameter combinations perform above-average on all metrics with respect to the synthetic dataset, as shown in Table 9.

The average value of α for the extracted dataset is 4870 N with a standard deviation of 11800 N, and the average of β is 61.6 s/m with a standard deviation of 118 s/m. The standard deviations for both parameter estimates are larger than the average values, indicating that the estimated contact parameters may not follow a Gaussian distribution.

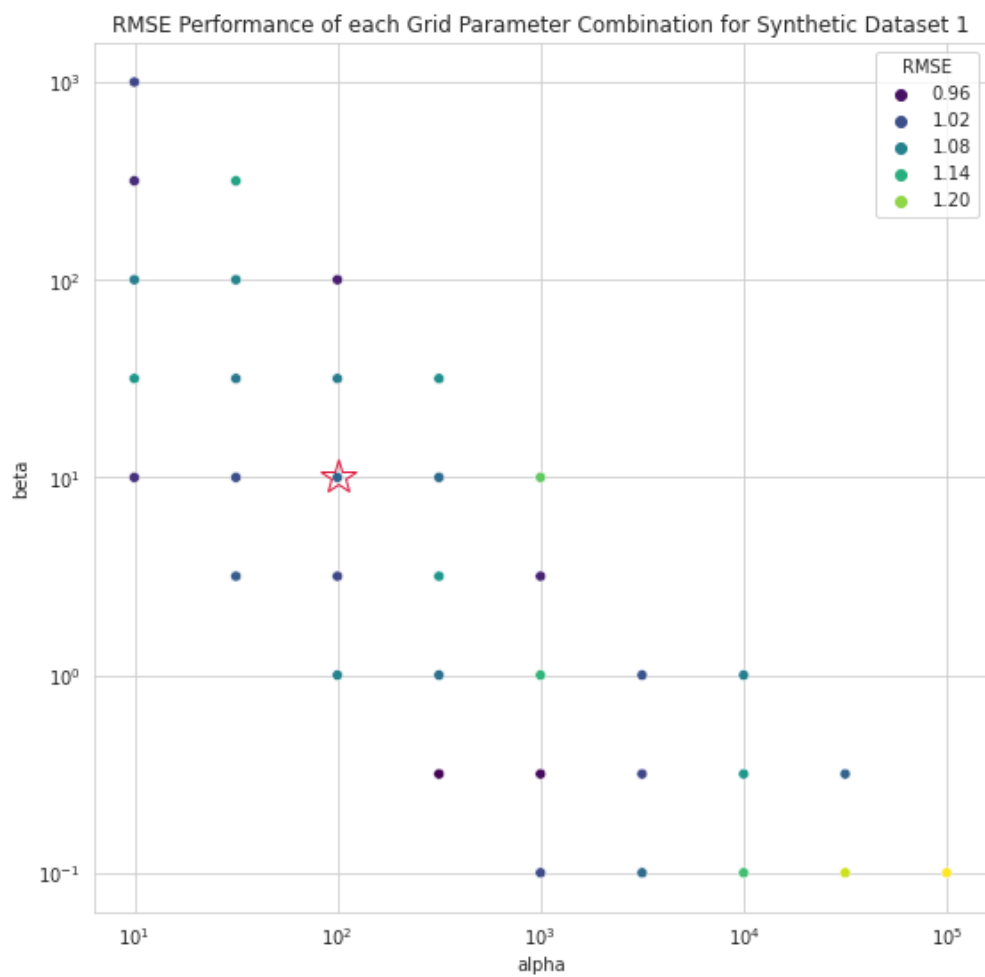


Figure 19: Root mean squared error of each parameter combination's estimate with respect to synthetic dataset 1. The star represents the dataset's true parameter combination.

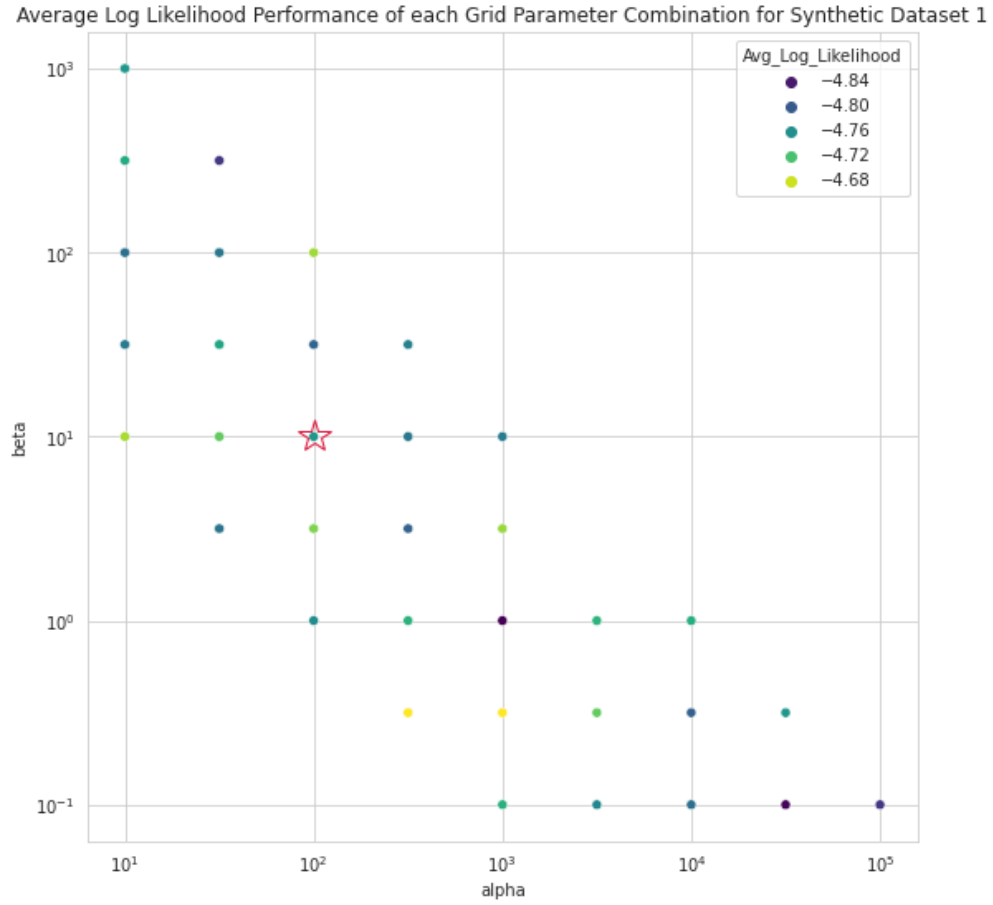


Figure 20: Time-averaged log-likelihood that synthetic dataset 1 originates from each parameter combination's ensemble of simulations. The star represents the dataset's true parameter combination.

Average Cross-Correlation Performance of each Grid Parameter Combination for Synthetic Dataset 1

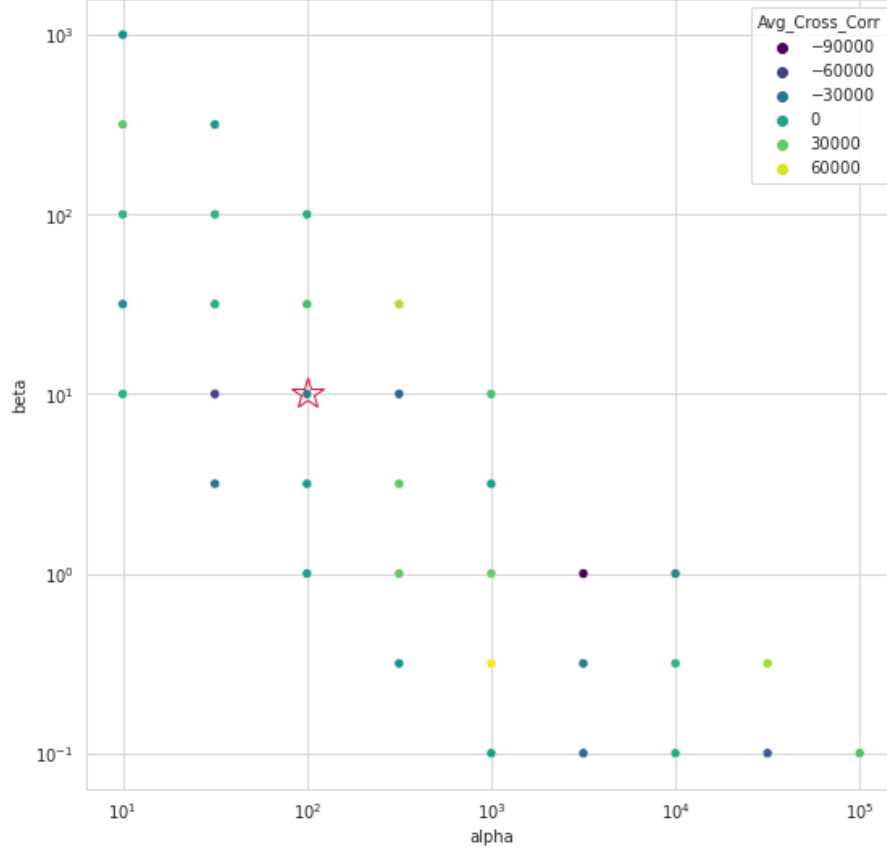


Figure 21: Time-averaged cross-correlation between synthetic dataset 1 and the ensemble average of a parameter combination's simulations, evaluated for each parameter combination on the grid. The star represents the dataset's true parameter combination.

Table 8: ($\alpha = 100, \beta = 10.0$) Grid search results for parameter combinations that perform optimally on various metrics with respect to synthetic dataset 1. These metrics seek to minimize the RMSE of the estimate with respect to the data, maximize the average log-likelihood that the synthetic data at a particular point in time came from the estimated ensemble, and maximize the time-averaged cross-correlation between the estimate and the ensemble.

ID	α	β	RMSE	Avg Log-Likelihood	Avg Cross-Correlation
True Data	100	10	1.04	-4.75	-25 400
Min RMSE	316	0.316	0.946	-4.67	-9850
Max Likelihood	1000	0.316	0.954	-4.67	68 800
Max Correlation	1000	0.316	0.954	-4.67	68 800

Table 9: ($\alpha = 100, \beta = 10.0$) Grid search results for parameter combinations that perform above-average on all tested performance metrics for synthetic dataset 1. The geometric mean values of the contact parameters in this dataset are $\alpha \approx 268$ N and $\beta \approx 5.18$ s/m.

α	β	RMSE	Avg Log-Likelihood	Avg Cross-Correlation
10.0	10.0	0.990	-4.69	11 100
10.0	316	0.984	-4.74	27 700
100	100	0.970	-4.69	6470
316	1.00	1.06	-4.73	31 100
1000	0.316	0.954	-4.67	68 800
1000	3.16	0.975	-4.69	-8.92
31600	0.316	1.04	-4.75	46 500

Table 10: ($\alpha = 100, \beta = 10.0$) Grid search method's contact parameter estimates for synthetic dataset 1

True α (N)	True β (s/m)	True γ (Ns/m)	$\hat{\alpha}$ (N)	$\hat{\beta}$ (s/m)	$\hat{\gamma}$ (Ns/m)
100	10.0	1000	268	5.18	1390

Table 11: ($\alpha = 100, \beta = 10.0$) Unscented Kalman filter's contact parameter estimates for synthetic dataset 1

True α (N)	True β (s/m)	True γ (Ns/m)	$\hat{\alpha}$ (s/m)	$\hat{\beta}$ (s/m)	$\hat{\gamma}$ (Ns/m)
100	10.0	1000	487	70.6	34400

The geometric mean of each parameter's estimates gives a better indication of the grid's average estimates for α and β , since the grid's parameter values are spaced on a logarithmic scale. The geometric average parameter values of this dataset are $\alpha \approx 268$ N and $\beta \approx 5.18$ s/m, which are far closer to the synthetic dataset's contact parameters than the average values of α and β . These parameter estimates are stored in Table 10.

6.2.2 Unscented Kalman Filtering Results

For the first dataset, the Kalman filter's approximations for α and β are higher than the true values of $\alpha = 100$ N and $\beta = 10.0$ s/m. After the transients decay, the average estimate of α is approximately 487 N with a standard deviation of 49.0 N, while the approximated β has an average value of 70.6 s/m and a standard deviation of 4.46 s/m. This yields an average product of $\gamma = \alpha\beta \approx 34400$ Ns/m, 34.4 times greater than its actual value of 1000 Ns/m. The high value of γ indicates that the system estimated by the unscented Kalman filter is approaching the point of critical damping.

If the contact force acting on the core barrel is approximated by a linearly viscous force with a damping coefficient of γ , the contact model can be combined with the core barrel's state-space dynamics matrix according to the relationship

$$A_{\text{new}} = A - B_2\gamma C_2 \quad (6-2)$$

This new dynamics matrix contains information regarding the damping ratios and natural frequencies of the new system's modes. The linear viscous contact force model is an approximation of the hyperbolic tangent contact force's influence on the core barrel system for contact point velocities below the characteristic velocity. The hyperbolic tangent model deviates from the linearly viscous model about the characteristic velocity by limiting the contact force such that it does not increase past a value of α . This constraint indicates that at higher velocities, the hyperbolic tangent contact model provides less damping to the system than the linear viscous model. Still, the linear viscous contact model provides insight as to the contact force's impact on the core barrel system's damping ratios. The contact force should have a measurable impact on the core barrel system's response without critically-damping any of the system's modes so long as γ falls within 50 N s/m to 50 000 N s/m. For γ values below 50.0 N s/m, the contact force's impact on the core barrel system is negligible. For γ values above 50000 N s/m, though, two of the core barrel system's modes become critically damped.

The unscented Kalman filter's parameter estimates suggest that the system has a γ value of approximately 34400 N s/m instead of its true value of 1000 N s/m. A linear viscous contact force with a damping coefficient of $\gamma \approx 1000$ N s/m would shift the core barrel system's highest damping ratio from 0.10 to 0.12. In contrast, the Kalman filter estimate's equivalent damping coefficient of $\gamma \approx 34400$ N s/m would increase the highest damping ratio to a value of 0.72, far closer to critical damping.

6.2.3 Comparison of Results

The contact parameter estimates for synthetic dataset 1 are compared in Table 12. The unscented Kalman filter overestimates both contact force parameters for this dataset, while the grid search method overestimates α and underestimates β . The grid search method's parameter estimates are far closer to the true values than the Kalman filter's parameter estimates.

Table 12: ($\alpha = 100, \beta = 10.0$) Comparison of contact parameters estimated for synthetic dataset 1, and the ratio of each estimate to its true value

Dataset	Parameter	True	GS Est.	KF Est.	GS Est. Ratio	KF Est. Ratio
Case 1	α	100	268	487	2.68	4.87
	β	10.0	5.18	70.6	0.518	7.06

6.3 Synthetic Dataset 2

Another synthetic dataset is generated with contact parameter values of $\alpha = 10^{1.5} = 31.6$ N and $\beta = 10^{2.5} = 316$ s/m. This dataset has a contact parameter product of $\gamma = 10000$ N s/m.

6.3.1 Grid Search Results

Each parameter combination on the grid has its performance evaluated according to each of the performance metrics with respect to synthetic dataset 2. The results are shown in Figures 22 through 24. The performances of the optimal parameter combinations for this dataset are displayed in Table 13 alongside the performance of the dataset’s actual set of contact parameters. Only the 7 parameter combinations listed in Table 14 perform above-average on all performance metrics for this synthetic dataset. These 7 combinations have average parameter values of $\alpha = 4820$ N and $\beta = 107$ s/m, with standard deviations of 11800 N and 148 s/m respectively. The geometric average parameter values for this dataset are $\alpha \approx 164$ N and $\beta \approx 10.0$ s/m, which combine to form a product of $\gamma \approx 1640$ N s/m. This estimated contact parameter product is roughly a factor of 6 below the actual product value of $\gamma = 10000$ N s/m.

6.3.2 Unscented Kalman Filtering Results

The unscented Kalman filter’s estimates for the new combination of α and β remain almost the same as for the previous parameter combination: the average value for α is 480

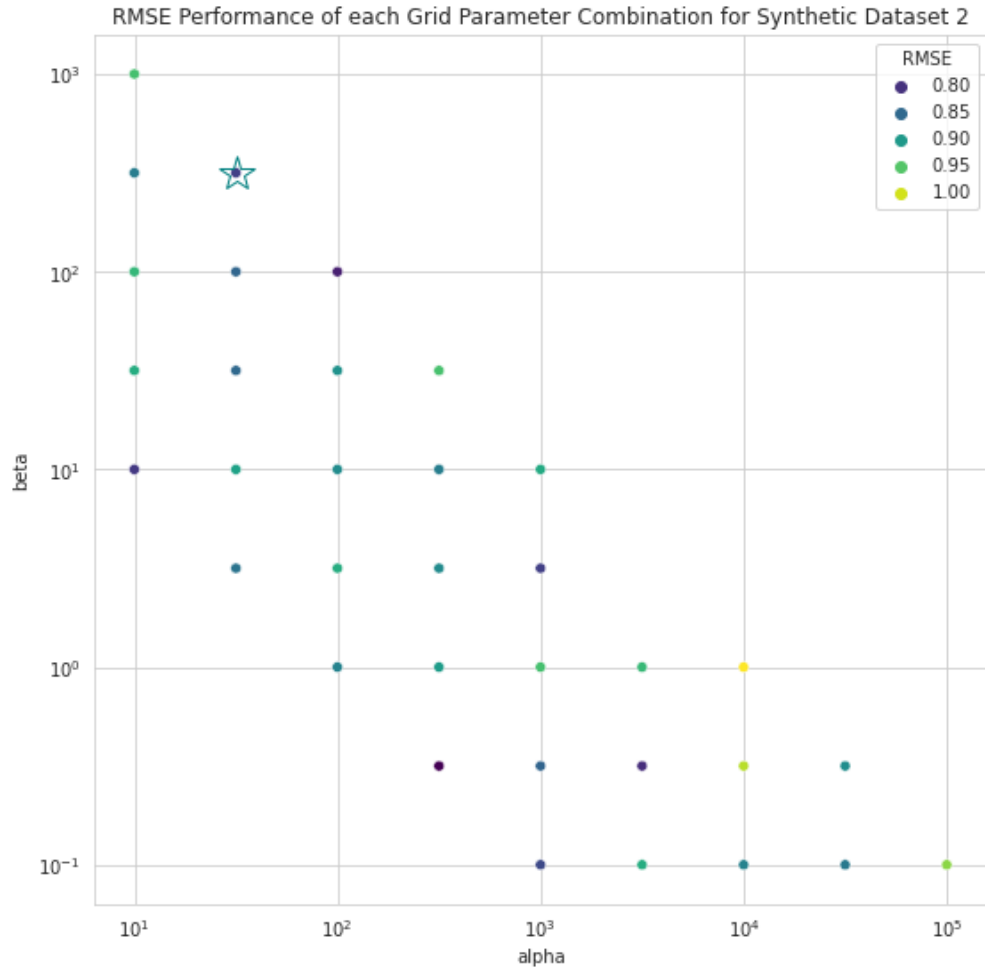


Figure 22: Root mean squared error of each parameter combination's estimate with respect to synthetic dataset 2. The star represents the dataset's true parameter combination.

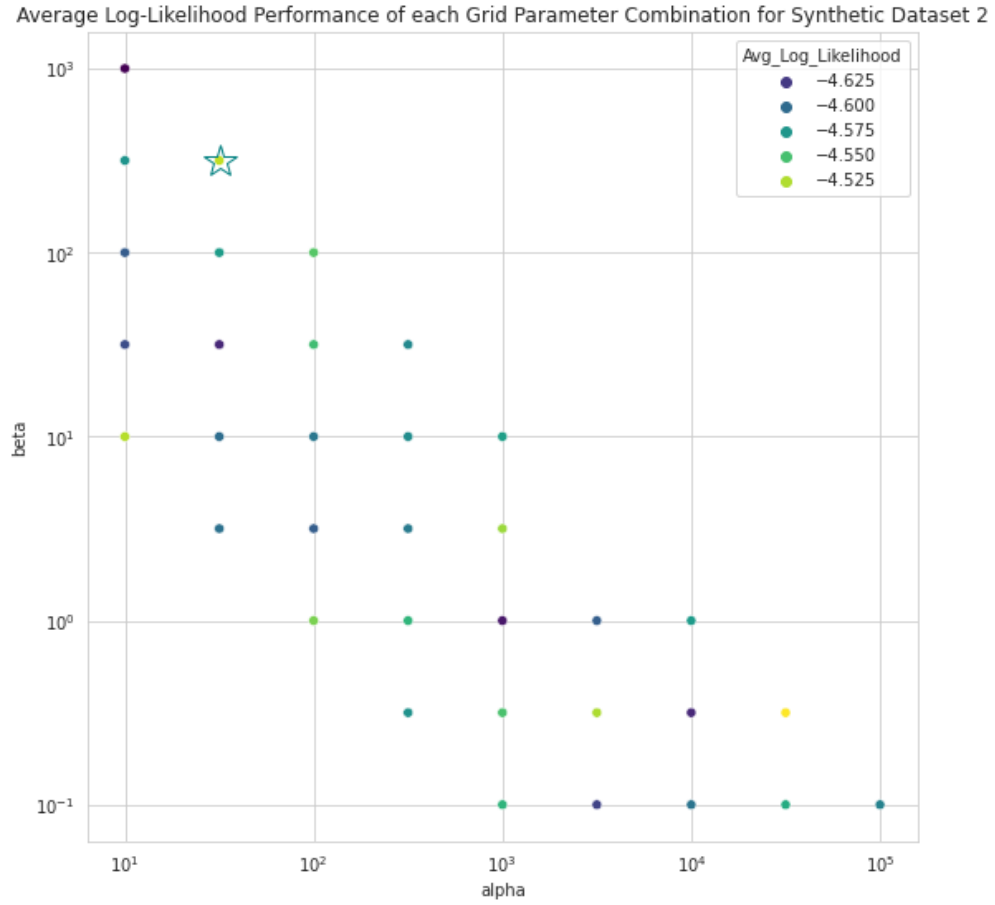


Figure 23: Time-averaged log-likelihood that synthetic dataset 2 originates from each parameter combination's ensemble of simulations. The star represents the dataset's true parameter combination.

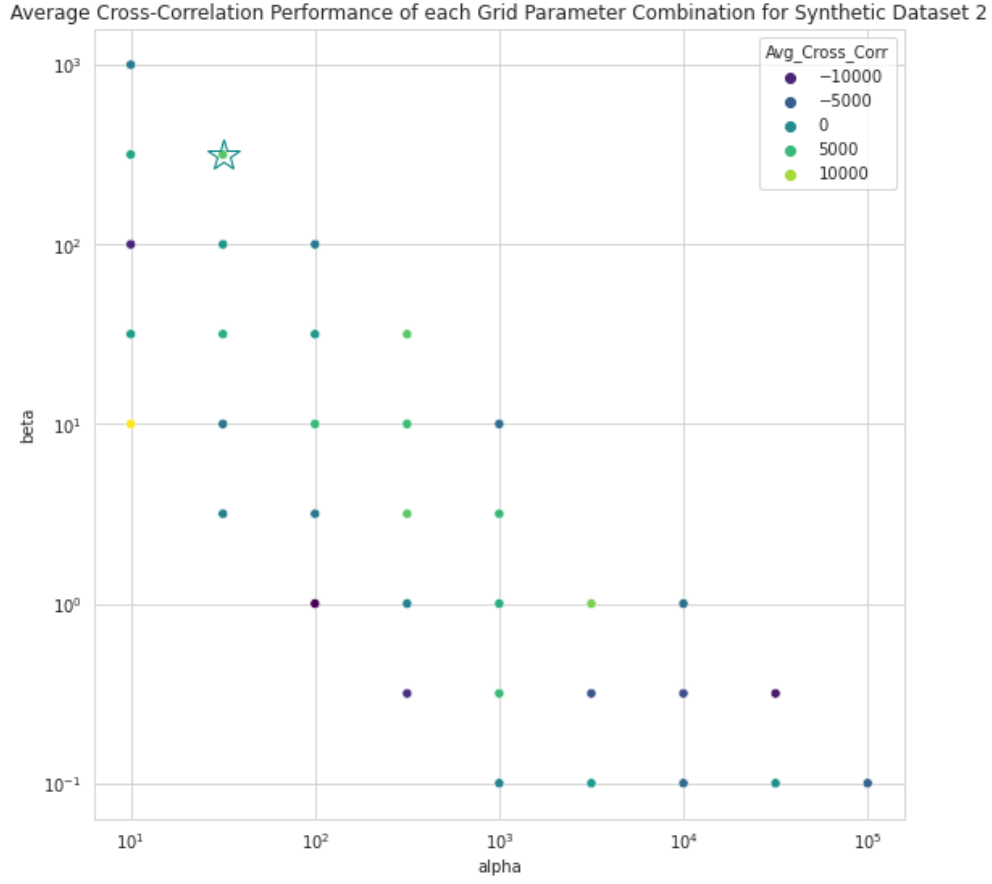


Figure 24: Time-averaged cross-correlation between synthetic dataset 2 and the ensemble average of a parameter combination’s simulations, evaluated for each parameter combination on the grid. The star represents the dataset’s true parameter combination.

Table 13: ($\alpha = 31.6, \beta = 316$) Grid search results for parameter combinations that perform optimally on various performance metrics for synthetic dataset 2

ID	α	β	RMSE	Avg Log-Likelihood	Avg Cross-Correlation
True Data	31.6	316	0.812	-4.52	6670
Min RMSE	316	0.316	0.764	-4.58	-9040
Max Likelihood	31600	0.316	0.889	-4.51	-10 900
Max Correlation	10.0	10.0	0.806	-4.52	13 600

Table 14: ($\alpha = 31.6, \beta = 316$) Grid search results for parameter combinations that perform above-average on all performance metrics of interest, with respect to synthetic dataset 2. These parameters have geometric average values of $\alpha \approx 164$ N and $\beta \approx 10.0$ s/m.

α	β	RMSE	Avg Log-Likelihood	Avg Cross-Correlation
10.0	10.0	0.806	-4.52	13 600
10.0	316	0.871	-4.58	2730
31.6	100	0.847	-4.57	1340
31.6	316	0.812	-4.52	6670
1000	0.316	0.846	-4.55	5210
1000	3.16	0.812	-4.53	4870
31600	0.100	0.866	-4.56	439

Table 15: ($\alpha = 31.6, \beta = 316$) Grid search method’s contact parameter estimates for synthetic dataset 2

True α (N)	True β (s/m)	True γ (N s/m)	$\hat{\alpha}$ (N)	$\hat{\beta}$ (s/m)	$\hat{\gamma}$ (N s/m)
31.6	316	10000	164	10.0	1640

Table 16: ($\alpha = 31.6, \beta = 316$) Unscented Kalman filter’s contact parameter estimates for synthetic dataset 2

True α (N)	True β (s/m)	True γ (Ns/m)	$\hat{\alpha}$ (s/m)	$\hat{\beta}$ (s/m)	$\hat{\gamma}$ (Ns/m)
31.6	316	10000	480	69.7	33500

Table 17: ($\alpha = 31.6, \beta = 316$) Comparison of contact parameter estimates for synthetic dataset 2, and the ratio of each estimate to its true value

Dataset	Parameter	True	GS Est.	KF Est.	GS Est. Ratio	KF Est. Ratio
Case 2	α	31.6	164	480	5.19	15.2
	β	316	10.0	69.7	0.0316	0.221

N, and the average of β is 69.7 s/m. The product of these two parameter estimates is 33500 Ns/m, which is 3.35 times greater than the true product of 10000 Ns/m. The highest-damped mode for a simulation with a γ value of 33500 Ns/m has a damping ratio of 0.69, indicating that the mode is approaching critical damping.

6.3.3 Comparison of Results

The contact parameter estimates for synthetic dataset 2 found through both the grid search approach and the unscented Kalman filter are displayed in Table 17. These estimates are terrible approximations of the synthetic dataset’s true parameter combination. Both methods overestimate α and underestimate β .

The grid search method’s estimate of α is a factor of 5.19 above the true value, while the unscented Kalman filter’s α estimate is a factor of 15.2 greater than the dataset’s true α . The unscented Kalman filter’s parameter estimate for β is a factor of 0.221 below the dataset’s true value, and the grid search approach’s β estimate is less than the true β value by a factor of 0.0316.

6.4 Synthetic Dataset 3

Two other synthetic datasets are generated using parameter values not located on the grid of contact parameter combinations. The first of these datasets is created using $\alpha = 490$ N and $\beta = 70.0$ s/m. These parameter values are selected to compare the grid search method's contact parameter estimates to an already-evaluated unscented Kalman filter's estimates. The unscented Kalman filter method provided the parameter values of $\alpha = 490$ N and $\beta = 70.0$ s/m as contact parameter estimates for the previous two synthetic datasets. The Kalman filter method was then applied to a synthetic dataset generated using $\alpha = 490$ N and $\beta = 70.0$ s/m to determine if these values are the only contact parameter estimates provided by the unscented Kalman filter. The grid search method's estimates and the unscented Kalman filter's estimates can only be compared if both methods are applied to the same synthetic dataset. So, the grid search method is applied to the synthetic dataset so that the previously-evaluated Kalman filter parameter estimates for that dataset can be re-used in the method comparison.

6.4.1 Grid Search Results

The performance of each parameter combination on the grid is evaluated with respect to synthetic dataset 3 according to each metric. These performances are visualized in Figures 25 through 27. The dataset's optimal parameter combination according to each performance metric is listed in Table 18. The collection of 6 parameter combinations found in Table 19 are the only ones that perform better-than-average on every performance metric for this synthetic dataset. The geometric averages of these parameter values are $\alpha \approx 100$ N and $\beta \approx 3.83$ s/m.

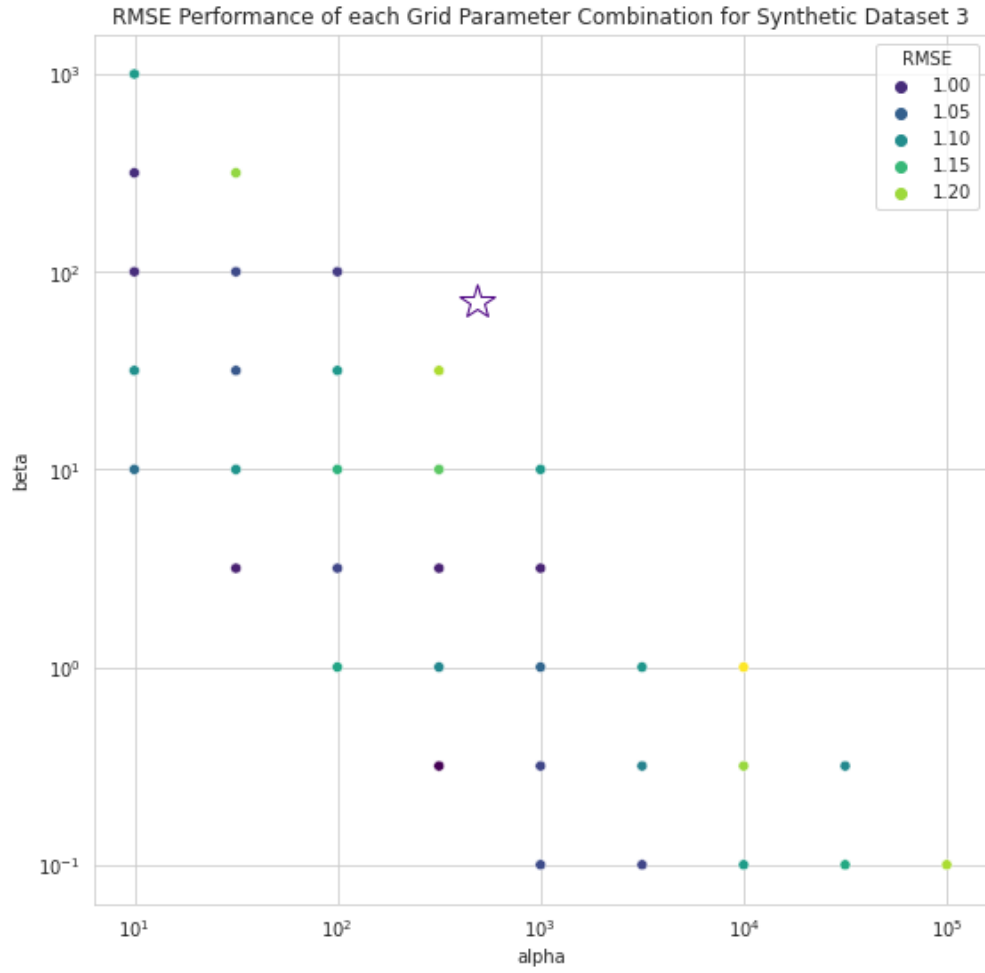


Figure 25: Root mean squared error of each parameter combination on the grid with respect to synthetic dataset 3. The star indicates the dataset's true contact parameters.

Average Log-Likelihood Performance of each Grid Parameter Combination for Synthetic Dataset 3

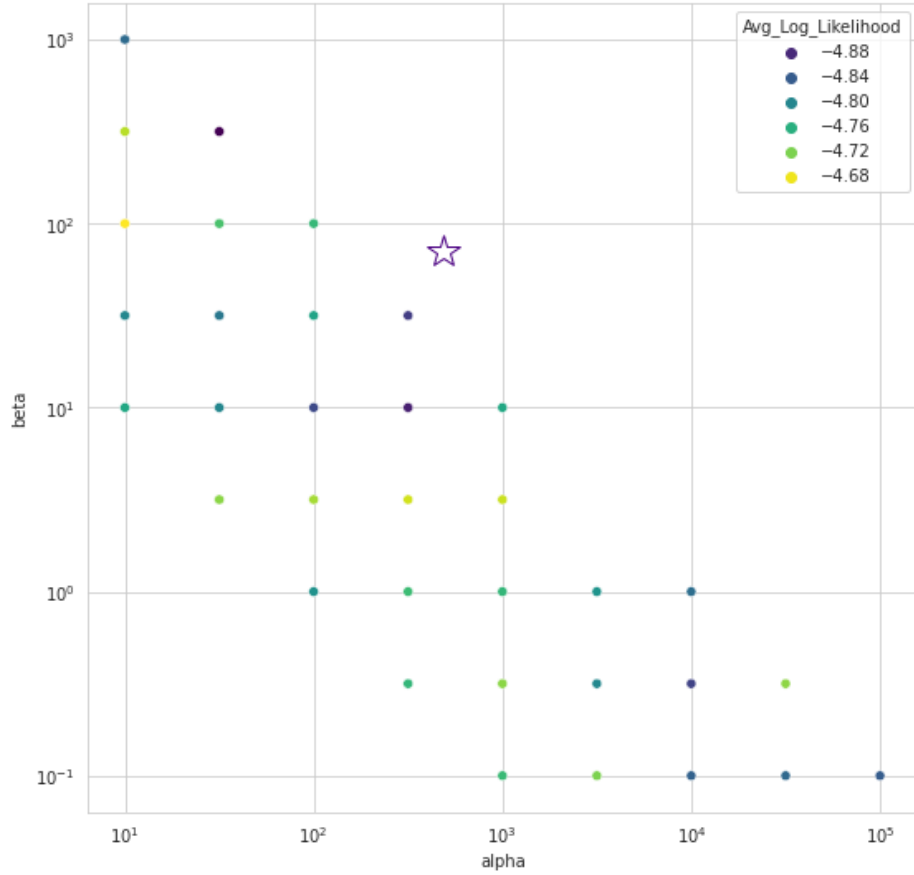


Figure 26: Time-averaged log-likelihood that synthetic dataset 3 originates from a parameter combination's ensemble of simulations, evaluated at every parameter combination on the grid. The star indicates the dataset's true contact parameters.

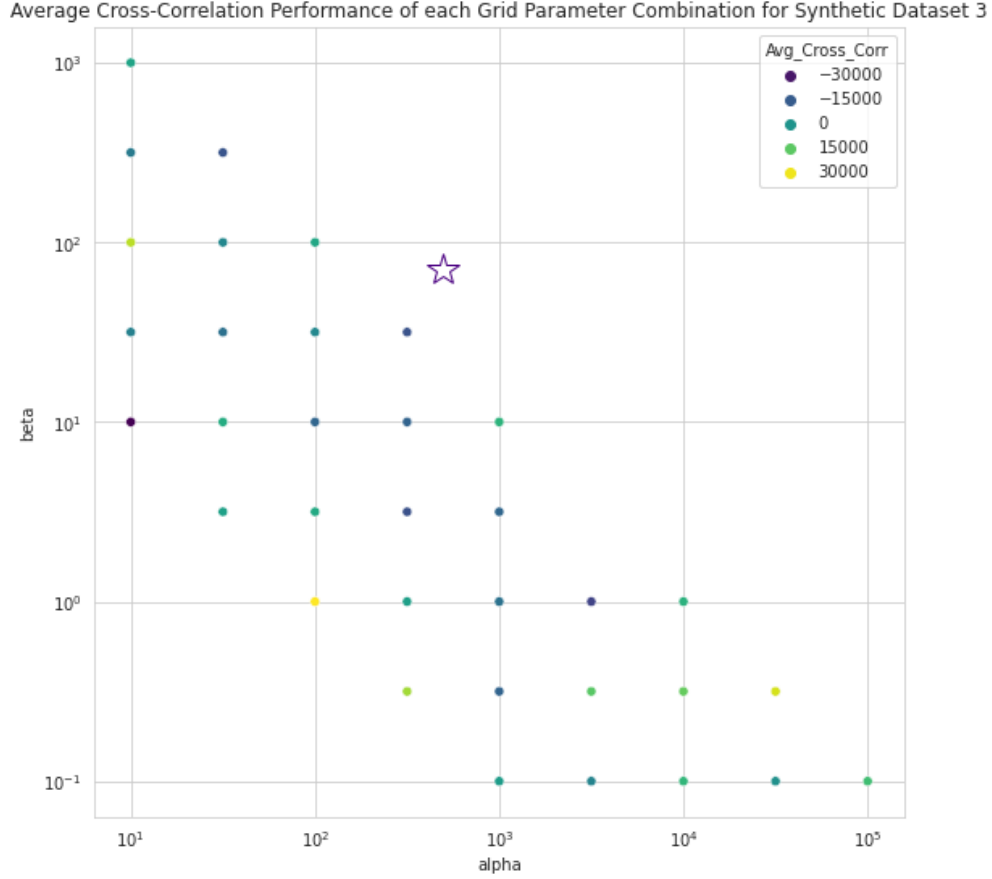


Figure 27: Time-averaged cross-correlation between synthetic dataset 3 and the ensemble average of a parameter combination’s simulations, evaluated at every parameter combination on the grid. The star indicates the dataset’s true contact parameters.

Table 18: ($\alpha = 490, \beta = 70.0$) Parameter combinations that perform optimally for synthetic dataset 3 according to each performance metric. This grid does not contain the true contact parameter combination, so the true combination’s performance on the various metrics cannot be evaluated.

ID	α	β	RMSE	Avg Log-Likelihood	Avg Cross-Correlation
Min RMSE	316	0.316	0.967	−4.75	22 600
Max Likelihood	10.0	100	1.00	−4.67	24 800
Max Correlation	100	1.00		−4.79	31 600

Table 19: ($\alpha = 490, \beta = 70.0$) Contact parameter combinations that performed better than average on all metrics across the grid for synthetic dataset 3. The geometric average parameter values for this subset are $\alpha \approx 100$ N and $\beta \approx 3.83$ s/m.

α	β	RMSE	Avg Log-Likelihood	Avg Cross-Correlation
10.0	100	1.00	-4.67	24 800
31.6	3.16	0.991	-4.72	3210
100	3.16	1.02	-4.71	5600
100	100	1.01	-4.75	5160
316	0.316	0.967	-4.75	22 600
1000	0.100	1.03	-4.75	2090

Table 20: ($\alpha = 490, \beta = 70.0$) Unscented Kalman filter’s contact parameter estimates for synthetic dataset 3

True α (N)	True β (s/m)	True γ (N s/m)	$\hat{\alpha}$ (s/m)	$\hat{\beta}$ (s/m)	$\hat{\gamma}$ (N s/m)
490	70.0	34300	665	108	71800

Table 21: ($\alpha = 490, \beta = 70$) Comparison of contact parameters estimated for synthetic dataset 3, and the ratio of each estimate to its true value

Dataset	Parameter	True	GS Est.	KF Est.	GS Est. Ratio	KF Est. Ratio
Case 3	α	490	100	665	0.204	1.36
	β	70	3.83	108	0.0547	1.54

6.4.2 Unscented Kalman Filtering Results

For a dataset generated using $\alpha = 490$ N and $\beta = 70.0$ s/m, the unscented Kalman filter’s average parameter estimates are approximately $\alpha \approx 665$ N and $\beta \approx 108$ s/m. The product of the dataset’s true parameters $\gamma = \alpha\beta$ is 34300 N s/m, 34.3 times its original value of $\gamma = 1000$ N s/m. If the simulation used a linear viscous contact force with the product of the parameter estimates $\gamma = \alpha\beta \approx 71800$ N s/m as its damping coefficient, the resulting core barrel system would have two critically-damped modes: one with a natural frequency of 179 Hz, and the other with a natural frequency of 34 Hz.

6.4.3 Comparison of Results

The contact parameter estimates produced by the grid search and unscented Kalman filter methods for synthetic dataset 3 are displayed in Table 21, alongside the ratio of each estimate to its true value. The unscented Kalman filter overestimates α and β , while the grid search method underestimates both parameters. The unscented Kalman filter’s contact parameter estimates are significantly closer to the true values than the grid search approach’s estimates.

6.5 Synthetic Dataset 4

The final tested synthetic dataset is associated with a true parameter combination of $\alpha = 660$ N and $\beta = 110$ s/m. This combination is also associated with a previously-evaluated unscented Kalman filter parameter estimate. The Kalman filter's parameter estimates for the dataset generated using $\alpha = 490$ N and $\beta = 70.0$ s/m were approximately $\hat{\alpha} \approx 660$ N and $\hat{\beta} \approx 110$ s/m. These estimated parameter values are used to generate a new synthetic dataset, to examine if the unscented Kalman filter's tendency to overestimate contact parameters persists when applied to datasets with higher-valued contact parameters. The results may only be used for model-comparison purposes if the grid search is applied to the same dataset. Therefore the grid search method is tested on a synthetic dataset with a true parameter combination of $\alpha = 660$ N and $\beta = 110$ s/m.

6.5.1 Grid Search Results

The performances of the grid's parameter combinations with respect to synthetic dataset 4 are displayed in Figures 28 through 30. The performance is evaluated using a different metric for each plot. The optimal parameter combinations for this dataset are collected within Table 22, and the subset of parameter combinations that perform better than average on every metric are shown in Table 23. A total of 6 parameter combinations satisfy this condition for the synthetic dataset. Their geometric average parameter values are $\alpha \approx 178$ N and $\beta \approx 3.83$ s/m.

6.5.2 Unscented Kalman Filtering Results

A dataset with a true parameter combination of $\alpha = 660$ N and $\beta = 110$ s/m produces unscented Kalman filter parameter estimates of $\alpha \approx 718$ N and $\beta \approx 125$ s/m. The product of this dataset's true contact parameters is $\gamma = 72600$ s/m, 72.6 times the original product and a factor of 2.1 greater than the product for the combination of $\alpha = 490$ N and $\beta = 70.0$ s/m. The dataset's true contact parameter product causes the core barrel system to have two critically-damped modes at natural frequencies of 182.5 Hz and 33.4 Hz. If the contact

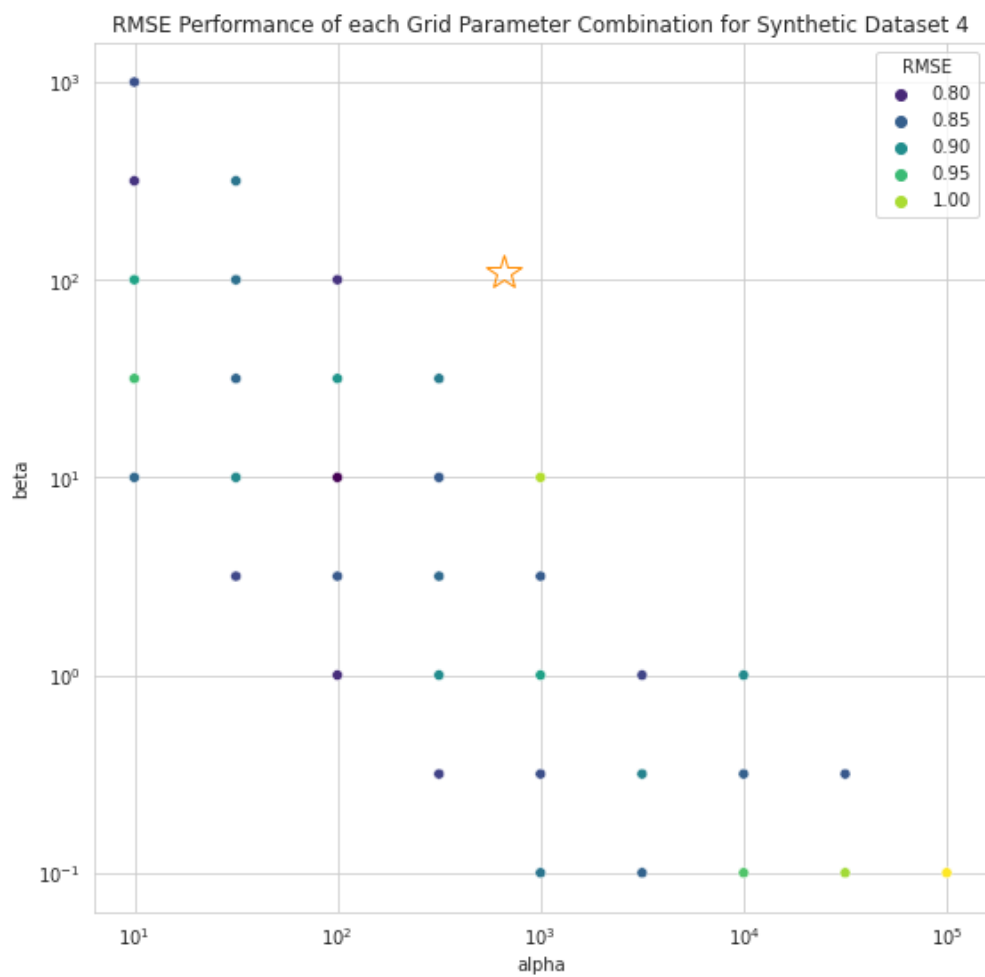


Figure 28: Root mean squared error of each parameter combination on the grid with respect to synthetic dataset 4. The star indicates the dataset's true contact parameters.

Average Log-Likelihood Performance of each Grid Parameter Combination for Synthetic Dataset 4

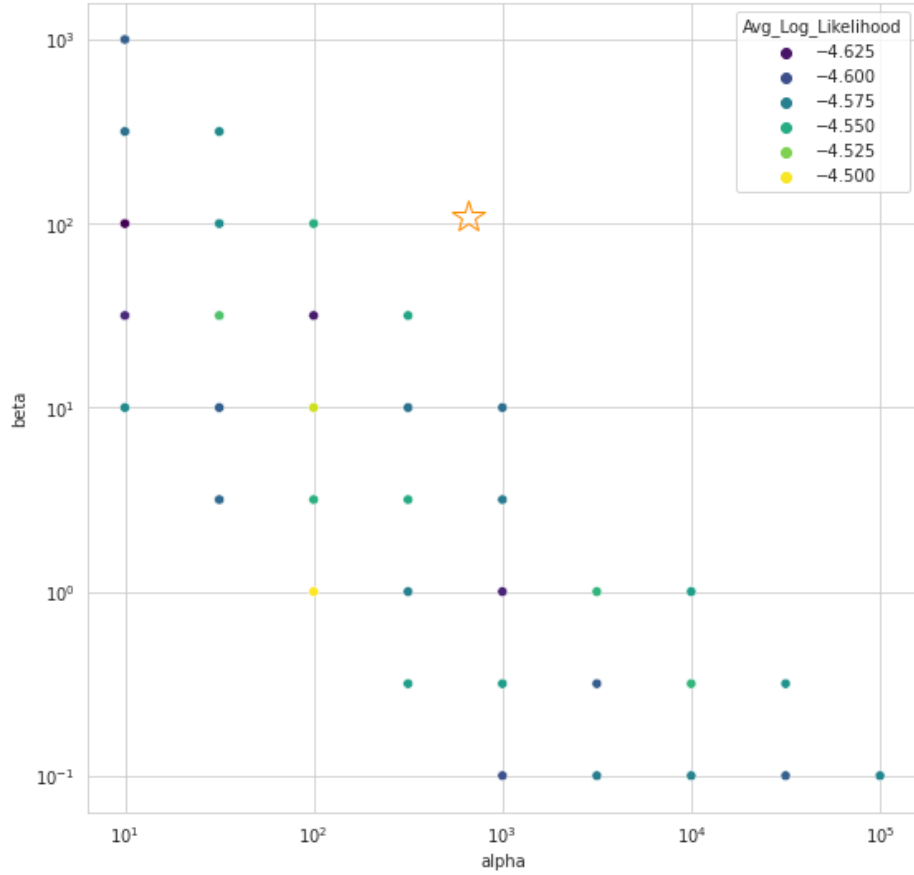


Figure 29: Time-averaged log-likelihood that synthetic dataset 4 originates from a parameter combination's ensemble of simulations, evaluated at every parameter combination on the grid. The star indicates the dataset's true contact parameters.

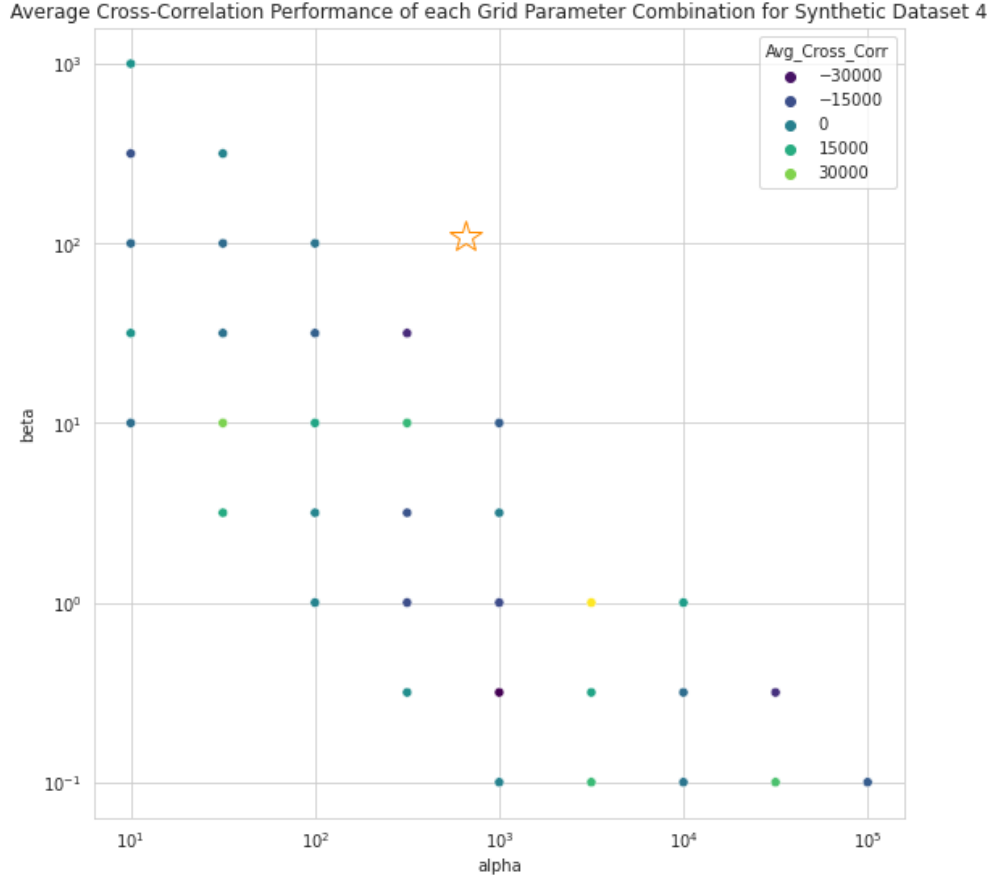


Figure 30: Time-averaged cross-correlation between synthetic dataset 4 and the ensemble average of a parameter combination’s simulations, evaluated at every parameter combination on the grid. The star indicates the dataset’s true contact parameters.

Table 22: $(\alpha = 660, \beta = 110)$ Grid search results for synthetic dataset 4. This parameter combination does not fall on the grid, so the performance metrics associated with the true parameters cannot be computed.

ID	α	β	RMSE	Avg Log-Likelihood	Avg Cross-Correlation
Min RMSE	100	10.0	0.771	-4.51	12 500
Max Likelihood	100	1.00	0.805	-4.50	1290
Max Correlation	3160	1.00	0.825	-4.54	44 700

Table 23: ($\alpha = 660, \beta = 110$) Parameter combinations that perform above-average on all performance metrics for synthetic dataset 4. This dataset’s geometric average parameters are $\alpha \approx 178$ N and $\beta \approx 3.83$ s/m.

α	β	RMSE	Avg Log-Likelihood	Avg Cross-Correlation
31.6	316	0.873	−4.57	1680
100	1.00	0.805	−4.50	1290
100	3.16	0.844	−4.55	1850
100	10.0	0.771	−4.51	12 500
316	0.316	0.823	−4.56	4830
3160	1.00	0.825	−4.54	44 700

force parameter product were 89800 N s/m, as predicted by the Kalman filter’s parameter estimates, the critically-damped modes would instead be located at natural frequencies of 237.7 Hz and 25.5 Hz.

6.5.3 Comparison of Results

The unscented Kalman filter and grid search method’s contact parameter estimates are compared in Table 25. The grid search method underestimates α by a factor of 0.270, and it underestimates β by a factor of 0.0348. In contrast, the Kalman filter’s estimate for α is greater than the true value by a factor of 1.09, and its β estimate is 1.14 times its true value. The unscented Kalman filter’s parameter estimates are far more accurate than the grid search approach’s estimates for synthetic dataset 4.

Table 24: ($\alpha = 660, \beta = 110$) Unscented Kalman filter’s contact parameter estimates for synthetic dataset 4

True α (N)	True β (s/m)	True γ (N s/m)	$\hat{\alpha}$ (s/m)	$\hat{\beta}$ (s/m)	$\hat{\gamma}$ (N s/m)
660	110	72600	718	125	89800

Table 25: ($\alpha = 660, \beta = 110$) Comparison of contact parameters estimated for synthetic dataset 4, and the ratio of each estimate to its true value

Dataset	Parameter	True	GS Est.	KF Est.	GS Est. Ratio	KF Est. Ratio
Case 4	α	660	178	718	0.270	1.09
	β	110	3.83	125	0.0348	1.14

6.6 Discussion and Comparison of Methods

The contact parameter approximations for each method and dataset are displayed in Figure 31, alongside the true parameters of the synthetic datasets. The markers on this plot are colored according to their synthetic datasets, and the shape indicates whether a marker is a true parameter combination, a Kalman filter estimate, or a grid search estimate. The ratios of the contact parameter estimates to the true values for each synthetic dataset serve as a means of comparison between the grid search and Kalman filter methods.

6.6.1 Comparison of Method Performance

The contact force parameter estimates generated through the unscented Kalman filter approach and through the grid search method are compiled in Table 26. These estimates are organized according to the true parameter values of the synthetic datasets. The parameter estimates generated through each method are compared to the true contact force parameters of the synthetic dataset.

The grid search method out-performs the unscented Kalman filter for synthetic dataset 1. The α estimate produced by the Kalman filter is a factor of 4.87 above the true value, and the β estimate produced by the same method is 7.06 times its true value. The grid search produces an α estimate 2.68 times its true value, and a β value that's a factor of 0.518 below the dataset's true β .

The estimates produced by both methods for synthetic dataset 2 are far from the true values, indicating almost equally terrible performance. These methods over-estimate α and

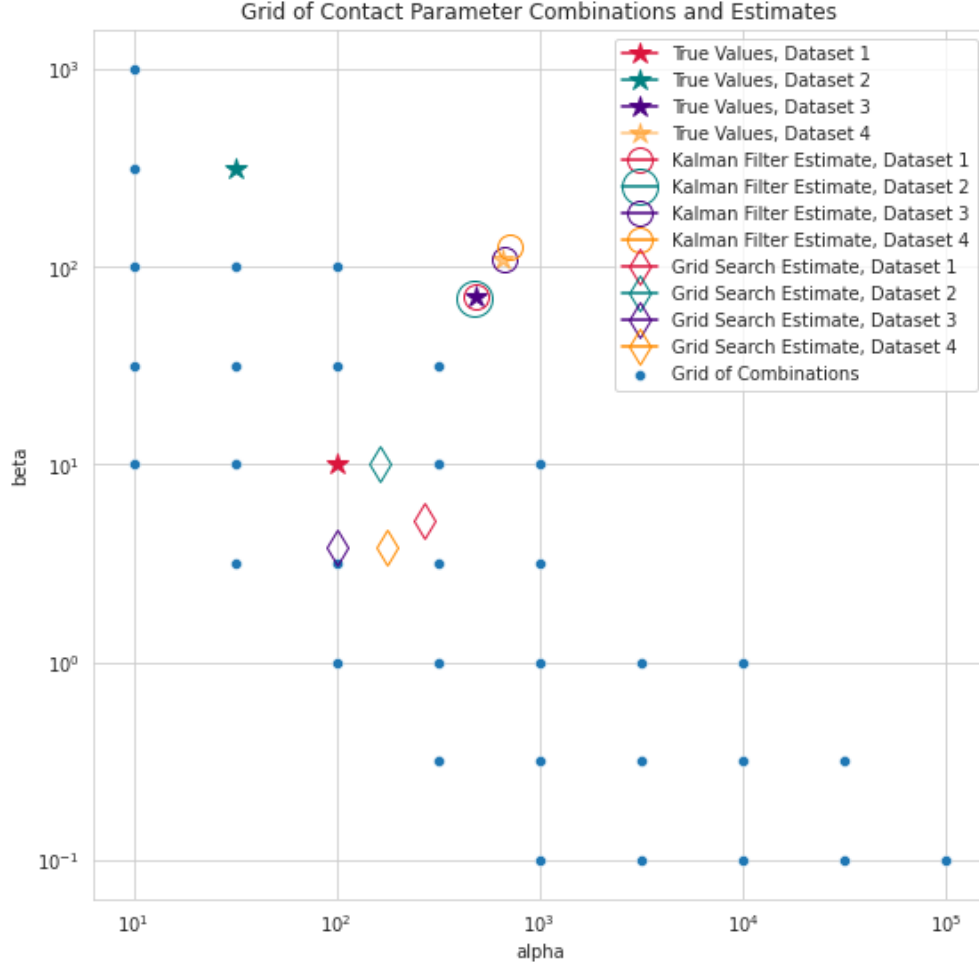


Figure 31: Plot of the contact parameter estimates across all datasets and estimation methods. The shapes of the markers indicate whether a parameter combination is a synthetic dataset's true parameters, a Kalman filter estimate, or a grid search estimate. The markers for the grid search and Kalman filter estimates are color-coded to match their respective synthetic datasets.

Table 26: Comparison of contact parameters estimated for 4 separate synthetic datasets through the grid search (GS) and Kalman filter (KF) methods. The ratio between each estimate and its associated true value is also computed.

Dataset	Parameter	True	GS Est.	KF Est.	GS Est. Ratio	KF Est. Ratio
Case 1	α	100	268	487	2.68	4.87
	β	10.0	5.18	70.6	0.518	7.06
Case 2	α	31.6	164	480	5.19	15.2
	β	316	10.0	69.7	0.0316	0.221
Case 3	α	490	100	665	0.204	1.36
	β	70	3.83	108	0.0547	1.54
Case 4	α	660	178	718	0.270	1.09
	β	110	3.83	125	0.0348	1.14

under-estimate β for this dataset. The estimate of α produced by the grid search method is a factor of 5.19 above the true value, while the unscented Kalman filter's α estimate is a factor of 15.2 greater than the truth. The grid search estimate of β is a factor of 0.0316 below the true value, and the Kalman filter's estimate is 0.221 times the true β . The grid search method produces a better estimate of α than the unscented Kalman filter for this dataset, yet the unscented Kalman filter creates a better estimate of β than the grid search method.

The unscented Kalman filter approach performs better than the grid search on datasets 3 and 4. The Kalman filter's contact parameter estimates for synthetic dataset 3 are factors of 1.36 and 1.54 above their true values for α and β , respectively. The grid search method's estimate for α is a factor of 2.04 below its true value, and its estimate for β is 0.0547 times the dataset's parameter value. For dataset 4, the Kalman filter's estimate of α is a factor of 1.09 above the true value, while the grid search method's estimate is a factor of 0.270 below the true value. Similarly, the Kalman filter estimate of β is 1.14 times the truth, and the grid search's approximation is a factor of 0.0348 below the true β .

A general trend emerges from this analysis: The unscented Kalman filter’s contact parameter estimates seem to out-perform the grid search method’s estimates for higher true values of α and β . In contrast, the grid search method appears to perform better than the unscented Kalman filter for lower true values.

6.6.2 Discussion of Unexpected Phenomena

Several aspects of the parameter estimates generated by both methods require explanation. Despite producing highly-accurate state and output estimates, the unscented Kalman filter almost always overestimates the contact force model’s parameters and by extension the contact force acting on the system. The Kalman filter somehow compensates for this increased contact force such that the estimated outputs and states remain accurate.

Also, no single performance metric for the grid search method is optimized at the synthetic dataset’s true contact parameter combination. This combination is known to have generated the synthetic data, but the performance metrics indicate that several other parameter combinations perform better on the metrics.

6.6.2.1 Deviation of Kalman Filtered Parameter Estimates

The Kalman filter’s contact parameter estimates significantly deviate from the true values used when generating the synthetic dataset. One reason for the difficulty in estimating the contact force parameters α and β is their interactions with each other. According to the hyperbolic tangent contact force model, if the velocity of the core barrel at the point of contact is far below the characteristic velocity $v_c = \frac{1}{\beta}$, the contact force u_2 takes on the form

$$u_2 = -\alpha \tanh(\beta y_2) \approx -\alpha \beta y_2 = -\gamma y_2 \quad (6-3)$$

where $\gamma = \alpha\beta$ is the effective viscous damping coefficient of the contact force model.

The unscented Kalman filter adjusts the estimated values of α and β until the system’s response approximates the measurement signal. However, the contact force at velocities below v_c depend only on γ , the product of α and β . So long as the contact point velocity is below the characteristic velocity and γ remains constant, changing the values of α and β

will have no impact on the system's response. Therefore the Kalman filter's estimates for α and β will randomly vary while the system attempts to reach the value of γ associated with the measured response.

Instead of this behavior, though, the Kalman filter's estimates for both α and β are several times greater than their true values: For synthetic dataset 1, which has true parameter values of $\alpha = 100$ N and $\beta = 10$ s/m, the estimate for α settles near a value of 487 N, and the approximate value of β approaches 70.6 s/m. This yields a product of $\gamma = \alpha\beta \approx 34400$ Ns/m, 34.4 times greater than its actual value of 1000 Ns/m.

When another synthetic dataset with drastically different contact force parameters is tested, the Kalman filter's estimated parameters still remain approximately the same. As previously mentioned, for a synthetic dataset generated with $\alpha = 31.6$ N and $\beta = 316$ s/m, the unscented Kalman filter's average parameter estimates are 480 N for α and 69.7 s/m for β . This synthetic dataset even has a true γ value of 10000 Ns/m, 10 times the previous dataset's γ value, and yet the Kalman filter approximates the values of α and β for both datasets as being nearly identical.

The deviation of the contact parameter estimates from their true values could be excused so long as the estimates recreate the true value of $\gamma = \alpha\beta$. However, the contact force parameter approximation method should be capable of recognizing when two datasets have different values of γ . The Kalman filter cannot be expected to accurately recreate the hyperbolic tangent model of the contact force acting on the system if it cannot extract even a basic viscous damping constant from the measured signal. The observed lack of change in parameter estimates could be explained if we assume the unscented Kalman filter's estimates do not significantly change for a factor of 10 increase in the synthetic dataset's true parameter product.

Following the above assumption, the unscented Kalman filter is applied to a system with significantly larger contact parameters such that the new dataset's contact parameter product is greater than a factor of 10 above the original's. If applied to synthetic dataset 3, which has true parameter values of $\alpha = 490$ N and $\beta = 70.0$ s/m, the unscented Kalman filter's parameter estimates increase to $\alpha \approx 665$ N and $\beta \approx 108$ s/m. The product $\gamma = \alpha\beta$ for this dataset is 34300 Ns/m, 34.3 times the γ value associated with synthetic dataset 1.

Similarly, synthetic dataset 4 with a true parameter combination of $\alpha = 660$ and $\beta = 110$ produces unscented Kalman filter parameter estimates of $\alpha \approx 718$ and $\beta \approx 125$. The product of this dataset's parameters is $\gamma = 72600$, 72.6 times synthetic dataset 1's γ value and a factor of 2.12 greater than the contact parameter product for synthetic dataset 2.

The unscented Kalman filter previously produced near-identical parameter estimates for two datasets where the parameter product of one dataset was 10 times the other's: Both a synthetic dataset with $\gamma = 1000$ N s/m and a dataset with $\gamma = 10000$ N s/m produced parameter estimates near $\alpha \approx 490$ and $\beta \approx 70$. Yet the same Kalman filter now generates two different sets of parameter estimates for two synthetic datasets where one dataset's product is less than half the other's: A dataset with $\gamma = 34300$ N s/m produces estimates of $\alpha = 665$ N and $\beta = 108$ s/m, while a synthetic dataset generated using $\gamma = 72600$ N s/m has parameter estimates of $\alpha = 718$ N and $\beta = 125$ s/m.

The unscented Kalman filter only produces different contact parameter estimates for two synthetic datasets if the Kalman filter is sensitive enough to detect the differences between those datasets. Assuming the unscented Kalman filter's parameter estimates only depend upon the product of the synthetic dataset's contact parameters, if a Kalman filter is sensitive enough to identify that one dataset's contact parameter product is a factor of 2 greater than the other's, then it should be sensitive enough to identify that one dataset's parameter product is a factor of 10 greater than the other's. Furthermore, if significantly different contact parameter estimates are generated for two datasets where one contact parameter product is double the other, then two synthetic datasets where one's product is 10 times the other's should also have significantly different contact parameter estimates. However, the unscented Kalman filter produces different parameter estimates for two datasets whose products are $\gamma = 34300$ N s/m and $\gamma = 72600$ N s/m. This same method generates nearly identical parameter estimates for two datasets whose products are $\gamma = 1000$ N s/m and $\gamma = 10000$ N s/m. Therefore, the contact parameter estimates do not depend upon the synthetic dataset's contact parameter product alone, but on some other unknown factors as well.

6.6.2.2 Identification of the Best-Performing Grid Element

Each performance metric has its own optimal combination of contact parameters. For example, synthetic dataset 2 is generated using $\alpha = 31.6$ N and $\beta = 316$ N s/m. The grid search method then locates the parameter combination on the grid with the highest time-averaged likelihood of generating the synthetic dataset from its ensemble of simulations. The likelihood is maximized for a parameter combination of $\alpha = 31600$ N and $\beta = 0.316$ s/m. The root-mean-squared error of the ensembles with respect to the same dataset is also computed for every parameter combination. This error is minimized for a combination of $\alpha = 316$ N and $\beta = 0.316$ s/m. The time-averaged cross-correlation between a parameter combination’s ensemble and the synthetic dataset is computed over the entire grid as well. This performance metric is maximized at its own optimal parameter combination of $\alpha = 10.0$ N and $\beta = 10.0$ s/m.

None of the performance metrics identify the true parameter combination used in generating the synthetic data. Instead, the performance metrics must all be considered together when evaluating the data’s contact parameters. This is achieved by normalizing each performance metric by its mean and standard deviation, then isolating the parameter combinations that perform better-than-average on all three performance metrics. A geometric average is applied to the parameter combinations of this subset of the data, producing approximate values for α and β associated with the best-performing parameter combinations in the grid. This geometric average is often closer to the true parameter combination than the various “optimal” parameter combinations produced by each performance metric.

7.0 Summary and Conclusions

7.1 Summary

The 2D motion of a core barrel within a pressurized water reactor is modeled as a spring-mass-damper system excited by a random force from turbulence and damped by nonlinear contact forces. This model is used to simulate the core barrel system's response to a turbulent input and generate a synthetic dataset for analysis. The contact forces are assumed to follow a hyperbolic tangent function of the system's states, with two parameters α and β determining the maximum contact force and its characteristic velocity. The outputs of the synthetic dataset are analyzed to identify the unknown parameters within the nonlinear contact force function. These attempts to extract the contact parameters from the data rely on two methods: a grid search approach, and an unscented Kalman filter approach.

The grid search method approximates the contact parameters by evaluating the response of the core barrel over a grid of possible combinations of contact force parameters. These simulated responses are then compared to identify the contact parameter combination that most accurately reproduces the synthetic dataset. Multiple simulations are evaluated for each combination of parameters, with only the noise terms varying between simulations. These replications form an ensemble representing the average behavior of the core barrel system for those parameters. The ensemble's ability to recreate the synthetic dataset is evaluated through three separate performance metrics: likelihood, cross-correlation, and root-mean-squared error. The synthetic data should have a high likelihood of originating from the ensemble, the cross-correlation between the data and the ensemble average should be high, and the root-mean-squared error in the ensemble average with respect to the synthetic dataset should be minimal. The performance metrics are then compared amongst the parameter combinations on the grid. The combination that performs best on all metrics should be a close approximation for the contact parameters used in generating the synthetic dataset.

The second approach applies an unscented Kalman filter to the core barrel system. This method assumes the contact parameters undergo some disturbance with a known variance. The expected mean values and variances of the process noise, measurement noise, states, and contact parameters are then used to select a set of values representing the distributions of the system's states and inputs. This set of points is known as the system's sigma points. A function representing the core barrel system's response to the states and inputs transforms the set of sigma points. The resulting set of transformed points describe the distribution of the outputs for the given inputs and states. This process is repeated at every time point to provide an estimate for the system's states, outputs, and contact parameters.

Contact parameter estimates are evaluated through both methods for each synthetic dataset. The estimates are then compared to the true values associated with the synthetic dataset. The purpose of this analysis is to identify which method is better at extracting contact parameters from the data. Additionally, the approximated states and responses associated with the contact parameter estimates are compared to the synthetic dataset whenever possible. The estimated contact parameters closest to the true values should produce state and output estimates matching the behavior of the synthetic data.

7.2 Conclusions

The unscented Kalman filter method recreates the core barrel system's outputs with incredible accuracy, but its approximations for the contact force parameters are not always near the true values. Additionally, the contact parameter estimates are not particularly sensitive with respect to the true parameter values: The unscented Kalman filter's parameter estimates for a true parameter combination of $\alpha = 100$ N and $\beta = 10$ s/m are $\hat{\alpha} \approx 487$ N and $\hat{\beta} \approx 70.6$ s/m. A true parameter combination of $\alpha = 31.6$ N and $\beta = 316$ s/m generates a similar set of contact parameter estimates, $\hat{\alpha} \approx 480$ N and $\hat{\beta} \approx 69.7$ s/m.

The grid search method provides better estimates for the contact force parameters when the synthetic dataset's true parameter values are relatively low, such as the parameter combination of $\alpha = 100$ N and $\beta = 10.0$ s/m. For higher parameter values, such as $\alpha = 660$

N and $\beta = 110$ s/m, the unscented Kalman filter’s estimates are closer to the true values. Both methods struggle to approximate the contact parameters associated with certain synthetic datasets. For instance, when analyzing a synthetic dataset such that $\alpha = 31.6$ N and $\beta = 316$ s/m, the unscented Kalman filter’s estimate for α is closer to the true value than the grid search estimate. For this same dataset, the grid search method’s approximation of β is more accurate than the Kalman filter’s estimate. Overall, the performance of each contact parameter estimation method depends upon the synthetic dataset under analysis. Neither method performs better than the other on all datasets.

7.3 Contributions

Prior attempts to describe the motion of the core barrel system approximated the contact force using linear viscous damping. These models did not capture the transition of the contact force model from linear viscous damping at low velocities to constant Coulomb friction at higher velocities. Unlike prior research, the contact force applied in this report accounts for the nonlinear relationship between the contact force and the velocity of the core barrel at the point of contact. This research also attempts to identify two parameters describing the contact force instead of just one. This introduces potential sources of complexity to the problem, such as interactions between parameters and how those interactions impact the measured outputs.

The state-space matrices and the contact force function accurately model the core barrel’s response to an input force from turbulence. The ex-core neutron noise measurements are approximated as a linear combination of the system’s position states. In an actual core barrel system, though, the ex-core readings may not depend on the core barrel’s vertical displacement. Additionally, the core barrel’s motion in the model is restricted to a 2D plane, while a real core barrel in a PWR unit vibrates within a 3D space. The 2D model is adequate for attempting to approximate the contact force model’s behavior from ex-core neutron noise measurements.

Modeling the core barrel system and extracting the contact force model's parameters from the neutron noise measurements proved to be far more difficult than anticipated. When generating synthetic data in the discrete-time domain, the state-space model of the core barrel system could not be discretized due to the nonlinear feedback mechanism introduced by the contact force. This problem was circumvented by creating a fourth-order Runge-Kutta algorithm for approximating the states and outputs of the continuous-time system at discrete points in time. For the Kalman filter method, the nonlinearity of the contact force prevented the application of traditional Kalman filter approaches for parameter estimation. Instead, an unscented Kalman filter was applied to the core barrel system. The three performance metrics analyzed in the grid search method each produced a different optimal parameter combination for each dataset, necessitating a different approach that accounts for all three metrics simultaneously. Additionally, several months were spent debugging the data generation, core barrel simulation, and contact parameter estimation analysis code. These difficulties significantly delayed research into the other aspects of the project, such as the analysis of the relationship between the contact forces and the conditions of the reactor internals. Due to these delays, the contact parameter estimation method's applications to condition monitoring were not analyzed in this report. Such research shall remain for any aspiring researchers in the field of condition monitoring for nuclear power plants.

As for contact parameter estimation method performance, neither approach produces better estimates for all synthetic datasets. The grid search approach is better at estimating contact parameters in systems with lower contact force parameter values, while the unscented Kalman filter's estimates perform better than the grid search approach for synthetic datasets with higher parameter values. In some cases, the Kalman filter might produce a better estimate of α and a worse approximation of β when compared to the grid search method, or vice-versa. Each method's performance depends upon the dataset under analysis. If the dataset's true parameter values are unknown, the performance of each method cannot be evaluated. More research is required to improve these contact parameter estimation methods.

7.4 Future Work

The core barrel simulation could be made more realistic by incorporating 3D motion within the model. The current model only has 3 degrees of freedom, allowing for horizontal, vertical, and rotational motion of the structure within a 2D plane. A real core barrel moves in 3D space, with translational motion normal to the 2D plane and rotational motion about the plane's component axes. A 3D model of the core barrel system was not considered for this report because the additional degrees of freedom complicate the modeling process. Rewriting the system's equations of motion for 3 more degrees of freedom would be time-consuming, without yielding any additional benefits to the contact parameter estimation process. The 3D simulation of the core barrel would be useful for simulating the response of an actual core barrel system for purposes such as condition monitoring.

The contact force model tested in this report assumes the parameters α and β are identical for each contact point. However, if the contact points degrade at different rates, the parameter values at each contact point would no longer be equal. The simulation could be made more realistic by providing a separate set of contact parameters for each point of contact. This would allow for simulations of non-uniform degradation within the core barrel system.

The contact force's impact on the core barrel system's response could be approximated by an effective viscous damping force. This would be achieved by extracting the damping ratios of the core barrel system's modes from the output simulated for a given contact force. These could then be compared to damping ratios extracted from a simulation without the contact force. A method for approximating the damping ratios of the core barrel system's modes using the power spectral density of each output is outlined in Appendix A. The change in the damping ratios would indicate the contact force's impact on the system's response, and an effective damping coefficient could be found to recreate this same change using a viscous contact force. The unscented Kalman filter might approximate a single parameter in the form of an effective damping coefficient more accurately than its previous attempts at estimating two separate parameters to describe a nonlinear contact force.

Assuming the core barrel and contact force models are correct, the synthetic dataset generated for the simulation should approximate the response of an actual reactor core barrel. If the models are inaccurate, though, the simulation’s results may significantly deviate from a reactor’s ex-core neutron noise measurements. The accuracy of the models could be determined by comparing the simulations to data from a real PWR system. Furthermore, a training dataset from an actual reactor would serve as an excellent test for the grid search and Kalman filter methods’ capabilities in approximating the PWR’s behavior. The actual contact force parameters associated with this dataset would be unknown, so the approximations of the parameters would have no “true value” for comparison, but the simulated outputs could still be tested against the true response of the reactor. Once the contact parameter extraction method is improved and known to produce accurate estimates on synthetic datasets, testing the method on data from an actual reactor system would serve as an excellent proof-of-concept.

Appendix A Approximation of Damping Ratios

The damping ratios associated with the core barrel simulation's modes are extracted from the power spectral density of the system's output, as estimated through Welch's method. Each mode is identified on the power spectral density plot as a peak occurring at some resonance frequency ω_r . Two points on the resonance peak occur halfway between the peak's highest and lowest magnitudes. These are labelled the half-power points, and they are located at the half-power frequencies ω_1 and ω_2 on the power spectral density curve. The damping ratio ζ associated with the peak is approximated using the resonance frequency and the width between the peak's half-power frequencies, assuming $\omega_2 > \omega_1$ and $\zeta \ll \frac{1}{2}$.

$$\zeta \approx \frac{\omega_2 - \omega_1}{2\omega_r} \quad (\text{A-1})$$

This computation is repeated for each peak identified in the power spectral density plot.

One way to identify a peak is using a minimum prominence threshold. This method locates a local minimum on the curve, then searches for a local maximum such that the difference between the minimum and maximum exceeds some specified threshold. If another local minimum below the previous one is encountered before locating such a maximum, the lower value is selected as the peak's new minimum. After finding the maximum, another point on the curve to the right of the peak at approximately the same height as the first minimum is identified. The power spectral density plots of the core barrel system's outputs for simulations with and without the contact force are shown in Figure 32.

The peak's prominence is the height of the peak above the identified local minima. This differs from the peak's height, which is the peak's magnitude above or below zero. The width of the peak is approximated as the difference between the half-power frequencies. The damping ratio of the mode is then approximated as half the ratio between the peak width and the peak's resonance frequency, as shown in Equation A-1. The resonance frequency, height, width, and prominence of each peak in the power spectral density plot are computed in MATLAB using the `findpeaks` function. This command locates the peaks while applying any specified thresholds, such as a minimum prominence, minimum peak height, or

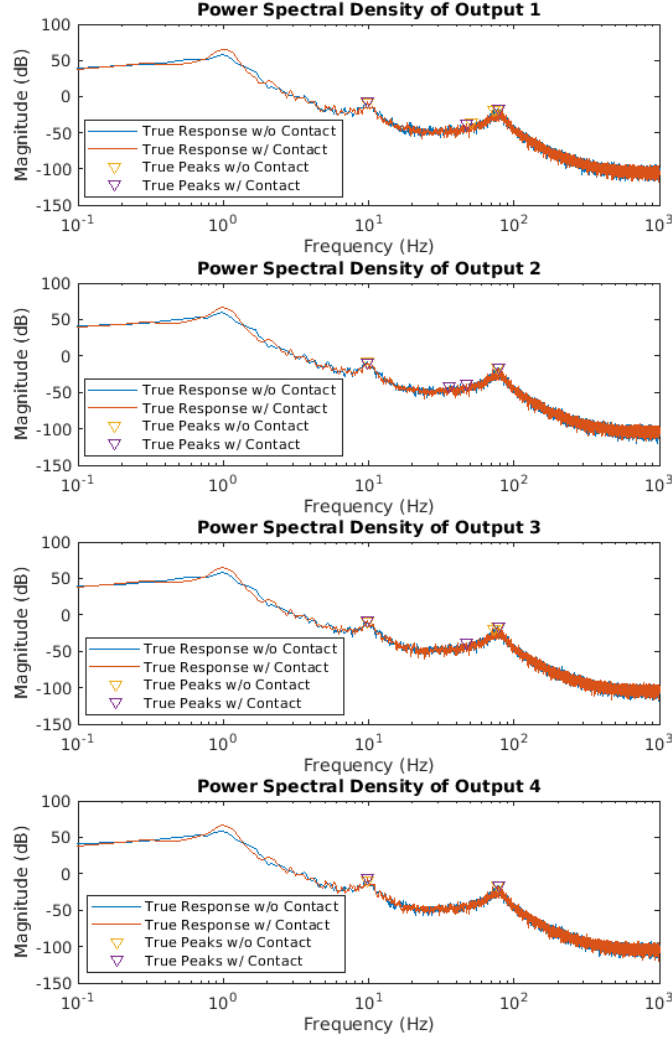


Figure 32: Power Spectral Density plots of the core barrel system's outputs for simulations with and without the contact force. The simulation that accounts for the contact force has contact parameter values of $\alpha = 100$ N and $\beta = 10$ s/m. Resonance peaks are identified using a minimum prominence threshold of 15 dB, minimum peak width of about 1.5 Hz, and a minimum peak height of -50 dB to exclude the output's noise floor.

a minimum or maximum peak width. It even allows the specification of the reference for the peak's width, with options of either the half-prominence width or the half-height width. For the core barrel system, the minimum prominence is set to 15 dB, the minimum peak width is specified as 0.1 Hz, and the minimum peak height threshold is placed at -50 dB. These thresholds allow the MATLAB command to identify the system's resonance peaks without accidentally mislabelling random variations in the power spectral densities as peaks.

The contactless simulation of the core barrel system is compared to a contact-damped simulation with contact parameters of $\alpha = 100$ N and $\beta = 10$ s/m. The resonance frequencies and modes for each output of these simulations are located in Tables 27 to 30. The contact force provides additional damping to the system, so the contact-damped simulations should have higher damping ratios than the contactless simulations.

The first resonance peak occurs near 10 Hz for every output. The damping ratios associated with this mode are 0.12 for Outputs 1, 2, and 3 when considering the contactless simulation. In this same simulation, the damping ratio of this mode for Output 4 is approximately 0.08. For the contact-damped simulation, the damping ratio of this mode is roughly 0.09 or 0.10 for every output. This mode tends to be lower for the contact-damped simulations than for the contactless simulations. The only exception is when analyzing Output 4, where the damping ratio of the contact-damped simulation is slightly higher than the damping ratio for the contactless simulation.

Several intermediate peaks occur between 10 Hz and 80 Hz on most outputs for both simulations. However, the frequencies of these peaks are not consistent between outputs, and they all have damping ratios of approximately 0.02. The low damping ratios and inconsistent resonance frequencies seem to indicate that these peaks are caused by noise rather than some significant mode of the core barrel system.

The final resonance peak occurs in every output at a frequency of approximately 80 Hz. The contactless simulation's outputs all have damping ratios of 0.11 or 0.12 for this mode. Outputs 1, 2, and 3 of the contact-damped simulation have damping ratios of 0.15 for this mode, while Output 4 of the simulation has a damping ratio of 0.13. The mode associated with this resonance peak has significantly more damping in the contact-damped simulation than in the contactless simulation.

Table 27: Resonance peaks and damping ratios for Output 1 of the core barrel system

Peak	Statistic	Contactless	Contact
Peak 1	Frequency (Hz)	9.8	9.9
	Width (Hz)	2.4	1.8
	Damping ratio	0.12	0.09
Peak 2	Frequency (Hz)	51	47
	Width (Hz)	1.7	2.2
	Damping ratio	0.02	0.02
Peak 3	Frequency (Hz)	72	N/a
	Width (Hz)	2.4	N/a
	Damping ratio	0.02	N/a
Peak 4	Frequency (Hz)	78	79
	Width (Hz)	17	23
	Damping ratio	0.11	0.15

Table 28: Resonance peaks and damping ratios for Output 2 of the core barrel system

Peak	Statistic	Contactless	Contact
Peak 1	Frequency (Hz)	9.8	9.8
	Width (Hz)	2.3	1.9
	Damping ratio	0.12	0.10
Peak 2	Frequency (Hz)	N/a	36
	Width (Hz)	N/a	1.7
	Damping ratio	N/a	0.02
Peak 3	Frequency (Hz)	N/a	47
	Width (Hz)	N/a	1.8
	Damping ratio	N/a	0.02
Peak 4	Frequency (Hz)	78	79
	Width (Hz)	17	23
	Damping ratio	0.11	0.15

Table 29: Resonance peaks and damping ratios for Output 3 of the core barrel system

Peak	Statistic	Contactless	Contact
Peak 1	Frequency (Hz)	9.8	9.8
	Width (Hz)	2.4	1.9
	Damping ratio	0.12	0.10
Peak 2	Frequency (Hz)	N/a	47
	Width (Hz)	N/a	1.7
	Damping ratio	N/a	0.02
Peak 3	Frequency (Hz)	73	N/a
	Width (Hz)	2.4	N/a
	Damping ratio	0.02	N/a
Peak 4	Frequency (Hz)	78	79
	Width (Hz)	17	25
	Damping ratio	0.11	0.15

Table 30: Resonance peaks and damping ratios for Output 4 of the core barrel system

Peak	Statistic	Contactless	Contact
Peak 1	Frequency (Hz)	9.8	9.9
	Width (Hz)	1.6	1.7
	Damping ratio	0.08	0.09
Peak 2	Frequency (Hz)	78	79
	Width (Hz)	18	21
	Damping ratio	0.12	0.13

Appendix B MATLAB Simulation Code

The synthetic datasets, unscented Kalman filter estimates, and the grid search method's ensembles of simulations are generated using MATLAB.

B.1 Synthetic Data Generation

The MATLAB code for generating synthetic data is listed below for a true parameter combination of $\alpha = 100$ N and $\beta = 10$ s/m. The true contact parameter values associated with a synthetic dataset are set by changing the values of `alpha` and `beta` in the code.

```
% 07/20/2022, Nicholas Harn
% Data generation for core barrel system
clear;
close all;
clc;
rng(1);

%% System dimensions
% Number of degrees of freedom
ss_mat.n_dof    = 3;
% Number of outputs
ss_mat.m_out    = 4;
% Number of process noise inputs (turbulent force)
ss_mat.n_w_in   = 3;
% Number of known inputs (contact force)
ss_mat.n_u_in   = 4;
```

```

%% Core Barrel Structure
% Properties known from Western-type PWR specs:
rho      = 27678*0.285; % Density of ASTM-304 Stainless Steel

% Properties approximated from Eastern-type PWR specs: WWER
-1000

w_core   = 3.67;          % Outer diameter of core barrel
H        = 10.51;         % Height of core barrel
thick    = 0.065;         % Thickness of core barrel

%% Calculated inertia of thick-walled cylinder
% Assuming uniform mass distribution:
% Core barrel's mass (kg)
m        = pi*rho*H*(w_core^2 - (w_core-2*thick)^2)/4;
% Height of core barrel's center of mass (m)
h_G      = H/2;
% Core barrel's mass moment of inertia (kg m^3)
Igx      = m*((3*(w_core/2)^2 + H^2)-(3*(w_core/2-thick)^2 + H^2))
/12;

%% System properties
%  $m \ddot{x} + c_{damp} \dot{x} + k x = b_1 w + b_2 u$ 

% Expected/guessed values (desire  $\omega_n = 10$  Hz)
delta_z  = 0.0025; % Assume 2.5 mm static displacement
% for 2 vertical hold-down springs
kz       = (m*9.81/delta_z)/2; % Estimated spring rate
% of each hold-down spring
delta_y  = 0.5; % Assume 50 cm static displacement
% for horizontal springs & radial keys

```

```

ky      = m*9.81/delta_y;      % Estimated spring rate
% of each horizontal spring/radial key (N/m)

zeta    = 0.1;                % Expected damping ratio
% for horizontal support & radial key

% Process noise coefficients (scaled by 1000)
by1     = 1000;
bz1     = 1000;
btheta1 = 1000;

% Mass matrix
M       = [ m,    0,    0; ...
           0,    m,    0; ...
           0,    0,   Igxx ];

% Spring matrix
K       = [ 2*ky,      0,      -2*ky*(H-h_G); ...
           0,          2*kz,    0; ...
           -2*ky*(H-h_G), 0,      2*(ky*(H-h_G)^2 + kz*w_core^2/4) ];

% Locate eigenvalues (Omega2) and eigenvectors (Phi)
[Phi, Omega2] = eig(M\K);
Omega         = sqrt(Omega2);

% Damping matrix
% C_damp      = 3.6*M + 0.001*K;
C_damp        = M*Phi*(2*zeta*Omega)/Phi;

save('c_damp.mat', 'C_damp');

```

```

% Process noise coefficient matrix
B1_coef      = [ by1,      0,      0; ...
                 0,      bz1,      0; ...
                 0,      0,      btheta1 ];

% Input coefficient matrix
B2_coef      = [ 1,      1,      0,      0; ...
                 0,      0,      1,      1; ...
                 h_G,    h_G,    -w_core/2, w_core/2 ];

%% Create the CT SS
% Dynamics matrix
ss_mat.A      = [ zeros(ss_mat.n_dof),    eye(ss_mat.n_dof); ...
                 -M\K,                    -M\C_damp ];

% Process noise input matrix
ss_mat.B1     = [ zeros(ss_mat.n_dof, ss_mat.n_w_in); ...
                 M\B1_coef ];

% Contact force input matrix
ss_mat.B2     = [ zeros(ss_mat.n_dof, ss_mat.n_u_in); ...
                 M\B2_coef ];

% Measurement output matrix coefficients
coef_y        = 0.25;      % Current's dependence on y
coef_z        = 0.25;      % Current's dependence on z
coef_theta    = 0.5;      % Current's dependence on theta

% Output matrix for all ex-core sensor measurements
ss_mat.C1     = [ coef_y,    coef_z,    -coef_theta; ... % Sensor 1
                 coef_y,    -coef_z,    coef_theta; ... % Sensor 2

```

```

        -coef_y,    coef_z,    coef_theta; ... % Sensor 3
        -coef_y,    -coef_z,    -coef_theta ]; % Sensor 4
ss_mat.C1 = [ss_mat.C1, zeros(ss_mat.m_out, ss_mat.n_dof)];

% Contact force velocity feedback matrix
ss_mat.C2 = [ 1, 0, h_G; ...
              1, 0, h_G; ...
              0, 1, -w_core/2; ...
              0, 1, w_core/2 ];
ss_mat.C2 = [ zeros(ss_mat.n_u_in, ss_mat.n_dof), ss_mat.C2 ];

%% Natural frequency
wn          = damp(ss_mat.A); % Natural frequency (rad/sec)
fn          = wn/(2*pi);     % Natural frequency (Hz)
fNyq       = 2*max(fn);      % Nyquist frequency (Hz)

%% Sampling frequency (greater than fNyq)
fs          = 3200;          % ~40 times fn
ss_mat.h    = 1/fs;          % Sampling period

%% Process noise
ss_mat.Qf = 3*ss_mat.h*eye(ss_mat.n_w_in); % Variance of f
swf = chol(ss_mat.Qf); % Standard deviation of noise
w = @(k) (swf*randn(ss_mat.n_w_in, 1)); % Process noise

function

%% Measurement noise
ss_mat.R = (1e-2)*eye(ss_mat.m_out); % Variance of v
sv = chol(ss_mat.R); % Standard deviation of noise

```

```

v = @(k) (sv*randn(ss_mat.m_out, 1)); % Measurement noise
function

%% Lyapunov Equations (normalizing outputs)
P      = lyap(ss_mat.A, ss_mat.B1 * ss_mat.Qf * ss_mat.B1
    ' ');
norm1    = sqrt( trace(ss_mat.C1 * P * ss_mat.C1') );

% Normalize outputs
ss_mat.C1 = ss_mat.C1/norm1;

%% Scale the state-space representation (Change of Basis)
omega_c = norm(Omega);          % Norm of natural frequency
matrix

% Scaling matrix
T      = inv(diag([1,          1,          180/pi, ...
    1/omega_c, 1/omega_c, 1/omega_c*180/pi]))
    ;

ss_mat.A = T \ ss_mat.A * T; % New basis:  $z = \text{inv}(T)*x$ ,  $x = T*
z$ 
ss_mat.B1 = T \ ss_mat.B1;    %  $z_{\{k+1\}} = \text{inv}(T)*x_{\{k+1\}}$ 
% =  $\text{inv}(T)*(A x_k + B u_k)$ 
ss_mat.B2 = T \ ss_mat.B2;    %  $z_{\{k+1\}} = T\backslash A*(T*z_k) + T\backslash B*u_k$ 
ss_mat.C1 = ss_mat.C1 * T;
ss_mat.C2 = ss_mat.C2 * T;
%  $y_k = C*x_k = C*T*z_k$ 

%% Check the steady state solution

```



```

% State error variance matrix
Sigma      = lyap(ss_mat.A, ss_mat.B1 * ss_mat.Qf * ss_mat.B1');

disp('-----')
norm(Sigma)                                % State variance
norm(ss_mat.C1*Sigma*ss_mat.C1' + ss_mat.R) % Innovation
variance

%% True parameters
% For alpha = 0 and beta = 0, y2max = 0.87.
% Set vc = (1/beta) < 0.87, or else the contact force
% will behave like linear-viscous damping.
% 1e-3 < vc < 0.87 for hyperbolic tangent model
% beta      = 1/vc;
% 10 < gamma < 5e4 for underdamped system with significant
    contact
% alpha      = gamma*vc;

% % Parameters for contactless simulation:
% alpha      = 0;
% beta       = 0;
% gamma      = alpha*beta;

% Setting parameters directly:
alpha      = 100;
beta       = 10;
gamma      = alpha*beta;

%% Equivalent Damping of Contact Force

```

```

disp('Damping_Norms')

% Structural Damping
disp('Structure_alone:')
damp(ss_mat.A)
norm(C_damp)

% Contact force damping
disp('Structure_with_Contact:')
A_contact = ss_mat.B2*alpha*beta*ss_mat.C2;
damp(ss_mat.A - A_contact)
norm(A_contact)

disp('Fastest_natural_frequency_w/_contact')
wn_contact = damp(ss_mat.A - A_contact);
fn_contact = max(wn_contact/(2*pi))

%% Allocate space
N_time = 1e5;
x = zeros(2*ss_mat.n_dof, N_time);
y = zeros(ss_mat.m_out, N_time);
time = 0:ss_mat.h:ss_mat.h*(N_time - 1);

% Iterate
for i = 2:N_time
    wCT_ = w(i-1);
    fturb = ss_mat.B1 * wCT_;
    x(:, i) = myRK4(i-1, x(:, i-1), ss_mat, alpha, beta, fturb)
    ;
    y(:, i) = ss_mat.C1 * x(:, i) + v(i);

```

```

end

% Evaluate contact force
y2 = ss_mat.C2 * x;
fc = -fcontact(y2, alpha, beta);

% Time point indices
t = 1:N_time;

%% Save Data
% Save synthetic data
save('data_core.mat', 'y', 'x');
% Save SS model information (SS matrices, dimensions, Qf, R)
save('model_core.mat', 'ss_mat');
% Save contact info (parameters for grid search)
save('contact_core.mat', 'alpha', 'beta');

% Save CSV file for true response (grid search method)
ytrue_mat = [ 0:4;
              time', y' ];
writematrix(ytrue_mat, 'Synth_Outputs_True_core.csv')

% Save CSV file for true coefficient combination
coefs = [1; alpha; beta];
writematrix(coefs, 'Synth_Outputs_True_Coefs_core.csv')

% Save CSV file for true states (UKF)
xtrue_mat = [ 0:6;
              time', x'];
writematrix(xtrue_mat, 'Synth_States_True_core.csv')

```

B.1.1 Fourth-Order Runge-Kutta Method

The synthetic dataset's states at each time point are evaluated for the core barrel system using a fourth-order Runge-Kutta method, as defined in the function `myRK4`.

```
%% 4th-Order Runge Kutta integrator
function xnext = myRK4(t, x, ss_mat, alpha, beta, process_noise
    )
    % Time step
    h = ss_mat.h;
    % Slopes
    K1 = CT_ODEs(t, x, ss_mat, alpha, beta);
    K2 = CT_ODEs(t + (h / 2), x + (h / 2)*K1, ss_mat, alpha,
        beta);
    K3 = CT_ODEs(t + (h / 2), x + (h / 2)*K2, ss_mat, alpha,
        beta);
    K4 = CT_ODEs(t + h, x + h*K3, ss_mat, alpha, beta);
    % Estimate the next state (including process noise from
        turbulence)
    xnext = x + (ss_mat.h / 6)*(K1 + 2*K2 + 2*K3 + K4) +
        process_noise;
end
```

B.1.2 Continuous-time Equations of Motion

The continuous-time equations of motion for the core barrel system are expressed in the user-defined function `CT_ODEs`. These equations are used within the Runge-Kutta method to solve for the system's states.

```
%% CT differential equations of motion (no process noise)
function xdot = CT_ODEs(t, x, ss_mat, alpha, beta)
    % Compute the velocity of each contact point
```

```

y2 = ss_mat.C2 * x;
% Differential equations of motion
xdot = ss_mat.A * x + ss_mat.B2 * fcontact(y2, alpha, beta)
;
end

```

B.1.3 Hyperbolic Tangent Contact Force Function

The function for the equations of motion also depends upon the user-defined contact force function `fcontact`.

```

%% Contact force applied to the core barrel
function Fc = fcontact(y2, alpha, beta)
% Hyperbolic tangent contact force model
Fc = -alpha * tanh(beta * y2);
end

```

B.2 Grid Search Ensemble Generation

An ensemble of 20 simulations is generated for each combination of contact parameters in the grid search method. This requires a total of 680 simulations for the entire grid of 34 parameter combinations. The data generation process is hastened by using MATLAB's parallel computing toolbox to simultaneously generate simulations across 4 pools of processors. This process requires more computational power, but in return it drastically decreases the computation time. The following code uses a parallel for-loop with 4 workers to generate the grid of ensembles.

```

% 06/03/2022, Nicholas Harn
% Grid of ensembles

```

```

clear;
close all;
clc;
delete(gcp('nocreate'));

% Set rng seed for each replication (shuffle)
rng('shuffle');

%% Load Data
load('data_core.mat');      % Load synthetic data
load('model_core.mat');     % Load core barrel model
load('contact_core.mat');   % Load contact parameters

%% System dimensions
% Number of states (including parameters)
ss_mat.n_state = 2*ss_mat.n_dof;
% Number of process noise inputs (including disturbances)
ss_mat.q       = ss_mat.n_w_in;

% Number of augmented states
ss_mat.n_a     = ss_mat.n_state + ss_mat.q + ss_mat.m_out;
% Number of augmented outputs
ss_mat.m_a     = ss_mat.n_state + ss_mat.m_out;

% Number of time points and samples
ss_mat.N       = length(x);
% Time vector
time           = 0 : ss_mat.h : ss_mat.h*(ss_mat.N - 1);

%% Define process noise

```

```

swf = chol(ss_mat.Qf); % Process noise standard deviation
w   = @(k) (swf*randn(ss_mat.q, 1)); % Process noise

%% Define measurement noise
sv  = chol(ss_mat.R); % Measurement noise standard deviation
v   = @(k) (sv*randn(ss_mat.m_out, 1)); % Measurement noise

%% Set-up grid search
% Parameter values
a     = 1:0.5:5;
ss_mat.alpha_vect = 10.^a; % Max contact force
b     = -1:0.5:3;
ss_mat.beta_vect  = 10.^b; % Inverse of characteristic
    velocity

% Number of coefficients for the grid
ss_mat.N_coef      = length(a);

%% Parfor loop (for multiple replications)
num_reps = 20; % Number of replications for the ensemble

% Begin timer and loop
tic;
parfor rep_id = 1:num_reps % Parallel computing on 4 workers
    %% Initializing arrays for storing data
    % Initialize array for storing states of simulations
    X_all_coefs      = zeros(ss_mat.N_coef, ss_mat.N_coef, ...
        ss_mat.n_state, ss_mat.N);

    % Initialize arrays for storing inputs and outputs

```

```

Y1_all_coefs      = zeros(ss_mat.N_coef, ss_mat.N_coef, ...
    ss_mat.m_out, ss_mat.N);
Y2_all_coefs      = zeros(ss_mat.N_coef, ss_mat.N_coef, ...
    ss_mat.n_u_in, ss_mat.N);
U1_all_coefs      = zeros(ss_mat.N_coef, ss_mat.N_coef, ...
    ss_mat.q, ss_mat.N);
U2_all_coefs      = zeros(ss_mat.N_coef, ss_mat.N_coef, ...
    ss_mat.n_u_in, ss_mat.N);

% Set Initial Condition for State
X_all_coefs(:, :, :, 1) = zeros(ss_mat.N_coef, ...
    ss_mat.N_coef, ss_mat.n_state, 1);

%% Iterative solver
% Iterate over alpha
for i_alpha        = 1:ss_mat.N_coef
    alpha          = ss_mat.alpha_vect(i_alpha);

    % Iterate over beta
    for i_beta     = 1:ss_mat.N_coef
        beta       = ss_mat.beta_vect(i_beta);

        % Keep 1e2 <= gamma = alpha * beta <= 1e4
        if alpha * beta > 1.01e4          % 1.01e4?
            continue
        elseif alpha * beta < 9.9e1       % 9.9e1?
            continue
        end

        % Initialize matrix of state vectors

```



```

X          = zeros(ss_mat.n_state, ss_mat.N);
% Initial conditions for this parameter combination
X(:, 1)    = zeros(ss_mat.n_state, 1);

% Initialize arrays for storing forces and outputs:
% Matrix of ex-core measurements
Y1         = zeros(ss_mat.m_out, ss_mat.N);
% Matrix of turbulent forces
U1         = zeros(ss_mat.q, ss_mat.N);
% Matrix of process noise terms from turbulence
fturb      = zeros(ss_mat.n_state, ss_mat.N);

% Iterate over time
for i_t = 2:ss_mat.N
    % Input vector
    U1(:, i_t - 1) = w(i_t - 1);
    % Process noise from turbulence
    fturb(:, i_t - 1) = ss_mat.B1 * U1(:, i_t - 1);

    % Solve for the state at the next time point
    X(:, i_t) = myRK4(i_t - 1, X(:, i_t - 1), ...
        ss_mat, alpha, beta, fturb(:, i_t - 1));

    % Output vector
    Y1(:, i_t) = ss_mat.C1*X(:, i_t) + v(i_t);
end

% Solve for contact force
Y2         = ss_mat.C2 * X;
U2         = fcontact(Y2, alpha, beta);

```

```

        % Save data for this coefficient combination
        X_all_coefs(i_alpha, i_beta, :, :) = X;
        Y1_all_coefs(i_alpha, i_beta, :, :) = Y1;
        Y2_all_coefs(i_alpha, i_beta, :, :) = Y2;
        U1_all_coefs(i_alpha, i_beta, :, :) = U1;
        U2_all_coefs(i_alpha, i_beta, :, :) = U2;
    end
end

%% Save synthetic grid data
% Define reorganized matrix for storing synthetic data
output_matrix_1 = zeros(ss_mat.N, ss_mat.N_coef^2 + 1);
output_matrix_1(:, 1) = time';

% Extract coefficient values
alpha_vect = ss_mat.alpha_vect;
beta_vect = ss_mat.beta_vect;

% Reorganize the data
i_col = 0;
for i_alpha = 1:ss_mat.N_coef
    for i_beta = 1:ss_mat.N_coef
        % Establish ranges of parameter values
        if alpha_vect(i_alpha)*beta_vect(i_beta) > 1.01e4
            continue
        elseif alpha_vect(i_alpha)*beta_vect(i_beta) < 99
            continue
        end
    end
end

```

```

        % Column index
        i_col = i_col + 1;

        % Reorganized output data
        out_mat_icol = squeeze(Y1_all_coefs(i_alpha, ...
            i_beta, 1, :));
        output_matrix_1(:, i_col + 1) = out_mat_icol;
    end
end

% Label the reorganized matrix's columns
output_matrix_1_labelled = [0:ss_mat.N_coef^2; ...
    output_matrix_1];

% Save matrix as a CSV datafile
writematrix(output_matrix_1_labelled, ...
    sprintf('Synth_Output1_Grid_core_Rep_%03d.csv', ...
        rep_id));
end

% Delete parallel pool once finished
delete(gcp('nocreate'));

% End timer
toc

%% Save coefficient data
% Initialize the coefficient matrix
coefs = zeros(2, ss_mat.N_coef^2);

```

```

% Extract coefficient values for the grid
alpha_vect = ss_mat.alpha_vect;
beta_vect  = ss_mat.beta_vect;

% Populate the coefficient matrix
i_col = 0;
for i_alpha = 1:ss_mat.N_coef
    for i_beta = 1:ss_mat.N_coef
        % Establish ranges of parameter values
        if alpha_vect(i_alpha)*beta_vect(i_beta) > 1.01e4
            continue
        elseif alpha_vect(i_alpha)*beta_vect(i_beta) < 99
            continue
        end

        % Indexing the data matrix's empty columns (2 - 120)
        i_col = i_col + 1;

        % Populating columns of matrices
        coefs(:, i_col) = [alpha_vect(i_alpha); ...
            beta_vect(i_beta)];
    end
end

% Label the coefficient matrix
coef_label = 1:length(coefs);
coef_matrix_labelled = [coef_label; coefs];

% Save coefficient data in .csv file

```

```
writematrix(coef_matrix_labelled, 'Synth_Output1_Coefs_core.csv'
    ');
```

B.3 Unscented Kalman Filter Approximation

The following MATLAB code applies an unscented Kalman filter to a synthetic dataset, generating state, output, and parameter estimates for the core barrel system.

```
% 07/20/2022, Nicholas Harn
% Unscented Kalman filter for Core Barrel
clear;
close all;
clc;
rng('shuffle');

%% Load Data
load('data_core.mat');          % Load synthetic data
load('model_core.mat');         % Load core barrel model

% Load core contact parameters
load('contact_core.mat');       % Load core contact parameters

%% System dimensions
% Number of states (including parameters)
ss_mat.n_state = 2*ss_mat.n_dof + 2;
% Number of process noise inputs (including disturbances)
ss_mat.q        = ss_mat.n_w_in + 2;

% Number of augmented states
```

```

ss_mat.n_a      = ss_mat.n_state + ss_mat.q + ss_mat.m_out;
% Number of augmented outputs
ss_mat.m_a      = ss_mat.n_state + ss_mat.m_out;

% Number of time points
ss_mat.N        = length(x);           % Number of samples
time = 0:ss_mat.h:ss_mat.h*(ss_mat.N - 1); % Time vector

%% Define noise on the system
% Disturbance of alpha's estimate
seps1 = 1e1;      % Standard dev of alpha's estimate (0.1*alpha)
Qeps1 = seps1^2; % Variance of alpha's estimate

% Disturbance of beta's estimate
seps2 = 1e0;      % Standard dev of beta's estimate (0.1*beta)
Qeps2 = seps2^2; % Variance of beta's estimate

% State variance (with parameter disturbances)
ss_mat.Q = [ss_mat.Qf,          zeros(ss_mat.n_w_in, 2);
    ...
            zeros(1, ss_mat.n_w_in), Qeps1, 0;
    ...
            zeros(1, ss_mat.n_w_in), 0,      Qeps2];

%% Initialize
% Initial guess of state estimate
% alpha0      = 1e1; % Underestimate as 10% of the true value
% beta0       = 1e0; % Underestimate as 10% of the true value
alpha0        = 0;
beta0         = 0;

```

```

xc0          = [ zeros(2*ss_mat.n_dof, 1); alpha0; beta0 ];

% Initial guess of state variance
Sxxc         = (1e-3) * eye(ss_mat.n_state);

% Set weighting factor kappa
kappa        = 0.5;

%% Generate the state estimate
[xp, xc, yp, yc, K_t, Sxxc] = myUKF(y, ...
    xc0, Sxxc, kappa, ss_mat);

%% Estimates of alpha and beta
alpha_avg     = mean(xc(7, ss_mat.N/5:ss_mat.N));
alpha_stdev   = std(xc(7, ss_mat.N/5:ss_mat.N));
beta_avg      = mean(xc(8, ss_mat.N/5:ss_mat.N));
beta_stdev    = std(xc(8, ss_mat.N/5:ss_mat.N));

%% Create plots of state, output, and parameter estimates
PLOT_SOME_STUFF

%% Save data as CSV
% Create dataset label
data_label = 1:(1 + ss_mat.m_a);

%% Organize data:
% Column 1 = Time vector, Columns 2 - 7 = States
% Columns 8 - 9 = Contact Parameters
% Columns 10 - 13 = Outputs, Row 1 = Labels
% Rows 2 - 100001 = Values at various time points

```

```

data_matrix = [ data_label; ...
               time', xc', yc'];

% Save as CSV
writematrix(data_matrix, 'Synth_UKF_Estimates_core.csv')

% Organize data:
% Column 1 = alpha, Column 2 = beta
% Row 1 = Labels, Row 2 = Average value
% Row 3 = Standard deviation
param_est    = [ 0,                1;
                alpha_avg,         beta_avg;
                alpha_stdev,        beta_stdev ];

% Save as CSV
writematrix(param_est, 'Synth_UKF_Param_Estimates_core.csv')

% Save outputs as mat file
xc_states = xc(1:2*ss_mat.n_dof, :);
xc_params = xc((2*ss_mat.n_dof + 1):ss_mat.n_state, :);
save('ukf_estimates.mat', ...
     'time', 'xc_states', 'xc_params', 'yc', 'y2c', 'fc_est');

%% FUNCTIONS

% Augmented function for the sigma point transformation
function ybig = fa(t, xbig, ss_mat)

    %% Extract info from ss_mat
    n_state = ss_mat.n_state;    % Number of states
    n_a      = ss_mat.n_a;        % Number of augmented states
    n_dof     = ss_mat.n_dof;     % Number of degrees of freedom

```



```

q          = ss_mat.q;          % Number of process noise
    inputs
n_w_in    = ss_mat.n_w_in;      % Number of turbulent inputs

%% Deconstruct the function's augmented input vector xbig
% States
x_        = xbig(1:n_state, :);
% Process noise
w_        = xbig((n_state + 1):(n_state + q), :);
% Measurement noise
v         = xbig((n_state + q + 1):n_a, :);

%% Deconstruct the state
% CT system's states
xCT_      = x_(1:2*n_dof, :);
% Parameter states
param_    = x_((2*n_dof + 1):n_state, :);

%% Deconstruct process noise
% CT system's process noise
wCT_      = w_(1:n_w_in, :);
% Process noise on parameters
epsilon   = w_((n_w_in + 1):q, :);

% Compute process noise from turbulence
fturb     = ss_mat.B1 * wCT_;

% Update the state
xCT       = myRK4(t, xCT_, ss_mat, ...
    param_(1,:), param_(2,:), fturb);

```

```

    % Require positive parameters
    param    = abs(param_ + epsilon);

    % Evaluate the measurement (including noise)
    y        = ss_mat.C1 * xCT + v;

    % Augmented function's output
    ybig     = [ xCT; param; y ];
end

% UKF prediction and update equation
function [xp, xc, yp, yc, K_t, Sxxc] = myUKF(y, ...
    x0, Sxx0, kappa, ss_mat)
    % Extract dimensions
    N        = ss_mat.N;           % Number of time points
    n_state  = ss_mat.n_state;     % Number of states
    n_a      = ss_mat.n_a;         % Number of augmented states
    m_out    = ss_mat.m_out;       % Number of outputs
    m_a      = ss_mat.m_a;         % Number of augmented outputs
    q        = ss_mat.q;           % Number of process noise inputs
    n_dof    = ss_mat.n_dof;       % Number of degrees of freedom

    % Extract other information
    Q        = ss_mat.Q;           % Process noise variance
    R        = ss_mat.R;           % Measurement variance
    h        = ss_mat.h;           % Time step length

    % Allocate space for inputs and outputs
    xp       = zeros(n_state, N);

```

```

xc      = zeros(n_state, N);
yp      = zeros(m_out, N);
yc      = zeros(m_out, N);

% Initialize posterior (corrected) estimates
xc(:, 1) = x0;
Sxxc     = Sxx0;

% Create time-varying Kalman gain matrix
K_t      = zeros(n_state, m_out, N);

% Iterate
for i     = 2:N
    % Current value of time
    t     = h*i;

    % Assemble augmented state vector
    xbig = [xc(:, i-1); zeros(q + m_out, 1)];

    % Assemble augmented state variance
    Xbig = [Sxxc, zeros(n_state, m_out + q); ...
            zeros(q, n_state), Q, zeros(q, m_out); ...
            zeros(m_out, n_state + q), R];

    % Sigma-point transformation
    [ybig, Ybig] = unscented_trans(@(t,xbig) fa(t, ...
        xbig, ss_mat), t, xbig, Xbig, n_a, m_a, kappa);

    % Deconstruct mean
    xp(:, i) = ybig(1:n_state, :);

```

```

yp(:, i) = ybig((n_state + 1):m_a, :);

% Deconstruct covariance matrix
Sxxp      = Ybig(1:n_state, 1:n_state);
Sxyp      = Ybig(1:n_state, (n_state + 1):m_a);
Syxp      = Ybig((n_state + 1):m_a, 1:n_state); % Sxyp'
Syyp      = Ybig((n_state + 1):m_a, (n_state + 1):m_a);

% Compute Kalman gain
K          = Sxyp*inv(Syyp);
K_t(:, :, i) = K;

% Correct state estimate
xc(:, i) = xp(:, i) + K*(y(:, i) - yp(:, i));
Sxxc      = Sxxp - Sxyp*inv(Syyp)*Syxp;

% Corrected output
yc(:, i) = ss_mat.C1*xc(1:2*n_dof, i);
end
end

```

B.3.1 Unscented Transformation Function

The unscented Kalman filter approach uses the function `unscented_trans` to apply an unscented transformation to the core barrel system's augmented states at each time point.

```

%% Unscented Transformation function, as developed by
% Julier and Uhlmann
% Code written by Nicholas Harn and Dr. Daniel G Cole

```

```

function [ybar, Pyy] = unscented_trans(func, ...
    t, xbar, Pxx, n, m, kappa)

% [ybar,Pyy] = UNSCENTED_TRANS(FUNC,t,XBAR,PXX,M,N,KAPPA)
% returns the mean estimate ybar and
% covariance estimate Pyy of a function FUNC
% for an input probability density
% with mean XBAR and covariance PXX.
% The dimension of the input to FUNC is N and
% the dimension of the output is M.
% KAPPA is a free parameter used in
% the unscented algorithm.
% t is the time vector for the simulation.

% Cholesky factorization of the input's variance
% (effectively the input's standard deviation)
U = chol((n + kappa)*Pxx)';

% Initialize matrices for the sigma points,
% weights, and transformed points
chi = zeros(n, 2*n + 1);
W    = zeros(2*n + 1, 1);
y    = zeros(m, 2*n + 1);

% Transform the mean of the input
chi(:, 1)    = xbar;
W(1)         = kappa/(n + kappa);
y(:, 1)      = func(t, chi(:, 1));

for i = 1:n,

```

```

    % Sigma points of x (distributed about the mean)
    chi(:, i+1)      = xbar + U(:, i);
    chi(:, i+n+1)    = xbar - U(:, i);

    % Weights of the sigma points
    W(i+1)           = 1/2/(n + kappa);
    W(i+n+1)         = 1/2/(n + kappa);

    % Transform the sigma points
    y(:, i+1)        = func(t, chi(:, i+1));
    y(:, i+n+1)      = func(t, chi(:, i+n+1));
end

% Initialize the statistics of the transformed points
ybar      = zeros(m, 1);
Pyy       = zeros(m, m);

% Evaluate the mean of the transformed sigma points
for i = 1:(2*n+1),
    ybar    = ybar + W(i)*y(:, i);
end

% Evaluate the variance of the transformed sigma points
for i = 1:(2*n+1),
    Pyy = Pyy + W(i)*(y(:, i) - ybar)*(y(:, i) - ybar)';
end

return
end

```

B.3.2 Additional Computations for the Estimates

The MATLAB file `PLOT_SOME_STUFF.m` computes additional information regarding the unscented Kalman filter's simulated responses. These computations include a comparison of the estimated contact force to the synthetic dataset's true contact force, approximating the power dissipated by the system, and evaluating the errors of the estimations.

```
%% Calculate innovation of the output and errors of the  
estimates  
  
% Innovation of the output predictions  
innov    = y - yp;  
  
  
% State correction term (theoretically xc - xp)  
x_correction = zeros(ss_mat.n_state, ss_mat.N); % Initialize  
for i      = 1:ss_mat.N  
    x_correction(:, i) = K_t(:, :, i)*innov(:, i);  
end  
  
  
% Error of the corrected outputs  
err      = y - yc;  
  
  
%% Calculate various estimates and true values  
  
% Slope of the contact force function's viscous region  
gamma_true = alpha * beta;           % True  
gamma_est  = xc(7, :) .* xc(8, :); % Estimate  
  
  
% True velocity at the point of contact  
y2        = ss_mat.C2 * x;  
  
% Corrected contact point velocity estimate  
y2c       = ss_mat.C2 * xc(1:(2*ss_mat.n_dof), :);
```

```

% True contact force
fc_true = fcontact(y2, alpha, beta);
% Corrected contact force estimate
fc_est = zeros(ss_mat.n_u_in, ss_mat.N); % Initialize
for i = 1:ss_mat.N
    fc_est(:,i) = fcontact(y2c(:, i), xc(7, i), xc(8, i));
end

% True power dissipated by the contact force
Pdiss_cont_true = sum( abs(fc_true.*y2), 1);
% Estimated power dissipated by the contact force
Pdiss_cont_est = sum( abs(fc_est.*y2c), 1);

% Power dissipated by the core barrel structure
load('c_damp.mat'); % Load structure's damping matrix
Pdiss_struc_est = zeros(1, ss_mat.N); % Initialize
Pdiss_struc_true = zeros(1, ss_mat.N); % Initialize
for i = 1:ss_mat.N
    % True structural power dissipation
    Pdiss_struc_true = sum(0.5*x(4:6, i)'*C_damp*x(4:6, i), 1);
    % Estimated structural power dissipation
    Pdiss_struc_est = sum(0.5*xc(4:6, i)'*C_damp*xc(4:6, i),
        1);
end

% Total power dissipated
Pdiss_true = Pdiss_cont_true + Pdiss_struc_true; % True
Pdiss_est = Pdiss_cont_est + Pdiss_struc_est; % Estimate

```


Bibliography

- [1] *Assessment and Management of Ageing of Major Nuclear Power Plant Components Important to Safety: PWR Vessel Internals*. Number 1557 in TECDOC Series. INTERNATIONAL ATOMIC ENERGY AGENCY, Vienna, 2007.
- [2] C. Montalvo, Imre Pazsit, H. Nylén, and Victor Dykin. First evidence of the pivotal motion ("tilting mode") of the core barrel in the ringhals-4 pwr, 2016.
- [3] Imre Pazsit, Henrik Nylén, and Cristina Montalvo Martín. Refined method for surveillance and diagnostics of the core barrel vibrations of the ringhals pwrs, 2014.
- [4] G. Por. Reactor noise analysis applications and systems in wwer-440 and wwer-1000 type pwrs. In *On-line testing of nuclear plant temperature and pressure instrumentation and other critical plant equipment IAEA regional workshop Working material*, page 609. IAEA, 1998.
- [5] I. Pázsit, J. Karlsson, and N. S. Garis. Some developments in core-barrel vibration diagnostics. *Annals of Nuclear Energy*, 25(13):1079–1093, 1998.
- [6] Imre Pázsit and Christophe Demazière. *Noise Techniques in Nuclear Systems*, chapter Chapter 14, pages 1629–1737. Springer US, Boston, MA, 2010.
- [7] J. Kenneth Shultis and Richard E. Faw. *Fundamentals of Nuclear Science and Engineering*. CRC Press, 2 edition, 2008.
- [8] Joseph A Thie. Core Motion Monitoring. *Nuclear technology*, 45(1):5–45, 1979.
- [9] A. Trenty. Operational feedback on internal structure vibration in 54 french pwrs during 300 fuel cycles. *Progress in Nuclear Energy*, 29(3-4):347–356, 1995.
- [10] R. T. Wood and R. B. Perez. Modeling and analysis of neutron noise from an ex-core detector at a pressurized water reactor. 1991. AC05-84OR21400.